APPLIED PHYSICS REVIEWS

Femtosecond laser three-dimensional micro- and nanofabrication

Koji Sugioka[1,a)] and Ya Cheng[2,b)]

[1]RIKEN Center for Advanced Photonics, Hirosawa 2-1, Wako, Saitama 351-0198, Japan
[2]Shanghai Institute of Optics and Fine Mechanics, Chinese Academy of Sciences, P.O. Box 800-211, Shanghai 201800, China

The rapid development of the femtosecond laser has revolutionized materials processing due to its unique characteristics of ultrashort pulse width and extremely high peak intensity. The short pulse width suppresses the formation of a heat-affected zone, which is vital for ultrahigh precision fabrication, whereas the high peak intensity allows nonlinear interactions such as multiphoton absorption and tunneling ionization to be induced in transparent materials, which provides versatility in terms of the materials that can be processed. More interestingly, irradiation with tightly focused femtosecond laser pulses inside transparent materials makes three-dimensional (3D) micro- and nanofabrication available due to efficient confinement of the nonlinear interactions within the focal volume. Additive manufacturing (stereolithography) based on multiphoton absorption (two-photon polymerization) enables the fabrication of 3D polymer micro- and nanostructures for photonic devices, micro- and nanomachines, and microfluidic devices, and has applications for biomedical and tissue engineering. Subtractive manufacturing based on internal modification and fabrication can realize the direct fabrication of 3D microfluidics, micromechanics, microelectronics, and photonic microcomponents in glass. These microcomponents can be easily integrated in a single glass microchip by a simple procedure using a femtosecond laser to realize more functional microdevices, such as optofluidics and integrated photonic microdevices. The highly localized multiphoton absorption of a tightly focused femtosecond laser in glass can also induce strong absorption only at the interface of two closely stacked glass substrates. Consequently, glass bonding can be performed based on fusion welding with femtosecond laser irradiation, which provides the potential for applications in electronics, optics, microelectromechanical systems, medical devices, microfluidic devices, and small satellites. This review paper describes the concepts and principles of femtosecond laser 3D micro- and nanofabrication and presents a comprehensive review on the state-of-the-art, applications, and the future prospects of this technology. © 2014 Author(s). All article content, except where otherwise noted, is licensed under a Creative Commons Attribution 3.0 Unported License. [http://dx.doi.org/10.1063/1.4904320]

TABLE OF CONTENTS

a)ksugioka@riken.jp
b)ya.cheng@siom.ac.cn

I. INTRODUCTION

Femtosecond lasers have been proven to be a powerful tool for advanced materials processing on both the micro- and nanoscale. Compared with traditional laser processing techniques that use longer pulse or continuous wave lasers, femtosecond laser micromachining offers several key advantages due to its unique characteristics of ultrashort pulse width and extremely high peak intensity. The advantages include suppression of heat-affected zone (HAZ) formation around the irradiated area, high spatial resolution beyond the diffraction limit, and versatility in terms of the materials that can be processed.[1,2] In particular, the versatility relies on nonlinear interactions of the femtosecond laser beam with transparent materials due to the high peak intensity, such as multiphoton absorption or tunneling ionization.[3] Thus, the femtosecond laser can process both opaque and transparent materials, such as metals, ceramics, soft materials (e.g., polymers and biotissues), and even brittle materials (e.g., glasses), and is presently in wide use for applications such as high-quality, high-precision surface micro- and nanomachining, such as scribing/cutting, drilling, surface patterning and texturing, nanoablation, and micro/nanostructuring.[4–7] More interestingly, once tightly focused and employed for direct writing inside a transparent material, the intense femtosecond laser pulses intrinsically provide the capability for three-dimensional (3D) micro- and nanofabrication due to efficient confinement of the nonlinear interactions within the focal volume, which enables sub-100 nm stereolithography based on two-photon polymerization (TPP) as well as micro- and nanoscale internal modification of bulk transparent materials including glass and polymers.[8–12] Furthermore, nonlinear interactions can be induced at the interface between two tightly stacked transparent substrates (e.g., two adjacent glass plates), which allows local melting and bonding of various glasses.[13,14] Such 3D micro- and nanofabrication is a peculiar feature that can only be achieved with ultrashort pulse lasers. Femtosecond laser 3D micro- and nanofabrication represents a breakthrough with potential advances for a broad range of applications, from optoelectronics, photonics, and microelectromechanical systems (MEMS) to chemical, biological, and medical systems.

Although in the past decade, a considerable number of review articles have been published on femtosecond laser micromachining for surface structuring, photonic and optofluidic applications and on femtosecond laser TPP,[1,2,8–12,15–17] few reports have provided a comprehensive review specifically focused on 3D micro- and nanofabrication with femtosecond lasers. Thus, the aim of this review is to provide a more complete picture of the history, current status, and likely future trends of femtosecond laser 3D micro- and nanofabrication. Femtosecond laser 3D microfabrication was first demonstrated in 1996 for waveguide fabrication and high-density data storage, both in fused silica.[18,19] One year later, a femtosecond laser was used as an alternative to ultraviolet (UV) light sources for the production of 3D microstructures by TPP.[20] Combined with the threshold effect, the quadratic intensity dependence of photoabsorption in TPP has significantly improved the resolution of 3D microstructuring beyond the diffraction limit. This unique capability has had a significant impact on a wide range of scientific communities. This field has since undergone steady growth at an increasing pace, and femtosecond laser TPP has been extensively investigated for the fabrication of photonic crystals, optical metamaterials, tissue scaffolds, micro/nano-fluidic components, and micro/nanomachines.[21–28] To date, femtosecond laser internal processing has been widely applied to the fabrication of photonic integrated circuits, free-space microoptics, and microfluidic/optofluidic chips.[29–39] However, femtosecond laser bonding of glasses has recently attracted significant attention as an emerging technique for optoelectronics, medical and biochips, and MEMS packaging,[13,14,40,41] which are important for a number of applications.

In this review, we first discuss several prominent features of femtosecond laser processing. Focus is then placed on femtosecond laser 3D micro- and nanofabrication, in an attempt to provide a comprehensive review on TPP, internal processing of transparent materials, and glass bonding using femtosecond lasers. Last, we conclude with a summary and examine the future perspectives.

II. FEATURES OF FEMTOSECOND LASER PROCESSING

A. Suppression of heat-affected zone

Femtosecond laser processing is often referred to as a nonthermal process, which is in contrast to processing with nanosecond and longer pulses, so that femtosecond lasers provide excellent performance in material processing to realize high-precision, high-quality micro- and nanofabrication. This characteristic has been explained as rapid energy deposition in the material. It takes a few hundred femtoseconds to a few picoseconds for the electron distribution to reach thermal equilibrium after femtosecond laser irradiation.[42,43] However, the energy transfer time from the electron subsystem to the lattice, which induces thermalization, is of the order of 1–100 ps, depending on the electron–phonon coupling strength of the material; this time is much longer than the time for the electrons to reach thermal equilibrium.[44,45] Thus, the femtosecond laser can efficiently cause electron heating and generate a hot electron gas that is far from equilibrium with the lattice. Consequently, only a very small fraction of the laser pulse energy is transformed to heat, so that nonthermal processing can be realized, which results in high-precision, high-quality micro- and nanofabrication.

Nevertheless, femtosecond laser irradiation of a material still generates heat. However, one of the most important features of femtosecond laser processing is that the formation of a HAZ is suppressed due to the extremely short pulse widths of several tens to several hundreds of femtoseconds. Thus, high-precision, high-quality micro- and nanofabrication can be realized even for high thermal conductivity materials such as metals.

When the pulse width of the laser is shorter than the electron-phonon coupling time in laser-matter interactions (of the order of 1–100 ps, depending on the electron–phonon coupling strength of the material), thermal diffusion in the vicinity of the laser irradiated region can be almost
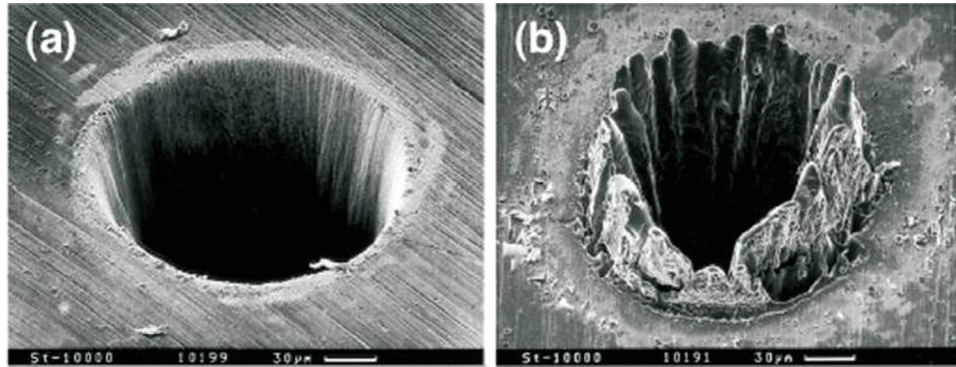
FIG. 1. SEM micrographs of holes drilled in 100-μm-thick steel foils by ablation using laser pulses with the following parameters: (a) pulse width: 200 fs, pulse energy: 120 mJ, fluence: 0.5 J/cm^2, wavelength: 780 nm; and (b) pulse width: 3.3 ns, pulse energy: 1 mJ, fluence: 4.2 J/cm^2, wavelength: 780 nm. The scale bars represent 30 μm. Reproduced with permission from Chichkov *et al.*, Appl. Phys. A **63**, 109 (1996). Copyright 1996 Springer.

eliminated. For most metals, the electron-phonon coupling time is of the order of picoseconds,[46] which is sufficiently longer than the pulse width of the femtosecond laser. In this regime, the thermal diffusion length l_d, when the material is heated to around the melting point T_{im}, by femtosecond laser irradiation, is given by

$$l_d = \left[\frac{128}{\pi}\right]^{1/8} \left[\frac{DC_i}{T_{im}\Lambda^2 C'_e}\right]^{1/4}, \qquad (1)$$

where D is the heat conductivity, C_i is the lattice heat capacity, $C'_e = C_e/T_e$ (where C_e is the electron heat capacity and T_e is the electron temperature), and Λ is the electron-phonon coupling constant.[47] From Eq. (1), l_d is independent of the pulse width in this regime. For example, when copper is heated to its melting point of $T_{im} = 1356$ K by a femtosecond laser, l_d is calculated to be 329 nm.[48]

On the other hand, when the pulse width of the laser τ, is much longer than the electron-phonon coupling time, l_d can be roughly estimated by

$$l_d = \sqrt{\kappa\tau}, \qquad (2)$$

where κ is the thermal diffusivity. For copper, l_d is estimated to be 1.5 μm for $\tau = 10$ ns; therefore, a femtosecond laser can clearly reduce the thermal diffusion length, which means that it can minimize the formation of a HAZ at the processed region.

Figures 1(a) and 1(b) show scanning electron microscopy (SEM) images of holes drilled in 100 μm thick steel foils by ablation using laser pulses with widths of 200 fs and 3.3 ns, respectively.[4] Femtosecond laser ablation creates an ablated hole with a sharp edge, a steep wall, and little formation of a HAZ. In contrast, nanosecond laser ablation produces severe swelling around the ablated hole due to melting.

Although the femtosecond laser can minimize formation of a HAZ at the processed regions, irradiation with repetition rates higher than a couple of hundred kilohertz (depending on material characteristics such as thermal diffusivity and specific heat) induces heat accumulation, which results in formation of a significant HAZ that is much larger than the laser spot size.[49,50] Therefore, femtosecond laser irradiation at higher repetition rates sometimes results in deteriorated ablation quality; however, the heat accumulation effect that

produces a larger molten pool is beneficial for glass-glass fusion bonding, as described later.

B. Nonlinear absorption by transparent materials

Femtosecond laser irradiation incident on materials such as dielectrics and wide bandgap crystals, which are transparent to the laser wavelength, can cause electron excitation (ionization) to be induced by nonlinear processes such as multiphoton absorption (ionization) and/or tunneling ionization due to the extremely high peak intensity of the laser.[3,51] In either of these nonlinear processes, free electrons are eventually generated in the conduction band.

Figure 2 depicts single and multiphoton absorption based on the electron excitation process in bandgap materials such as semiconductors and glass. The typical absorption process is linear single-photon absorption (Fig. 2(a)). When light with a photon energy that is larger than the bandgap of a specific material is incident on the material, it is absorbed and an electron is excited from the valence band to the conduction band by a single photon. In contrast, light with a photon energy that is smaller than the bandgap cannot excite electrons, so that no absorption is induced in the stationary state. However, when extremely high density of photons are
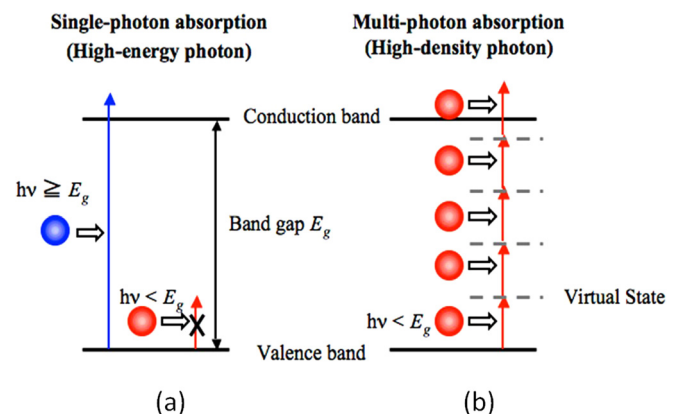

FIG. 2. Electron excitation processes in bandgap materials by (a) single and (b) multiphoton absorption. Reproduced with permission from K. Sugioka and Y. Cheng, *Femtosecond Laser 3D Micromachining for Microfluidic and Optofluidic Applications*, Springer Briefs in Applied Science and Technology (Springer, London, 2014), p. 22. Copyright 2014 Springer.[210]
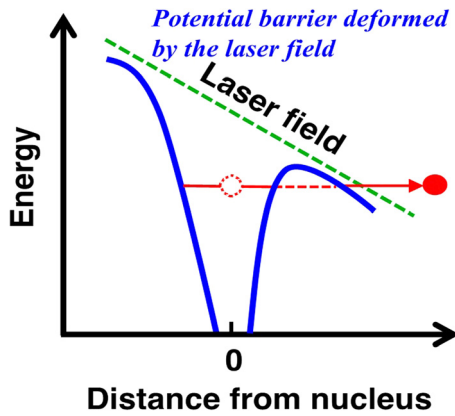
FIG. 3. Tunneling ionization process induced in materials by an intense electric field of a femtosecond laser. Reproduced with permission from K. Sugioka and Y. Cheng, *Femtosecond Laser 3D Micromachining for Microfluidic and Optofluidic Applications*, Springer Briefs in Applied Science and Technology (Springer, London, 2014), p. 23. Copyright 2014 Springer.[210]

simultaneously incident on the material, an electron can be excited by multiple photons via virtual states, even if the photon energy is smaller than the bandgap (Fig. 2(b)). This phenomenon is referred to as multiphoton absorption. Such a high photon density can be easily obtained using femtosecond lasers due to the ultrashort pulse width. When multiphoton absorption occurs by two photons, it is called two-photon absorption.

In the regime of high laser intensity and low frequency, electron excitation can be induced by another nonlinear absorption process called tunneling ionization, rather than by multiphoton absorption. In tunneling ionization, the potential energy in the molecules is first significantly distorted by the intense electric field of the femtosecond laser, and then the length of the barrier is decreased, so that electrons can tunnel through the barrier. As a result, an electron can easily escape from a molecule to generate free electrons, as shown in Fig. 3.

The probability of each nonlinear absorption process, i.e., multiphoton absorption and tunneling ionization, in femtosecond laser interaction with transparent materials can be determined from the Keldysh parameter, γ[52]

$$\gamma = \frac{\omega}{e}\sqrt{\frac{m_e c n \varepsilon_0 E_g}{I}}, \quad (3)$$

where ω is the laser frequency, I is the laser intensity, m_e is the electron effective mass, e is the fundamental electron charge, c is the speed of light, n is the linear refractive index, ε_0 is the permittivity of free space, and E_g is the bandgap of the material. When γ is much greater (smaller) than 1, multiphoton absorption (tunneling ionization) is dominant. For $\gamma \approx 1$, absorption (photoionization) is induced by a combination of both processes. For waveguide writing in glass (described in Sec. IV D), the γ value is typically about 1. Thus, femtosecond lasers can induce strong absorption (electron excitation) even in transparent materials, thereby allowing for high-precision, high-quality micro- and nano-processing of transparent materials including glass.

Figure 4 shows SEM micrographs of monocrystalline sodium chloride (NaCl) ablated with (a) 16 ns and (b) 300 fs lasers at a wavelength of 248 nm, at which NaCl is transparent.[53] The femtosecond laser creates a cleanly ablated crater with good edge quality and no signs of thermal damage. In contrast, the nanosecond laser does not provide clean ablation. Multiphoton absorption can also be achieved with a nanosecond laser. However, the absorption cross section induced by a nanosecond laser is very small due to the relatively low peak intensity. Thus, the high absorption cross section achieved with a femtosecond laser is essential in order to achieve clean ablation. A much longer pulse width than the electron-phonon coupling time is another factor that can deteriorate ablation quality due to thermal effects, as described in Sec. II A.

C. Internal modification of transparent materials

One of the most exciting features of femtosecond laser processing is the unique capability of 3D processing inside transparent materials in a space-selective manner,[18,19] which is most relevant to the contents of this article. The probability of nonlinear absorption processes such as multiphoton absorption and tunneling ionization occurring is strongly dependent on the laser intensity. For instance, the absorption cross section for n-photon absorption is proportional to the n-th power of the laser intensity. Therefore, nonlinear absorption can be efficiently induced only at laser intensity above a specific critical value that is dependent on both the material and the pulse width. When a femtosecond laser beam is focused inside a transparent material with an adequate pulse energy, as shown in Fig. 5, nonlinear

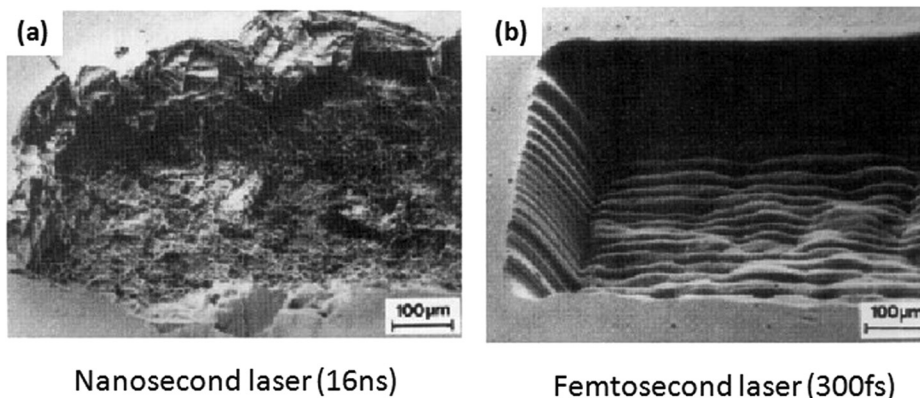
Nanosecond laser (16ns)

Femtosecond laser (300fs)

FIG. 4. SEM micrographs of monocrystalline sodium chloride (NaCl) ablated by (a) 16 ns and (b) 300 fs lasers at a wavelength of 248 nm. Reproduced with permission from S. Küper and M. Stuke, Microelectron. Eng. **9**, 475 (1989). Copyright 1989 Elsevier.
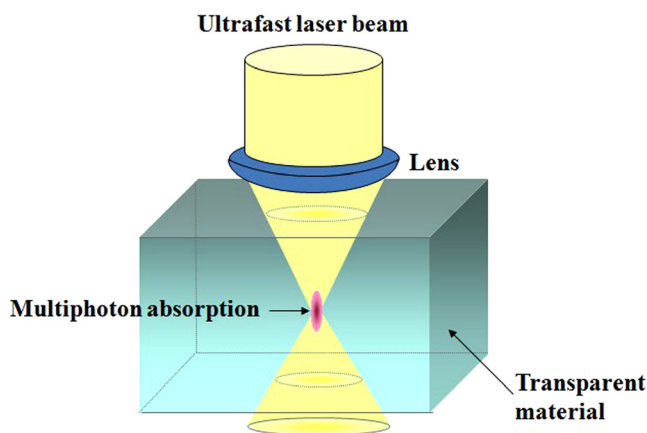
FIG. 5. Schematic diagram of the internal modification of a transparent material by nonlinear absorption processes such as multiphoton absorption and tunneling ionization using a femtosecond laser. Reproduced with permission from K. Sugioka and Y. Cheng, "Overview of ultrafast laser processing" in *Ultrafast Laser Processing*, edited by K. Sugioka and Y. Cheng (Pan Stanford, Singapore, 2013), p. 6. Copyright 2013 Pan Stanford.[211]

absorption can be confined to a region near the focal point inside the material where the laser intensity exceeds the critical value. In this way, internal modification of transparent materials and fabrication of structures inside them can be performed, but only using ultrashort pulse lasers. Internal modification is currently widely applied to TPP, photonic device and biochip fabrication, and glass bonding, as discussed below.

D. Nanoscale processing by improved spatial resolution

In Sec. II A, we discussed how femtosecond lasers minimize the formation of a HAZ due to suppression of heat diffusion to the processed area surroundings. This feature presents an advantage for yielding higher spatial resolution. Each pixel in a processed region almost corresponds to the spot size of the focused laser beam due to the negligible heat diffusion. The spot size ω_0 is determined by the diffraction limit ($\omega_0 = 0.61\lambda/\mathrm{NA}$, where λ is the laser wavelength and NA is the numerical aperture of the focal lens). For example, when an 800 nm wavelength femtosecond laser beam is

focused by an oil immersion lens with a NA of 1.4, a spot size of ca. 350 nm is achieved. Thus, the femtosecond laser can perform nanofabrication with a spatial resolution of less than a half wavelength. In addition, in the ideal case, the spatial intensity distribution for a femtosecond laser beam has a Gaussian profile. In many processes, including ablation, a threshold in the laser intensity exists, above which a reaction only occurs after absorption. By adjusting the laser pulse energy, in which only the central part exceeds the threshold intensity, the fabrication dimensions can be reduced to smaller than the laser spot size (threshold effect).

The use of nonlinear multiphoton absorption can further improve the spatial resolution.[54] For single-photon absorption (linear absorption), the spatial distribution of the laser energy absorbed by the material corresponds to the laser beam profile shown by a thick dashed line in Fig. 6. However, for multiphoton absorption, the distribution of the absorbed energy becomes narrower as the order (n) of the multiphoton absorption increases, because the effective absorption cross section for n-photon absorption is proportional to the n-th power of the laser intensity. Therefore, the effective beam size ω for n-photon absorption is expressed by

$$\omega = \omega_0/\sqrt{n}, \tag{4}$$

where ω_0 is the actual spot size of the focused laser beam. Figure 6 also shows the spatial distributions of the laser energy absorbed by transparent materials for two- (solid line) and three-photon (thin dashed line) absorption. From Eq. (4), it can be expected that multiphoton absorption can overcome the diffraction limit (ω_0) of a laser beam and thereby achieve sub-diffraction-limit resolution. It should be noted that better resolution can be achieved with multiphoton absorption than with single-photon absorption at the same wavelength. Single-photon absorption using a second harmonic, i.e., a half wavelength, provides better resolution ($\omega_0/2$) than two-photon absorption of a fundamental beam ($\omega_0/\sqrt{2}$), although the former process cannot be used to perform internal modification of transparent materials. Employing the threshold effect can further improve the fabrication resolution. For example, if the threshold intensity for the reaction is set to
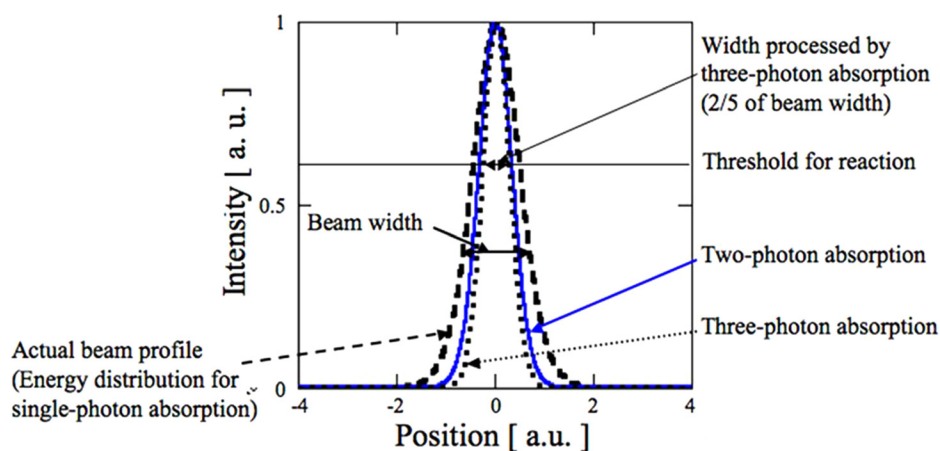
FIG. 6. Actual beam profile (thick dashed line) and spatial distributions of laser energy absorbed by materials through single- (thick dashed line), two- (solid line), and three-photon (thin dashed line) absorption. The solid horizontal line indicates the reaction threshold. Reproduced with permission from K. Sugioka and Y. Cheng, *Femtosecond Laser 3D Micromachining for Microfluidic and Optofluidic Applications*, Springer Briefs in Applied Science and Technology (Springer, London, 2014), p. 24. Copyright 2014 Springer.[210]

correspond to the solid horizontal line in Fig. 6, then the fabrication width can be reduced to 2/5th of ω_0.

In principle, the threshold effect provides no limit to the fabrication resolution, because the resolution can be significantly improved if the solid horizontal line in Fig. 6 is set to as near to the intensity at the center of laser beam as possible. Careful stabilization and control of the laser power has resulted in resolution better than 20 nm for TPP using a 780 nm femtosecond laser.[55] However, in practice, fluctuations of the femtosecond laser output power make fabrication of 3D nanostructures with such high fabrication resolution rather difficult. Thus, the typical resolution for the fabrication of 3D nanostructures by TPP is 100–200 nm.[54,56]

III. TPP

A. Principle of TPP

Laser stereolithography is classified as additive manufacturing, i.e., 3D printing, which can be used to directly create 3D structures. The initial concept was first reported in 1981, based on the use of UV light.[57] In this process, a focused UV laser beam (typically from a He–Cd laser) is scanned in the plane of the first layer of a photocurable epoxy resin in a vat on an elevator stage. The vertical position of the stage is adjusted to form a thin layer of epoxy resin on the stage. The epoxy resin is initially liquid, but it solidifies according to the laser beam trace by single-photon absorption. The elevator stage is then shifted down in the vat to form a second thin epoxy resin layer on the structure and the focused laser beam is scanned in the plane of the second layer. A 3D structure is thus fabricated by repeating this layer-by-layer process. Rapid prototyping of 3D structures by laser stereolithography (i.e., 3D photopolymerization) is already in commercial use for design verification, fabrication of working models, function and performance testing, fabrication of direct injection molding dies, and fabrication of medical models.[58]

The use of a near-IR femtosecond laser for stereolithography, which is transparent to the photocurable epoxy resin, enables the direct creation of 3D structures without shifting the elevator stage, due to internal modification based on two-photon absorption (see Fig. 7). Stereolithography performed using a near-IR femtosecond laser is termed TPP. TPP transforms small unsaturated molecules in the liquid state to macromolecules in the solid state due to polymerization reactions based on two-photon absorption. Only the epoxy regions where the laser beam is focused are solidified because the two-photon absorption can be confined in the focal volume. The unpolymerized resin is easily removed with a solvent during the subsequent developing process, leaving the remaining 3D structure. The fabrication resolution of femtosecond laser processing can go beyond the diffraction limit in a plane perpendicular to the laser beam axis, as described in Sec. II D. Furthermore, elimination of the stage shift improves the fabrication resolution along the direction parallel to the laser beam axis (better than the Rayleigh length dimension), because with mechanical shifting of the stage, it is difficult to create a uniform resin layer on the stage with a thickness less than several microns. Thus, TPP is currently used widely for the fabrication of 3D polymer micro- and nanostructures.

A solid resist can replace epoxy resin for the direct fabrication of 3D micro- and nanostructures. Complex 3D microstructures and topologically complex structures using organic photoactive materials (bis-donor phenylene vinylenes) have been successfully fabricated by two-photon absorption using a femtosecond laser.[59,60] Unlike epoxy resin, the solid resist can be used to perform not only bottom-up fabrication (additive manufacturing) but also top-down fabrication (subtractive manufacturing) by the selection of a suitable photoresist (negative- or positive resist). For example, a positive tone resist is suitable for the fabrication of a hollow microchannel embedded in a material.[61]

B. Fabrication resolution

In Sec. II D, we discussed the advantage of femtosecond laser processing that reduces the HAZ combined with nonlinear multiphoton absorption to overcome the diffraction limit and thereby enable nanofabrication with subwavelength resolution or smaller. The typical resolution of TPP for the fabrication of 3D nanostructures in a plane perpendicular to the laser beam axis (lateral resolution) is 100–200 nm, even though the laser wavelength is ca. 800 nm.[54,56] In contrast, the resolution along the beam axis (vertical resolution) is always several times larger than the lateral resolution, even when a high NA lens is used, due to the mismatch between the focal radius and the Rayleigh length of the focused laser beam.[62,63]

Precise setting of the laser intensity to very near the TPP threshold intensity coupled with control of the laser scanning speed enabled reduction of the fabrication resolution to ca. 1/50th of the laser wavelength (780 nm).[55] Polymer nanofibers were formed between two supports also fabricated using TPP. Figure 8(a) shows a 23-nm-wide nanofiber fabricated between two supports with a spacing of 600 nm at a pulse power of 30 mW and a scan speed of 600 μm/s. Increasing the scan speed to 700 μm/s with an increased pulse power of 35 mW resulted in the formation of an 18-nm-wide nanofiber as shown in Fig. 8(b). However, the reproducibility of nanofabrication at extremely high resolution is very poor because of the inherent sensitivity of the fabrication process to fluctuations of the femtosecond laser output power under these
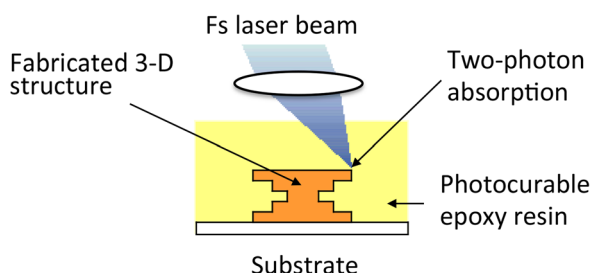

FIG. 7. Schematic illustration of direct fabrication of 3D microstructures by TPP using a near-IR femtosecond laser and a photocurable epoxy resin. Reproduced with permission from K. Sugioka and Y. Cheng, "Overview of ultrafast laser processing" in *Ultrafast Laser Processing*, edited by K. Sugioka and Y. Cheng (Pan Stanford, Singapore, 2013), p. 17. Copyright 2013 Pan Stanford.[211]

(a) Pulse power: 30 mW
Scan speed: 600 μm/s

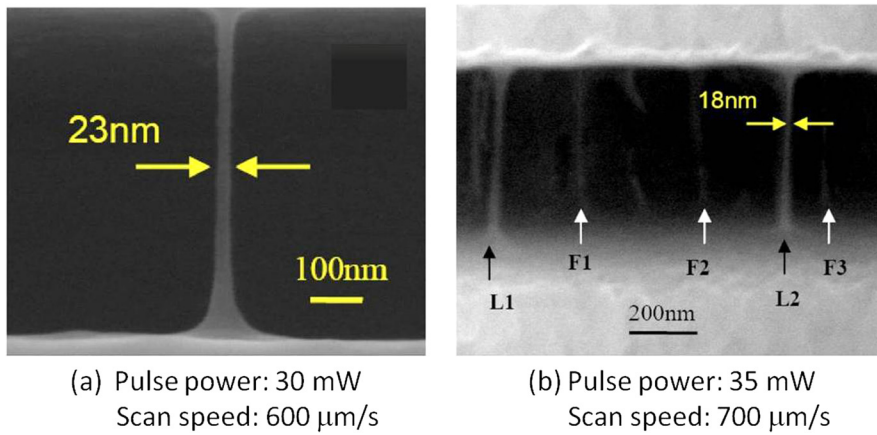(b) Pulse power: 35 mW
Scan speed: 700 μm/s

FIG. 8. SEM micrograph of suspended polymer nanofibers fabricated between two supports with a spacing of 600 nm at pulse power and scanning speeds of (a) 30 mW and 600 μm/s, and (b) 35 mW and 700 μm/s, respectively. Reproduced with permission from Appl. Phys. Lett. **90**, 071 106 (2007). Copyright 2007 AIP Publishing LLC.

conditions, which makes it difficult to regularly produce 3D nanostructures with this resolution.

A further effort to overcome the limitation of fabrication resolution for TPP was made based on the concept of stimulated emission depletion microscopy, which was originally developed for far-field nanoimaging of live cells.[64] In this scheme, two laser beams are employed. One is the activation beam with, e.g., a wavelength of 800 nm and a pulse width of 200 fs, which induces photopolymerization in a negative-tone photoresist, while the other is the deactivation beam operated at the same wavelength but in continuous wave mode, which is superimposed on the activation beam with a suitable lateral offset to deactivate the photoinitiator. With the deactivation beam, suppression of photopolymerization can be realized via the metastable intermediate energy states of the photoinitiators. This technique has been termed resolution augmentation through photo-induced deactivation (RAPID) lithography.[65] Compared with conventional TPP (Fig. 9(b)), typical RAPID lithography utilizes a doughnut-shaped deactivation beam to inhibit photopolymerization triggered by the activation beam at the doughnut ring, which results in an improvement of the fabrication resolution to less than 100 nm (Fig. 9(c)). Thus, RAPID lithography can realize a resolution comparable to electron beam lithography (Fig. 9(a)), which is not cost-effective and has no capability for 3D nanostructuring. Another important factor for achieving higher fabrication resolution by TPP is the mechanical strength of the solidified materials. By developing a two-photon absorption resin with a high mechanical strength, writing of polymer lines with widths of 9 nm and a two-line resolution of 52 nm, which is determined as the minimum center-to-center distance between the two fabricated lines, has been successfully demonstrated.[66]

C. Functionalization of materials

Resins typically used for TPP, such as SCR 500, SU-8, and NOA 61, do not result in polymers with specific
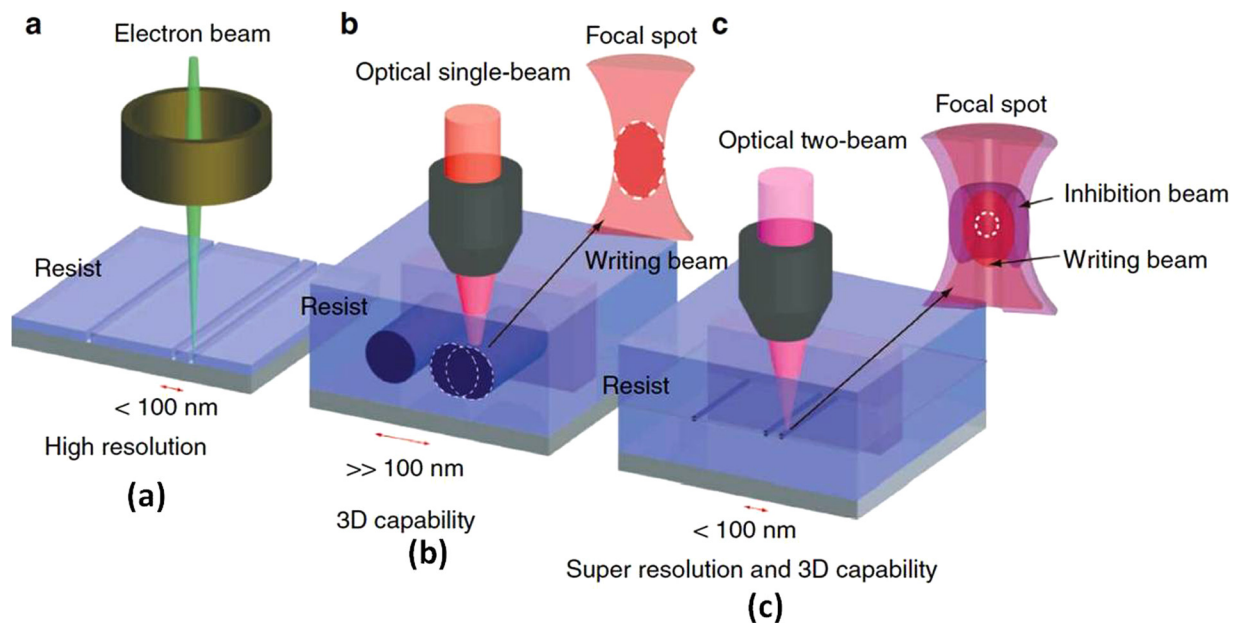

FIG. 9. Comparison of different lithography schemes. (a) Electron beam lithography with a high fabrication resolution of 10–20 nm, but without the capability of 3D fabrication. (b) Conventional TPP by a single beam that provides 3D fabrication capability with a resolution of 100–200 nm. (c) TPP by the combination of activation and deactivation beams to provide 3D fabrication capability with a resolution comparable to electron beam lithography. The image in the inset shows the focal spot of the activation beam and the doughnut-shaped deactivation beam. Reproduced with permission from Gan *et al.*, Nat. Commun. **4**, 2061 (2013). Copyright 2013 Nature Publishing Group.

functions. The incorporation of optical, electric, or mechanical functions into the polymers is highly preferable for many applications; therefore, functional polymer materials can be designed by doping specific substances into common resins.

3D multicolor luminescent microstructures have been realized by the *in situ* synthesis of semiconductor-polymer nanocomposites by TPP.[67] The resins consisted of precursors of CdS nanoparticles (cadmium methacrylates), monomers (methacrylic acid and methyl methacrylate), oligomers (dipentaerythritol hexaacrylate), photoinitiator (benzyl, 1 wt. %) and photosensitizer (2-benyl-2 -(dimethylamino)-4′-morpholinobutyrophenone, 1 wt. %). By tuning the cross-linking density of the polymer, the size of the CdS nanoparticles synthesized *in situ* within the polymer matrices could be controlled. The resultant nanocomposites exhibited unique tunable light emission from quantum size effects due to the controllable size of the CdS nanoparticles. Figure 10(a) shows SEM and fluorescence microscopy (FM) images of microbulls created using TPP. The microbull fabricated using the resin without a cross-linker emits a green colored fluorescence (center image in Fig. 10(a)). In contrast, a cyan color emission was successfully achieved by the *in situ* synthesis of CdS nanoparticles using a resin with 48.7 wt. % cross-linker content (right-hand image in Fig. 10(a)). Multicolor lizards with a 15 μm feature size have also been fabricated using the same procedure, as shown in Fig. 10(b). Such functional structures will be beneficial for micro- and nano-electromechanical systems (MEMS/NEMS) and integrated optical devices.

A common resin doped with surface-modified Fe_3O_4 nanoparticles imparts magnetic properties to 3D microstructures produced using TPP, which can then be remotely driven by a magnetic force.[68] The Fe_3O_4 nanoparticles were synthesized using the traditional Massart method. To fabricate magnetic micro/nanomachines, magnetic nanoparticles were mixed with a prepared photopolymerizable resin consisting of 37.14 wt. % methyl acrylate as a monomer,

60.00 wt. % pentaerythritol triacrylate as a cross-linker, 1.66 wt. % benzyl as a photoinitiator, and 1.20 wt. % 2-benzyl-2-(dimethylamino)-1-(4-morpholinophenyl)butan-1-one as a photosensitizer. The optimized doping rate for magnetic nanoparticles in the resin mixture was approximately 2.40 wt. % according to thermogravimetric analysis measurements. Using this magnetic photopolymerizable resin, various functional micromachines were fabricated by pinpoint laser writing. One of the interesting micromachines applications demonstrated is a remote-controllable microturbine.[69] Figure 11 shows a collar-joint microturbine that was successfully produced according to a predesigned model (Figure 11(a)). The total size of the microturbine is ca. 35 μm in diameter with a central axletree and three blades. A piece of ferromagnet placed on a vortical device was used to magnetically control the microturbine motion. The rotation speed could be controlled in the range of 0–6 rps. Such a microturbine could be applied for the remote control of micro/nanomachines, and would be of considerable interest in the field of microfluidics.

Direct femtosecond laser writing of protein (bovine serum albumin) facilitated by a photosensitizer (methylene blue) has made unique optical properties available in 3D microstructure fabrication based on photo-cross-linking in order to realize tunable microlenses.[70] The fabricated protein microlens could be swollen when immersed in a buffer solution, and the degree of deformation was dependent on the pH of the buffer solution. Thus, for a protein lens with a diameter of 40 μm, the focal length could be continuously tuned over a wide range from ca. 400 μm at pH 7.0 to ca. 600 μm at pH 13.0. Such unique protein-based microoptical devices are dynamically tunable and biocompatible, and will have potential use in optofluidic applications.

D. Photonic device fabrication

Microoptics comprise an important element for many applications such as microimaging, microfocusing, and beam shaping. The capabilities of 3D microfabrication and the almost unlimited geometry available with TPP allows for the preparation of various planar and 3D microoptical devices. The Fresnel zone plate (FZP) is an important microoptical component that is used for laser shaping and X ray imaging. Guo *et al.* fabricated both a spherical microlens array and an amplitude-type FZP using TPP with SCR500 resin.[71] The 15-μm-diameter spherical microlens produced a focal spot less than 0.5 μm in diameter, while the 17 μm diameter FZP produced a focal spot of ca. 2 μm, both of which were in good agreement with the theoretical simulation. Compared with an amplitude-type FZP, the phase-type FZP provides higher diffractive efficiency. Chen *et al.* fabricated a phase-type FZP by TPP with a diffraction efficiency of 68% for an eight-level lens, which was comparable to that for an FZP prepared using other techniques such as planar lithography, although the theoretical diffractive efficiency was 95.1%.[72] To date, diffractive efficiencies as high as 73.9% have been achieved for an eight-level phase lens produced using TPP with the SU-8 resin.[73] In addition, FZP arrays with fill
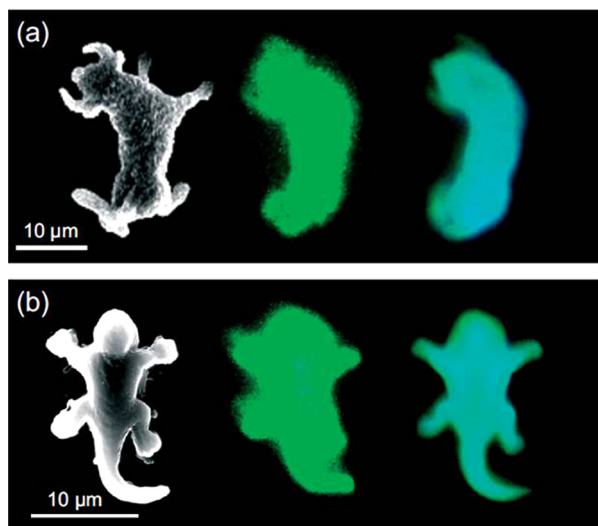

FIG. 10. SEM (left) and FM micrographs of (a) 3D microbulls and (b) 3D microlizards fabricated from resin without (center) and with (right) cross-linker. Reproduced with permission from Sun *et al.*, Adv. Mater. **20**, 914 (2008). Copyright 2008 Wiley.
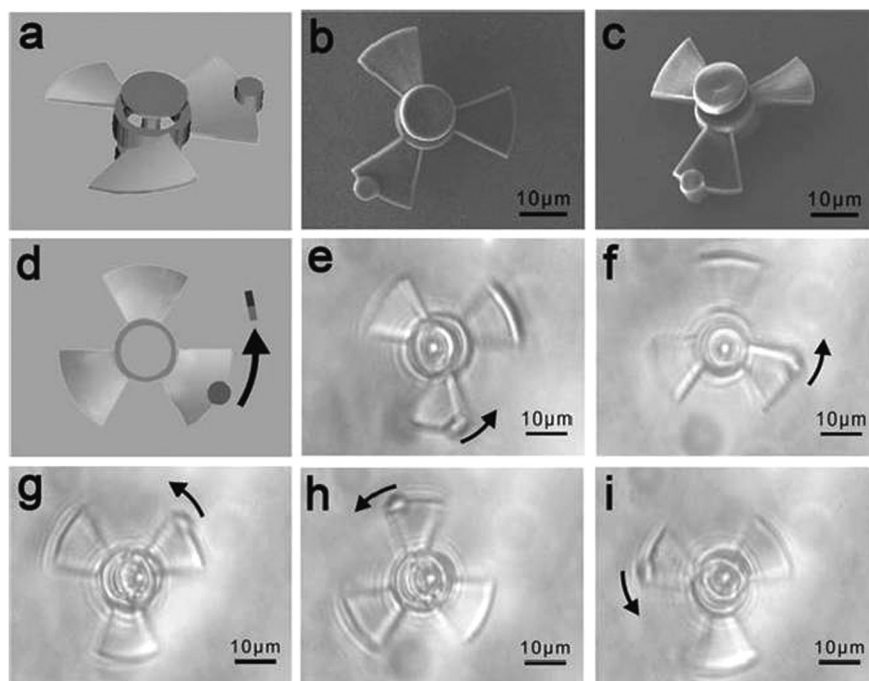
FIG. 11. Remote control of a microturbine in acetone. (a) 3D design model of the microturbine, (b) and (c) SEM micrographs of the microturbine, and (d) top-view scheme model for circumgyration. (e)–(i) Optical micrographs of the microturbine in a circumgyration cycle. For remote control and observation of the microturbine, a piece of ferromagnet was placed on a vortical device around the objective lens. Reproduced with permission from Xia *et al.*, Adv. Mater. **22**, 3204 (2010). Copyright 2010 Wiley.

factors of 100% have been fabricated that demonstrate excellent optical focusing and imaging performance.[74]

In addition to FZPs, TPP has been adopted to create Dammann gratings, which are optical elements used to split a beam and generate a coherent signal.[75] Each Dammann grating generated an array of 2×2, 3×3, 4×4, 5×5, and 6×6 spots for an incident He:Ne laser beam with a wavelength of 632.8 nm, and with theoretical diffractive efficiencies of 81.06%, 66.42%, 70.63%, 77.38%, and 84.52%, respectively. More interestingly, the Dammann grating could produce coherent patterns even when incoherent white light was incident as the input signal.

An even more attractive application of TPP for photonic device fabrication is the fabrication of photonic bandgap crystals. A photonic crystal has a 3D dielectric structure that generates a photonic bandgap, i.e., frequency window, to irrespectively forbid the propagation of electromagnetic waves with specific frequencies.[76,77] Thus, photonic crystals are very attractive optical elements for controlling and manipulating the propagation of light. Sun *et al.* demonstrated the first 3D photonic crystals produced using TPP, which consisted of 20-layer photonic structures with different in-plane rod spacings ($d = 1.2$, 1.3, and 1.4 μm).[78] All had planar dimensions of $40 \times 40 \mu m^2$ and exhibited the designed photonic bandgaps. The photonic crystals exhibited transmittance dips under normal incidence at wave numbers of 2553, 2507, and 2454 cm^{-1}. The unique capability of TPP for the production of 3D structures with almost unlimited geometries and with a fabrication resolution of 100–200 nm provides the opportunity to realize a variety of photonic crystals with diamond-lattice, cubic, woodpile, and spiral structures. Among these, a novel spiral architecture, which cannot be produced by conventional methods based on layer-by-layer fabrication, realized promising photonic bandgap properties; Seet *et al.* produced 3D spiral-architecture photonic crystals with design parameters of a = 1.8 μm,

L = 2.7 μm, and c = 3.04 μm (L = 1.5a, c = 1.69a), as shown in Figs. 12(a) and 12(b).[23] The structure has dimensions of ca. $48 \times 48 \times 30 \mu m^3$. Figure 12(c) shows reflectance and transmittance spectra measured along the z-axis for three different spiral photonic crystals fabricated with the same normalized lattice parameters (L = 1.5a, c = 1.69a), but with different absolute lattice periods of a = 1.2, 1.5, and 1.8 μm. Pairs of spectrally matching transmittance dips and reflectance peaks are observed at central wavelengths of 3.8, 4.7, and 5.2 μm for a = 1.2, 1.5, and 1.8 μm, respectively, which indicates that a smaller lattice period opens the photonic bandgap at shorter wavelength. At the shorter wavelength interval of 1.5–2.5 μm, similar pairs of dips and peaks were observed at central wavelengths of 2.0 and 2.48 μm, where a shorter wavelength also corresponds to a smaller lattice period. For the largest lattice period of a = 1.8 μm, the photonic bandgap was located in the intrinsic SU-8 absorption and then vanished. The introduction of defects into photonic crystals enables the transmission of specific wavelength light along the defects, which thereby act as a waveguide and is one of the key technologies for applications of photonic crystals. TPP has advantages in the introduction of defects over other fabrication techniques due to its highly flexible 3D fabrication capability.[23,79] Figure 12(d) shows a photonic crystal with L-shaped defects that was formed on the walls of the sample by missing parts of the spirals.[79]

E. Micro- and nanomachine fabrication

Micro- and nanomachines have attracted much attention due to their extensive applications in communication and transportation, biomedicine, the energy field, textile and food industries, and in security. In many cases, they are composed of movable microcomponents. TPP can be used to produce 3D microcomponents that float freely in a photocurable resin during the entire process, due to the high viscosity of
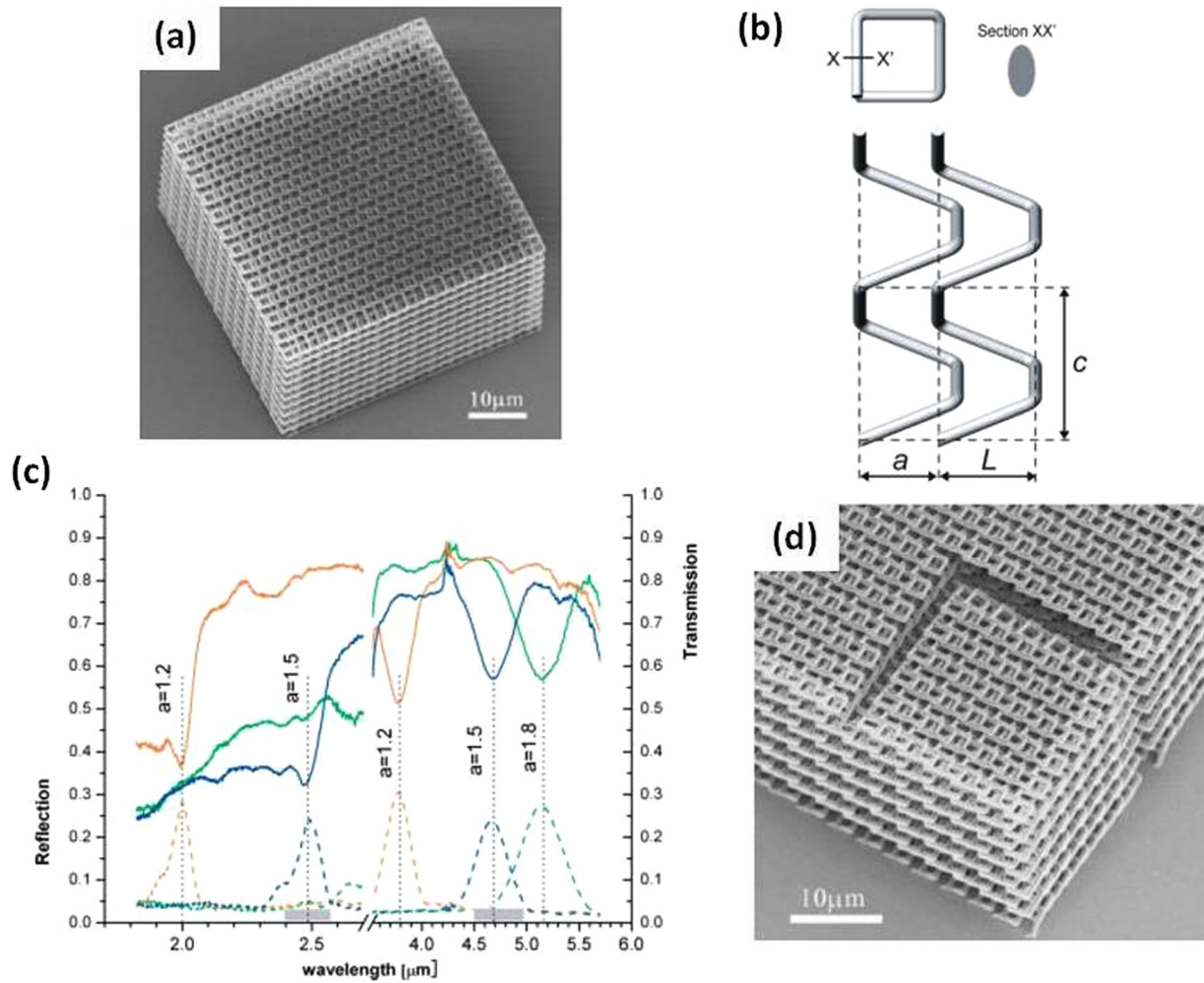
FIG. 12. (a) SEM micrograph of spiral architecture photonic crystals with parameters of a = 1.8 μm, L = 2.7 μm, and c = 3.04 μm (L = 1.5a, c = 1.69a). (b) Parameters of individual spirals separated from the structure. *L* is the length of the spiral arms and *c* is the vertical pitch of the spiral. The extended spiral structures are generated by creating the spirals on the nodes of a two-dimensional square lattice with period *a*. (c) Reflectivity and transmission spectra measured along the z-axis for three different spiral photonic crystals fabricated with the same normalized lattice parameters (L = 1.5a, c = 1.69a), but with different absolute lattice periods of a = 1.2, 1.5, and 1.8 μm. (d) A sample with L-shaped defects, which act as waveguides, formed on the walls of the sample by missing parts of the spirals. Reproduced with permission from Seet *et al.*, Adv. Mater. **17**, 541 (2005). Copyright 2005 Wiley.

the resin,[80] which is beneficial for the fabrication of movable microcomponents.

The magnetically driven microturbine shown in Fig. 11 was successfully fabricated using TPP with a photocurable resin doped with surface-modified Fe_3O_4 nanoparticles.[68] Microsprings that were fabricated by a similar technique were successfully elongated from an original length of 60 μm to a length of 81 μm by remote control under an external magnetic field.[69]

Polymers solidified by TPP from undoped photocurable resins are transparent to visible and near-IR light; therefore, they can be driven by optical forces. Figure 13(a) shows an SEM image of an optically driven microneedle fabricated using TPP,[21] and Fig. 13(b) shows a 3D schematic diagram of the optical manipulation. The movable part is free from both the substrate and the shaft. Such a distinct structure could be realized because the high viscosity resin fixed the position of movable parts during the entire TPP process. The probe tip (movable part) of the needle is attached to the slotted arm, so that this microneedle can perform both translational and rotational motion under laser trapping with a Ti:sapphire laser operated in continuous wave mode. The microneedle was applied to manipulate a micro-object in the liquid. Figures 13(c) and 13(d) illustrate the mechanical stimulation of a micro-object by the microneedle, where a tiny particle of dust floating in the liquid is pushed with the arm of the microneedle or pricked with its probe tip. Such optically driven micromachines will have application in nanosurgery on living cells and in single molecule nanoanalysis.

Micropumps are functional microcomponents that are widely used to control the flow rate of fluids in microfluidic devices. An optically driven micromachine can also act as a micropump, in which two lobed rotors are incorporated into a microchannel by TPP, as shown in Fig. 14.[81] The two built-in 9-μm-diameter rotors are cooperatively driven by optical trapping that employs time-divided scanning with a single laser beam. The velocity of trace particles in a liquid can be controlled in the range of 0.2–0.7 μm/s according to the rotation speed of the rotors. An optically driven micropump that employs viscous drag exerted on a spinning microrotor with left- and right-handed spiral blades on its rotational axis has been proposed in order to enhance the
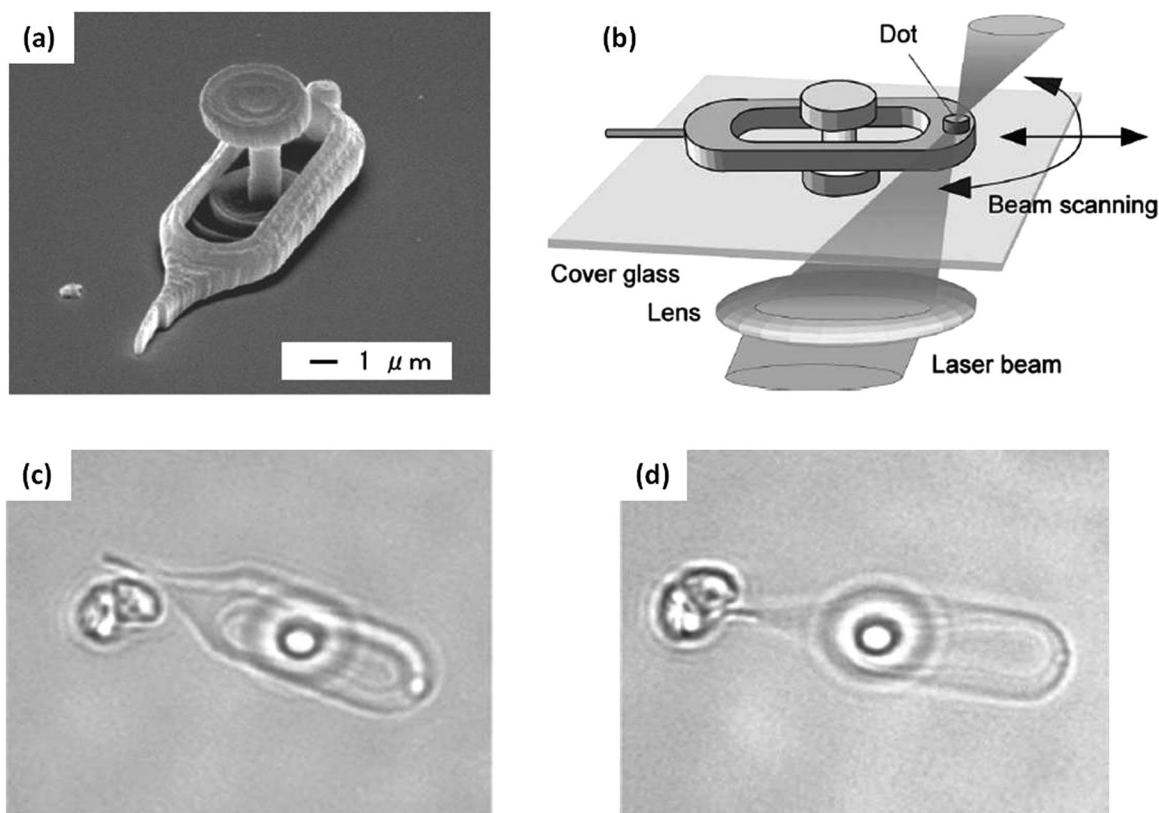
FIG. 13. (a) SEM micrograph and (b) 3D schematic for the optical manipulation of microneedles fabricated by TPP. (c) Pushing a micro-object with the arm of the microneedle. (d) Pricking a micro-object with the submicron probe tip of the microneedle. Reproduced with permission from Appl. Phys. Lett. **82**, 133 (2003). Copyright 2003 AIP Publishing LLC.

rotation performance of such micropumps and achieve higher flow rates.[82]

F. Functional microfluidic device fabrication

In the past two decades, much attention has been paid to microfluidic systems due to their broad range of applications in chemistry, biology, medicine, food science, environmental science, and material science, with distinct advantages of low sample consumption, high speed, high activity, high sensitivity, safety, and environmental benignity. The use of positive tone resists in TPP enables the fabrication of 3D
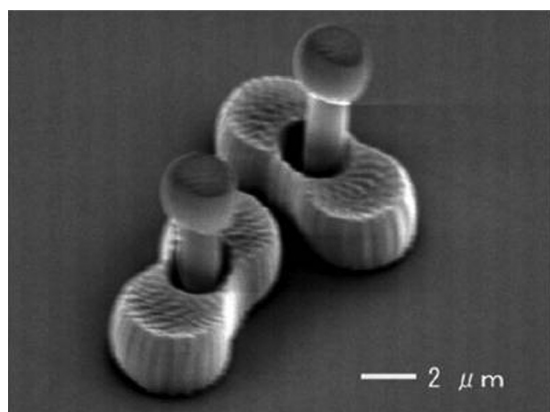

FIG. 14. SEM micrograph of a prototype lobed micropump fabricated by TPP. Reproduced with permission from Appl. Phys. Lett. **89**, 144 101 (2006). Copyright 2006 AIP Publishing LLC.

microfluidic structures embedded in a polymer material.[61] In contrast, negative tone resists or photocurable resins are adopted for the integration of 3D functional microfluidic components into microfluidic structures to functionalize the microfluidic devices. Currently, negative tone resists or photocurable resins have been much more widely investigated because positive tone resists have many competitive techniques, such as femtosecond laser 3D glass micromachining[10] (Sec. IV) and soft lithography.[83] Negative tone resists or photocurable resins are not used for fabrication of microfluidic structures, because much labor and time are required due to the bottom-up fabrication (a 100–500 nm scanning pitch is typically employed). For example, the time required to fabricate a 1 mm³ volume microfluidic structure exceeds 104 days, even when the scanning pitch is increased to as large as 1 μm. Therefore, TPP is generally used for integration of functional microcomponents into planar open microfluidic structures prepared using other techniques such as photolithography. Functional microfluidic systems that can perform controlled filtering of particles, high-efficiency mixing of different solvents, and individual guiding of different fluids have been successfully fabricated by the integration of TPP-fabricated microfilters,[84] mixers,[69,85] and overpasses[86] into open microfluidic channels, respectively. A more detailed review of TPP applications for microfluidic device fabrication is available in Ref. 9.

The efficient mixing of different kind of fluids in microfluidic channels is crucial because laminar flow is usually produced due to the low Reynolds number. Therefore, the

integration of a mixing functionality is desirable for many microfluidic applications. Micromixer devices for fluid mixing are classified into two categories, active and passive, according to the presence or absence of an external power source for operation. One example of the former is the magnetic-field driven microturbine shown in Fig. 11. In contrast, a passive micromixer is more simple and cost effective because it does not require movable parts or an external power source. Figure 15 shows a new concept 3D crossing-manifold micromixer integrated into an open microfluidic channel by successive procedures of conventional photolithography and TPP.[85] After integration of the micromixer in the channel by TPP, the microfluidic system was sealed with polydimethylsiloxane (PDMS) slabs with two inlet and one outlet holes. The integrated microfluidic device demonstrated efficient fluid mixing with a mixing efficiency as high as 93.9%.

Recently, TPP integration of functional microcomponents into closed microfluidic channels has been accomplished.[28,87] Figure 16 shows an optical micrograph of a microfilter integrated at the junction of a closed cross-shape microfluidic channel.[28] The inset shows an SEM image of the polymer microstructure formed by TPP on a glass surface for SEM observation, which consists of a 3D triangular structure with $1.3 \times 1.3 \, \mu m^2$ pores. The same structure was constructed in a commercial microfluidic channel to provide filtering functionality. The 3D space-selective microfabrication capability of this technique enables the integration of microcomponents by post-processing inside closed microfluidic structures, such as in a chip that has been fabricated using standard technologies. The microfilter-integrated microfluidic system was tested with a suspension of $3 \, \mu m$ polystyrene spheres in a Rhodamine 6G solution and demonstrated high performance in that the microspheres were completely stopped at the microfilter while the Rhodamine 6G molecules passed through.

G. Medical and tissue engineering applications

Biomedical applications of TPP are also extensively investigated. One of the distinct applications in this field is the fabrication of medical microdevices.[88–90] Biocompatible
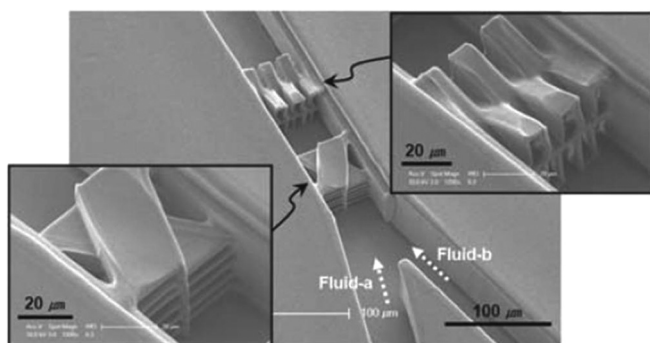

FIG. 15. SEM micrograph of a new concept 3D crossing-manifold micromixer integrated into a Y-shaped open microfluidic channel using conventional photolithography and TPP. Reproduced with permission from Lim *et al.*, Lab Chip **11**, 100 (2011). Copyright 2010 the Royal Society of Chemistry.
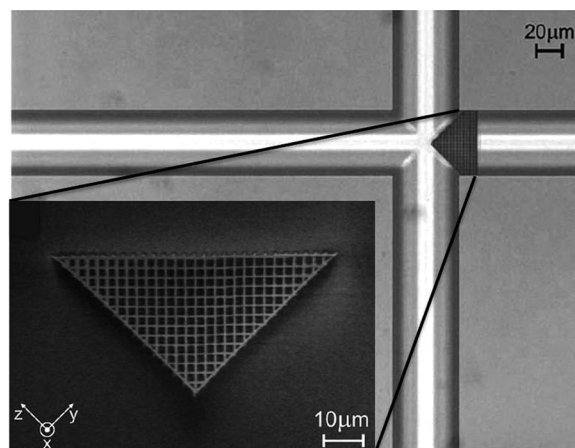

FIG. 16. Optical micrograph of a microfilter integrated at the junction of closed cross-shape microfluidic channels. The inset shows an SEM micrograph of the polymer microstructure formed on a glass surface by TPP. The same structure was constructed in the microfluidic channel. Reproduced with permission from Amato *et al.*, Lab Chip **12**, 1135 (2012). Copyright 2012 The Royal Society of Chemistry.

photopolymers are used for this purpose. One such example is an implantable MEMS, as shown in Fig. 17(a).[88] This microdevice consists of a check microvalve, designed to prevent the reversal of blood flow in human veins, such as that caused by standing for too long. The valve can open for forward fluid flow, but closes firmly to prevent backward flow. Part of the valve cover was intentionally deconstructed here (Fig. 17(a)) for visualization of the interior. TPP can also be used to fabricate drug-delivery devices, such as the microneedle arrays used for transdermal drug delivery[88] shown in Fig. 17(b).

Furthermore, TPP has been applied to fabricate scaffolds for tissue engineering. The scaffolds are artificially structured components capable of supporting cell attachment/migration for subsequent tissue development, which is important for understanding a variety of physiological and pathological processes, such as embryonic development, cancer metastasis, blood vessel formation and remodeling, tissue regeneration, immune surveillance, and inflammation. A scaffold fabricated by TPP from a biocompatible polymer material has a 3D structure composed of micrometer-sized pores, as shown in Fig. 17(c).[88] To explore cell migration, the green fluorescent protein (GFP)-labeled human fibrosarcoma cell line HT1080 was seeded in the scaffold at a density of 500 000 cells ml^{-1}.[90] Figure 18(a) shows a top-view bright-field image of the scaffold taken 5 h after cells were seeded inside the scaffold, which had a pore size of 52 μm. Initially, the cells are located only on the cover slip. However, after a few hours, the cells begin 3D migration throughout the scaffold, as shown by the 3D-rendered image of GFP-labeled cells in Fig. 18(b). The cells attach and move predominantly along the beams in a scaffold with 110 μm pores (Fig. 18(c)), while they occupy the entire pore in scaffolds with smaller pores. In addition, the cells are more uniformly dispersed inside the 52 μm pore scaffold than inside the 25 μm and 12 μm pore scaffolds (Figs. 18(d)–18(f)). It has thus been concluded that the mean speed of migration decreases as the pore size of the 3D matrix is decreased, due
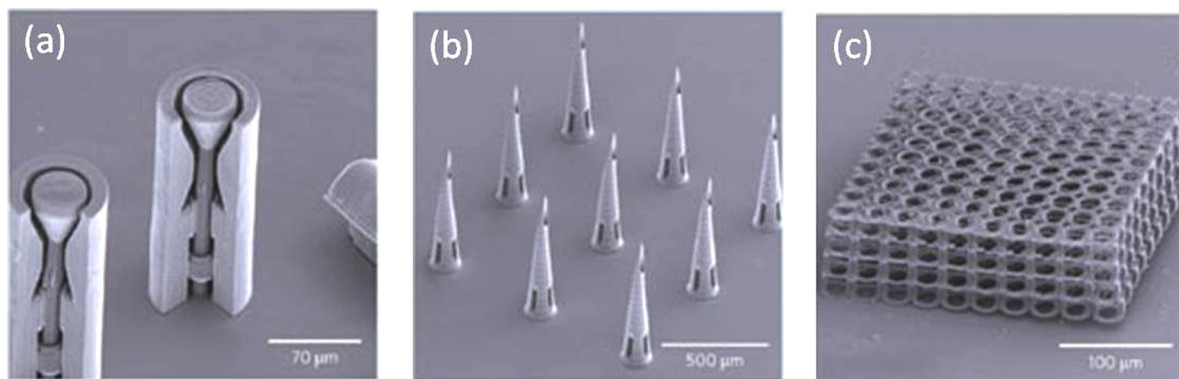
FIG. 17. (a) A check microvalve designed to prevent the reversal of blood flow in human veins. Part of the valve cover was intentionally deconstructed to show the interior. (b) Test microneedle arrays used for transdermal drug delivery. (c) Tissue engineering scaffold produced using TPP from a biocompatible polymer material. Reproduced with permission from M. Farsari and B. Chichkov, Nat. Photonnics **3**, 450 (2009). Copyright 2009 Nature Publishing Group.

to obstruction from the matrix. The scaffolds prepared by TPP have significant potential for systematic studies on the effects of mechanical properties, adhesion peptide concentrations, and biodegradability on cell migration in 3D environments.

H. Fabrication of 3D metal micro- and nanostructures

Instead of a photocurable resin, the use of either a sol-gel matrix,[91] a polymer composite containing metal nanoparticles and a silver salt,[92] a metal-ion solution,[93,94] or a polymer film containing silver ions[95] has also enabled the formation of 3D metal micro- and nanostructures by femtosecond laser direct writing based on multiphoton

absorption. This technique has been termed multiphoton photoreduction.

One of the materials used for the fabrication of 3D metal micro- and nanostructures consisted of diammine silver ions (DSI) as a silver source and a nitrogen atom-containing alkyl carboxylate (n-decanoylsarcosine sodium; NDSS) as a surfactant.[94] The concentration of silver ions was set at 0.05 M. Femtosecond laser irradiation was tightly focused at the interface between the metal-ion solution and a cover slip glass substrate using an oil immersion objective lens with a NA of 1.4. A free-standing silver pillar structure with a minimum feature size of 180 nm was formed as the undesirable formation of metallic particles was inhibited by the introduction of the surfactant, as shown in Fig. 19(a). Thus, an array of truly free-standing 3D 5-μm-high silver pyramids was
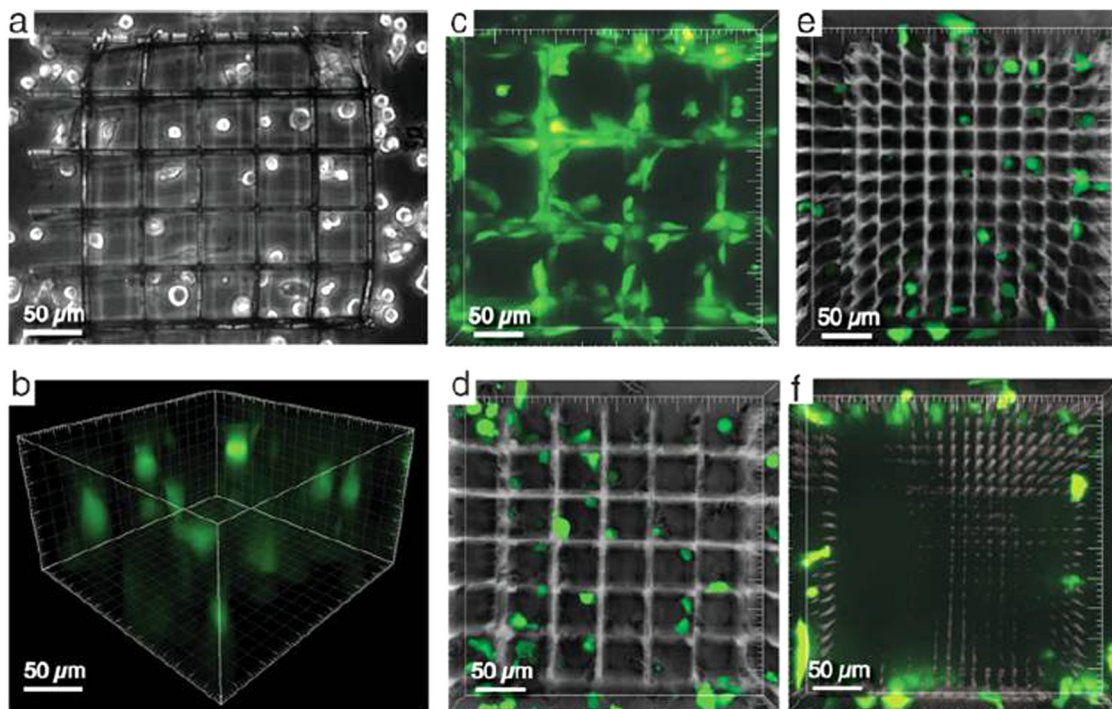
FIG. 18. (a) Bright-field optical micrograph showing a top-view of cells inside a scaffold with 52 μm pores, 5 h after of cell seeding. (b) Fluorescence image showing isometric 3D rendered view of HT1080 cells inside a scaffold 24 h after cell seeding. (c)–(f) Top-view overlay of fluorescence and differential interference contrast images of cells in scaffolds with 110, 52, 25, and 12 μm sized pores showing non-uniformity in the distribution of cells in different matrices due to variations in physical obstructions. Reproduced with permission from Tayalia *et al*., Adv. Mater. **20**, 4494 (2008). Copyright 2008 Wiley.

FIG. 19. Free-standing nanostructures produced by femtosecond laser multi-photon photoreduction using a metal-ion solution. (a) SEM micrograph of a free-standing silver pillar formed on a cover slip. (b) SEM micrograph of silver pyramids. The inset on the left shows a top-view of the silver-pyramid array. The inset on the right shows a close-up view of a silver pyramid. Reproduced with permission from Appl. Phys. Lett. **89**, 113 102 (2006). Copyright 2006 AIP Publishing LLC.
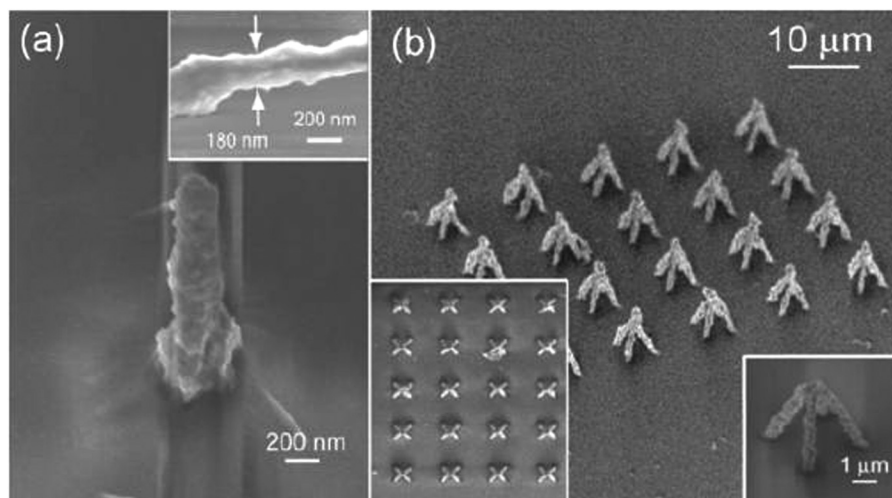
successfully constructed with each edge at a 60° angle to the substrate.

Another scheme for the fabrication of 3D metal micro-structures is the use of polyvinylpyrrolidone (PVP) films containing silver ions.[95] Figure 20 shows the experimental procedure for this technique. First, 1.25 g of PVP was dissolved in 50 ml of ethanol. The prepared PVP solution was then mixed with a solution of AgNO$_3$ in deionized water. To form a thin film containing silver ions, the mixed solution was spread onto a glass cover slip or stored in wells made of dimethylpolysiloxane and then heated in air at 100 °C for 10 min. Femtosecond laser irradiation was then focused on the sample using an objective lens with a NA of 1.25 for the fabrication of metal microstructures based on two-photon photoreduction. After laser direct writing, the sample was soaked in ethanol to remove the polymer matrix and then rinsed with deionized water. As a result, 2D and 3D metal microstructures remained on the glass substrate. The electrical resistivity of a continuous silver microstructure was measured to be 3.47×10^{-7} Ω m.

3D patterning of metal structures with micro- and nano-geometries has attracted much attention in various fields including plasmonics, electronics, bioscience, and chemistry.

IV. INTERNAL PROCESSING OF TRANSPARENT MATERIALS

A. Principle and scheme of internal processing

In the past two decades, irradiation of transparent materials with tightly focused, intense ultrafast laser pulses has led to many intriguing phenomena, such as refractive index modification,[18] the formation of nanovoids and periodic nanogratings,[96–98] element redistribution,[99] nanocrystallization,[100] and, very recently, the quill writing effect.[101,102] The combination of internal modification with a direct writing scheme has established the internal processing of transparent materials using femtosecond lasers, which has emerged as an important branch of materials processing with femtosecond lasers. Currently, optical waveguide writing has become an enabling technology for the construction of integrated photonic circuits (e.g., photonic lanterns and quantum circuits). The monolithic integration of microfluidic and optofluidic systems (e.g., lab-on-a-chip devices and micro-total analysis systems) has also benefited from internal femtosecond laser processing. The two enabling approaches for microfluidic and optofluidic applications are femtosecond laser-assisted chemical wet etching and water-assisted femtosecond laser 3D drilling. Here, the principles and major procedures involved in these technologies are described.

Optical waveguides are typically written in transparent materials such as glass, crystals, and polymers by inducing permanent refractive index changes in the focal volumes of tightly focused femtosecond laser pulses. It is generally considered that the changes in refractive index are a synergetic effect of several interaction phenomena, including color center formation, densification and stress production, element redistribution, thermal diffusion and accumulation; however, the actual contributions have not been quantitatively determined and are different for different types of materials.[11] Currently, glass materials, particularly fused silica, are the most intensively investigated materials for waveguide writing. In comparison with polymers, glass can offer better chemical stability and optical properties. In addition, glass is generally cheaper and more easily processed than crystals
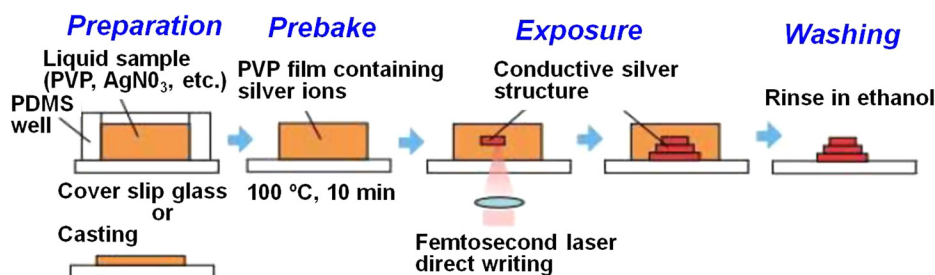

FIG. 20. Experimental procedure for the fabrication of 3D metal microstructures by femtosecond laser induced metal ion reduction using a PVP film containing silver ions. Reproduced with permission from S. Maruo and T. Saeki, Opt. Express **16**, 1174 (2008). Copyright 2008 The Optical Society of America.

using femtosecond lasers. Fused silica has another unique advantage, in that irradiation with a femtosecond laser in this material can induce an increased etching rate in hydrofluoric acid (HF) at the modified regions, which has allowed the single-step integration of microfluidic networks and optical waveguides for optofluidic applications. Another interesting glass that has also attracted significant attention is the photosensitive glass Foturan. Similar to fused silica, optical waveguides can be inscribed in Foturan glass, and exhibit a reasonable propagation loss of the order of 0.5 dB/cm.[103] Moreover, microfluidic structures can be fabricated in Foturan glass with a higher throughput than for fused silica because of the intrinsic photosensitivity of Foturan and the higher etching rate of regions modified by femtosecond laser irradiation.[104]

Besides glass, optical waveguides have also been written in crystals and polymers using femtosecond lasers.[15,17,105,106] Crystals can usually provide superior mechanical, thermal, and nonlinear optical properties than glass, which are desirable for applications ranging from wavelength conversion to miniaturized lasers. Polymers are cheaper and easier to manufacture than glass and crystals, which is advantageous for high-throughput production of low-cost photonic and microfluidic chips. However, when compared with most types of glass and crystals, polymers have poorer chemical durability and/or biological compatibility, in addition to inferior optical properties such as a narrower transmission window and a higher scattering loss.

A typical scheme for waveguide writing with femtosecond laser pulses is illustrated in Fig. 21. For most applications, a transverse writing scheme (i.e., translation of the sample perpendicular to the beam propagation direction) is preferred because it offers the maximum degree of flexibility in terms of the length and geometry of the fabricated structures. However, the transverse writing scheme inevitably gives rise to an elliptical focal spot elongated along the laser propagation direction. Several techniques for the correction of undesirable cross-sectional shapes will be discussed in Sec. IV B. To write high-quality optical waveguides with ideal cross-sectional shapes, minimal propagation losses, and
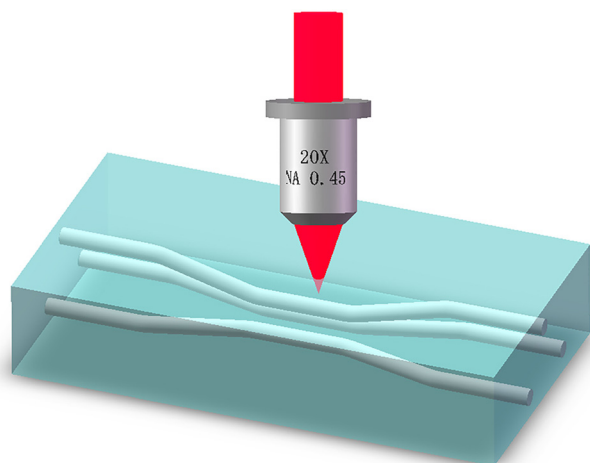

FIG. 21. Femtosecond laser writing of optical waveguides in transparent materials using a transverse writing scheme.

highest coupling efficiencies with other optical elements, care should be specifically given to the irradiation conditions, which are determined by a variety of parameters including the wavelength, polarization, pulse energy, pulse duration and pulse repetition rate of the femtosecond laser, the NA of the focal lens, and the translation speed of the motion stage.[11,107] It should be noted that these parameters must be optimized for each material being processed, because nonlinear multiphoton absorption relies on not only the peak intensity and pulse duration of the laser pulses but also the bandgap and thermal characteristics of the transparent material. The laser power used for writing the optical waveguides within glass should typically be slightly higher than the ablation threshold on the surface of the glass. The translation speed of the motion stage is largely determined by the repetition rate of the femtosecond laser. However, the translation speed should be sufficiently slow to ensure overlap between the focal spots of two successive pulses, although it should be reasonably high to maximize the fabrication throughput. Thus, a high translation speed can only be achieved when using a high-average-power femtosecond laser operated at a high repetition rate. Such femtosecond laser systems have become available recently. Optimization of the irradiation conditions is a troublesome and time-consuming process that is usually achieved by comparison of the propagation losses of waveguides written under various conditions. However, once a set of optimal irradiation conditions is determined for a certain combination of laser source, material to be processed, and geometry of the optical waveguide, then high-performance waveguides can be fabricated with high reliability and reproducibility.

Microfluidic devices, which incorporate microfluidic structures for the control and manipulation of small volumes of liquids with high precision and ease of operation,[108,109] have led to the miniaturization of systems for chemical and biological studies. The most popular microfluidic fabrication technology is soft lithography, which employs PDMS substrates.[83] Although soft lithography is rapid and cost effective, it cannot be used to directly form 3D microfluidic structures, such as buried microchannels and microchambers, without stacking and bonding. This difficulty can be overcome by internal processing with a femtosecond laser and is achieved by two different technical approaches, i.e., femtosecond laser-assisted chemical wet etching and water-assisted femtosecond laser 3D drilling, which were developed in late 90 s and early 2000 s, respectively.[110–112]

Figure 22 schematically illustrates the process used to fabricate a 3D microfluidic structure in the photosensitive glass Foturan, which include (1) formation of a latent image by femtosecond laser direct writing (Fig. 22(a)), (2) transformation of the latent image into an etchable phase by thermal treatment (Fig. 22(b)), and (3) selective removal of the modified material by wet chemical etching in a 5%–10% aqueous solution of HF acid in an ultrasonic bath (Fig. 22(c)).[113] The ultrasonic bath is critical because it can significantly enhance the etch rate by increasing the mass transfer of the chemical etchant in the thin channel. Likewise, microfluidic structures can also be fabricated in fused silica; however, in this case, chemical etching is performed immediately after the

(a)   **(b)**   **(c)**

Step 1: Fs laser direct writing   **Step 2: Heat treatment 505℃ 1hr - 605℃ 1hr**   **Step 3: Ultrasonic etching in 10% HF solution**
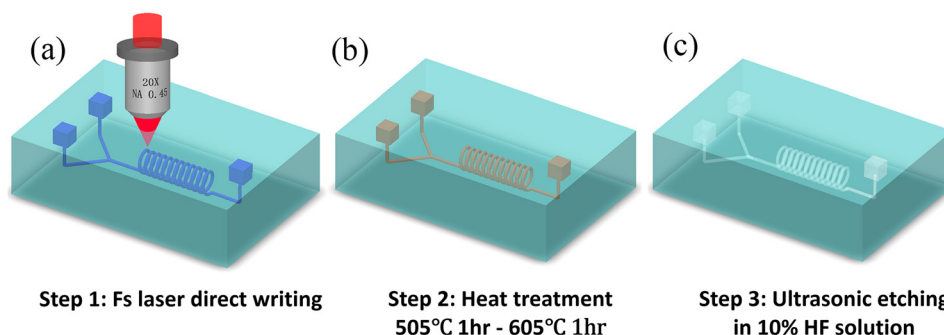
FIG. 22. Schematic illustration of the procedures used to fabricate 3D microfluidic structures in photosensitive glass. (a) 3D latent images are written in photosensitive glass by femtosecond laser direct writing. (b) Samples are subjected to programmed heat treatment to develop the modified region. (c) Samples are soaked in an aqueous solution of hydrofluoric acid in an ultrasonic bath to selectively etch the laser irradiated regions to leave hollow microfluidic structures in the glass.

exposure process and without the need for thermal treatment.[111] The mechanism behind such a difference is that for Foturan glass, which is a photosensitive glass doped with silver ions, femtosecond laser irradiation only reduces the silver ions to silver atoms by providing free electrons generated through multiphoton ionization. Therefore, thermal treatment must be used to first initiate the agglomeration of silver nanoparticles and then grow a crystalline phase of highly etchable metasilicate using the silver nanoparticles as nuclei. In contrast, for fused silica, exposure to the femtosecond laser can directly weaken the chemical bonds, which results in an enhanced etch rate with some chemical etchants. For both fused silica and Foturan, the typical etchant is a 5%–10% aqueous solution of HF acid. The different modification mechanisms mean that the minimum diameter of the microfluidic channels that can be fabricated in Foturan glass is a couple of micrometers, whereas that for fused silica can be as small as ca. 500 nm. The reason that it is difficult to reduce the diameter of the microfluidic channels fabricated in Foturan glass to less than 1 μm is because the space-selective modification of the etch rate in Foturan glass is achieved by formation of a crystalline phase of lithium metasilicate in the regions modified by femtosecond laser irradiation and subsequent heat treatment. The crystallites of lithium metasilicate, which have a much higher etch rate than the unmodified glass matrix, must be grown to a certain size (a few microns) to form an etchable network. In contrast, this limitation is not present in fused silica, but instead the main limiting factor for the fabricated channel diameter is the focal spot size due to the diffraction limit. It should be stressed that the microfluidic channel diameter is also dependent on the total length of the channels because of the limited etching selectivity. An etching selectivity of the order of 1:50 can be typically achieved in Foturan and fused silica when using diluted HF acid as the etchant. Thus, when the length of the microfluidic channel is increased, the channel will become significantly wider near the opening area, which leads to a tapered structure. Recently, Kiyama et al. reported that for fused silica, the replacement of HF acid with KOH led to significantly improved selectivity between the modified and unmodified regions by femtosecond laser irradiation, which allowed high-aspect-ratio microfluidic channels with extended lengths to be produced.[114] A

drawback is that the absolute etch rate in KOH etchant is too low, and thus a significantly longer time is required for the etching process in KOH than in HF acid. It should be noted that chemical wet etching can significantly benefit from ultrasonic assistance, which speeds up circulation of the fresh chemical etchants in the thin microfluidic channels. Besides glass, Choudhury et al. reported the preferential removal of femtosecond laser irradiation-modified regions in Nd:YAG crystals using a 50% aqueous H_3PO_4 solution as an etchant, with an etching selectivity as high as $1:10^4$.[115] This interesting finding provides a new possibility for the fabrication of crystal-based microfluidic chips that may incorporate active optical functions, such as nonlinear wavelength conversion and the generation of laser emission with optical waveguide writing using femtosecond laser pulses.

A counterintuitive phenomenon in the fabrication of microfluidic structures in fused silica is the strong dependence of the etch rate on the polarization of the writing beam. The mechanism behind this phenomenon is the formation of periodic nanograting-like structures in regions irradiated with linearly polarized femtosecond laser pulses. The nanogratings are intrinsically oriented perpendicular to the polarization of the writing laser beam; therefore, the etching selectivity can be enhanced by arranging the polarization of the laser pulses perpendicular to the direction of sample translation.[96,116] Further details on nanograting formation with femtosecond laser irradiation will be discussed in Sec. IV C.

Femtosecond laser-assisted chemical etching is compatible with optical waveguide writing because both technologies are based on femtosecond laser direct writing and can be simultaneously applied to a single substrate, so that the combination of these techniques has led to a wide range of novel optofluidic devices, which will be discussed in Sec. IV D. However, selective chemical etching can only be induced by femtosecond laser irradiation in a few dielectric materials. To broaden the coverage of materials, Li et al. developed a simple but powerful technique for the fabrication of 3D microfluidic structures in an almost unlimited number of transparent materials.[117] Another advantage of this technique is the higher fabrication resolution than that achieved by femtosecond laser-assisted chemical etching because this technique relies on ablation, which means that

the fabrication resolution is determined by the spatial energy distribution of the focused laser beam.[118] This technique, frequently called water-assisted femtosecond laser 3D drilling, employs femtosecond laser 3D drilling from the rear surface of glass in contact with distilled water, so that the water introduced into the microchannel facilitates efficient removal of the ablated debris. However, when the length of the microchannel increases, it becomes increasingly difficult to quickly introduce water into the narrow channel. In such a case, the debris produced during ablation is redeposited in the microchannel and causes blockages, so that the drilling process terminates. The length of the fabricated microchannels typically reaches only a few millimeters (i.e., <5 mm). Recently, Li and Qu demonstrated that by connecting a pressurized water tube to the opening of the 3D microchannel, water can enter the microchannel more easily during the drilling process, so that debris can be more efficiently removed, which allows longer channels to be produced, such as that with a total length of ca. 2.1 cm described in Sec. IV E.[119]

To promote the widespread application of 3D microfluidic structures, it is necessary to further increase the total length of the fabricated microchannels, which is so far still much less than that of microchannels fabricated by planar lithographic fabrication technologies. Even so, novel nanofluidic systems have attracted tremendous attention for their potential applications ranging from nanoscale fluid control to single molecule manipulation. Liao et al. have developed a technique based on femtosecond laser induced ablation in porous glass immersed in water that enables hollow structures with various geometries and configurations to be produced.[120] The composition of the porous glass is approximately 95:5SiO$_2$-4B$_2$O$_3$-0:5Na$_2$O (wt. %). Pores with a mean size of 10 nm are distributed uniformly within the glass and occupy 40% of the glass volume. In particular, the pores form a 3D connective network, which allows water to flow through. The water plays a key role in this process, in that bubbles are continuously generated around the ablation area due to the presence of water. The bubbles are then driven out from the microchannel by strong shock waves induced by femtosecond laser ablation. When the bubbles leave the microchannel from the opening, the generated debris is carried with them and the water circulation is accelerated.[121] The fabricated sample is then annealed to collapse all the nanopores. Figure 23 shows a schematic illustration of the fabrication process. This technique has enabled the fabrication of microfluidic channels in glass with almost unlimited lengths and arbitrary 3D geometries; long square-wave-like microchannels, large-volume microfluidic chambers, and 3D passive microfluidic mixers have been realized.[122] The fabrication resolution of this technique is determined by the spatial energy distribution, similar to the case of water-assisted femtosecond laser 3D drilling.

Recently, nanofluidic channels with transverse widths down to 40 nm were directly fabricated in silicate glass by combining the formation of hollow nanogratings in the glass and the threshold effect.[123] The formation of nanogratings in glass with linearly polarized femtosecond laser pulses is an exotic interaction phenomenon, of which the mechanism has not yet been elucidated.[96,97] The nanogratings formed in
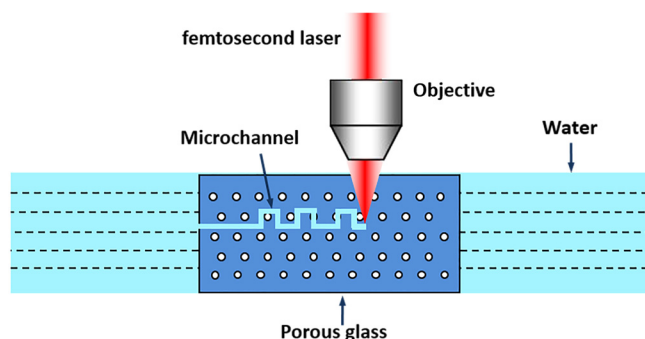

FIG. 23. Schematic illustration of the fabrication of 3D microfluidic structures by femtosecond laser direct writing in porous glass immersed in water. Reproduced with permission from Liao et al., Opt. Lett. **35**, 3225 (2010). Copyright 2010 The Optical Society of America.

fused silica glass are typically composed of alternated regions of high and low etching rates.[116] Interestingly, the nanogratings formed in porous glass contain an array of hollow nanocracks due to the porosity of the glass, as shown by the green areas in Fig. 24. If the femtosecond laser intensity is intentionally reduced to a level at which only the intensity in the blue region of Fig. 24 is higher than the threshold intensity, then only a single nanocrack in the central area of the focal volume is produced. The single nanocracks produced during femtosecond laser beam scanning can thus be connected into a continuous nanofluidic channel, the continuity of which has been confirmed by observation with a fluorescent dye solution.

B. Control of cross-sectional shapes

Optical waveguides and microfluidic channels fabricated in transparent materials by femtosecond laser direct writing are essential building blocks for the construction of complex 3D photonic circuits and microfluidic networks. Therefore, control of the cross-sectional shapes of the waveguides and microfluidic channels is necessary. For instance, to achieve
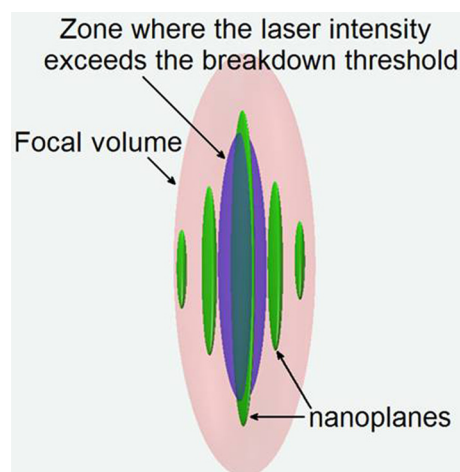

FIG. 24. Schematic illustration of how the channel width is narrowed far beyond the optical diffraction limit. When the laser intensity is decreased to some extent, only the central nanochannel could be induced while other nanograting-like channels vanish. Reproduced with permission from Liao et al., Lab Chip **13**, 1626 (2013). Copyright 2013 The Royal Society of Chemistry.

single-mode propagation and efficient coupling with external fibers, the cross section of optical waveguides should be round. Likewise, in many microfluidic applications, circular cross sections are preferable to rectangular cross sections in order to mimic the environment in blood vessels, because rectangular cross sections induce non-physiological gradients in the fluid shear rate, velocity, and pressure.

If optical waveguides or microfluidic channels have large cross-sectional areas (i.e., diameters of several tens of micrometers, which is significantly larger than the femtosecond laser wavelength), then the cross-sectional shape can be tailored by overlapping multiple laser-affected zones.[124] In contrast, small diameter optical waveguides and microfluidic channels are typically produced using a single-scan transverse writing technique, in which the sample is translated perpendicular to the incident beam. In this case, a single focal lens generates a focal spot that is elongated in the direction of the incident laser beam, which results in waveguides or microfluidic channels with elliptical cross sections. In addition, the asymmetry of the cross section becomes more severe when focal lenses with low NAs are used. For many practical applications, low-NA lenses are more useful than high-NA lenses because of their larger working distances. Several beam shaping techniques have been developed to overcome this problem and produce microfluidic channels with circular cross sections. Typical shaping techniques include astigmatic beam shaping,[125] slit beam shaping,[126,127] crossed-beam shaping,[128] and spatiotemporal beam shaping.[129,130] All of these techniques have proven capabilities for the production of isotropic resolution in the transverse and vertical directions, which allows a circular cross-sectional shape to be achieved. However, each technique does have its advantages and disadvantages in terms of flexibility, ease of operation, and cost.

Figure 25(a) shows a schematic diagram of a focusing system that incorporates the slit beam shaping technique.[126,127] The system employs a narrow slit that can be placed directly in front of the objective lens without using an extra mount. Diffraction induced by the slit enlarges the focal spot in the transverse direction, producing an optical waveguide with a perfectly symmetrical cross section (Fig. 25(b)). In contrast, an optical waveguide fabricated without the slit beam shaping has a highly asymmetric cross section, which obviously cannot support single-mode propagation (Fig. 25(c)). It is important that the slit be oriented parallel to the direction of sample motion in the laser writing process; however, this makes it difficult to fabricate curved optical waveguides or microfluidic channels with complex 3D geometries. The problem can be solved by either dynamic slit beam shaping[131,132] or simultaneous shaping of the femtosecond laser pulses both spatially and temporally.[129,130]

The key to dynamic slit beam shaping technology is to maintain the orientation of the slit parallel to the translational direction of the sample along the curved scanning trajectory; i.e., the slit is always oriented parallel to the waveguide axis. Technically, this can be achieved either by mechanical rotation of a physical slit or by generation of adaptive slit illumination with a spatial light modulator (SLM). Both approaches can allow for the writing of curved optical waveguides with uniform symmetrical cross sections; however, adaptive slit beam shaping based on a SLM can provide several additional advantages, such as real-time change of the slit dimensions and dynamic control of the writing beam pulse energy.[132] Figure 26(a) shows an experimental setup for adaptive slit beam shaping, with an SLM phase pattern (i.e., the grating region) shown as an inset. The adaptive slit, of which the shape is defined by the grating region in the SLM, is mapped onto the objective lens with a 4-f system composed of two achromatic doublet lenses. A pinhole is arranged between the two achromatic lenses to select only the first-order diffraction from the vertical grating in the adaptive slit, whereas the zeroth-order diffraction is blocked. The efficiency of the first-order diffraction of a blazed grating is known to reach its maximum when the phase modulation depth is 2π rad. Dynamic adjustment of the writing beam power can be easily achieved by variation of the grating phase modulation depth. Figure 26(b) presents a differential interference contrast (DIC) image of a circular track
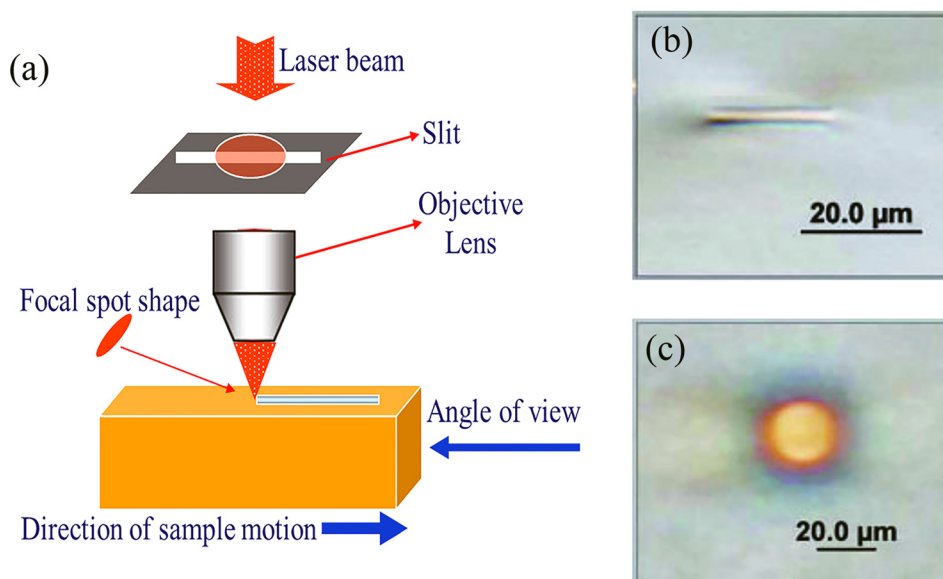

FIG. 25. (a) Schematic illustration of the slit-beam shaping system. Optical waveguides written in glass (b) without and (c) with slit beam shaping. Reproduced with permission from Cheng et al., Opt. Lett. **28**, 55 (2003) and Ams et al., Opt. Express **13**, 5676 (2005). Copyright 2003 and 2005 The Optical Society of America.
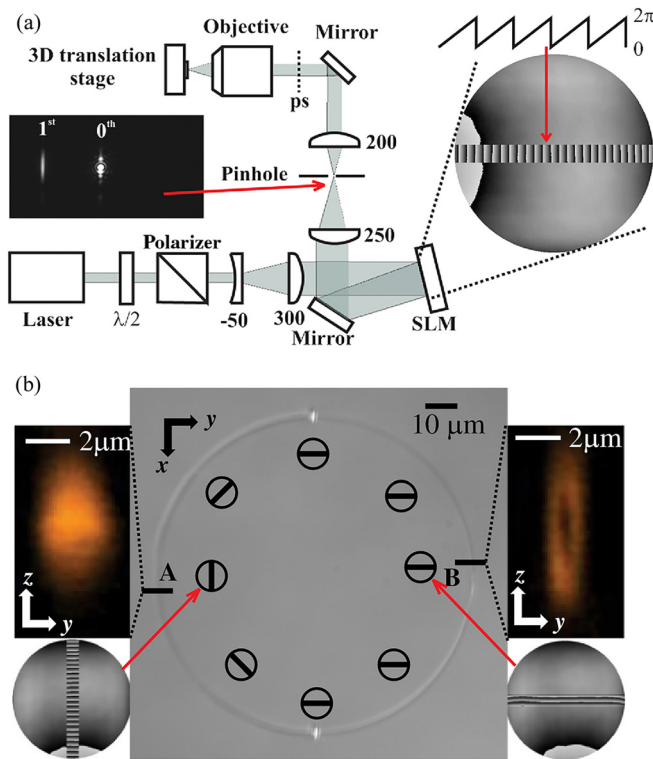
FIG. 26. (a) Experimental setup for adaptive slit beam shaping. The inset shows an example SLM phase pattern. (b) DIC image of a circular structure written with and without variation of the slit orientation during fabrication. The third harmonic images show cross sections of the structure at points A and B. The circular insets indicate the slit orientation at each point. Reproduced with permission from Salter *et al.*, Opt. Lett. **37**, 470 (2012). Copyright 2012 The Optical Society of America.

written in glass. To compare the cross sections obtained with adaptive and fixed slits, the slit orientation was varied only in the sample translational direction during fabrication of the left-hand side of the circle. A uniform circular cross section was achieved at the left-hand side, whereas at point B on the right-hand side, the cross section is strongly elliptical because the slit is perpendicular to the translation direction. In addition to correction of the cross-sectional ellipticity, the adaptive optics also enable correction of the aberration induced by the mismatch between the refractive indices of the transparent material and the immersion medium.[133]

It is noteworthy that in both the slit and dynamic slit beam shaping schemes, balanced transverse and vertical resolutions have only been achieved in the 2D plane perpendicular to the translational direction of the sample. In principle, for 3D internal processing of transparent materials, a 3D isotropic resolution will be the ultimate goal. 3D isotropic resolution can be obtained using a crossed-beam shaping technique, in which the focusing system consists of two orthogonal objective lenses that are positioned so that they have a common focal point.[128] If two femtosecond laser pulses traveling through two lenses temporally overlap at the common focal point, then the synthesized focal spot will produce an isotropic illumination volume near the crossing point. The major difficulty with this technique is to maintain the spatial and temporal overlap of the 2 fs laser beams focused by the orthogonal objective lenses during the

fabrication process. To overcome this issue, the glass sample is translated in a fixed glass cell that contains a liquid medium with a matching refractive index to maintain the optical paths of the two orthogonal beams. Thus, the two initially aligned foci can maintain spatiotemporal overlap during the entire fabrication process. This technique successfully addresses the problems, but requires a complex system.

Recently, He *et al.* developed a more sophisticated technique that allows 3D isotropic resolution to be achieved with only a single objective lens. In the spatiotemporal focusing scheme, the incident pulses must be first spatially dispersed by a pair of parallel gratings before entering the focusing lens, as schematically illustrated in Fig. 27(a).[129] Temporal focusing is achieved because different frequency components spatially overlap only near the focus, so that the pulse width is minimized and the peak intensity is maximized at the focus. This improves the axial resolution for femtosecond laser microfabrication because the peak intensity decreases rapidly due to broadening of the pulse width when the pulse is moving away from the geometric focal spot. Figure 27(b) demonstrates that it is possible to fabricate microfluidic channels with circular cross sections, regardless of the translational direction. However, the technique has not been used for the fabrication of optical waveguides, because there pulse front tilting occurs in the spatiotemporally focused femtosecond laser pulses.[134] The tilted pulse front can induce a "quill" writing effect, which gives rise to subtle changes in the morphology of tracks written by femtosecond laser pulses when the translational direction of the sample switches.[101] At first sight, the quill writing effect appears counterintuitive; however, it clearly indicates that the microscopic morphology of the internally written structures is

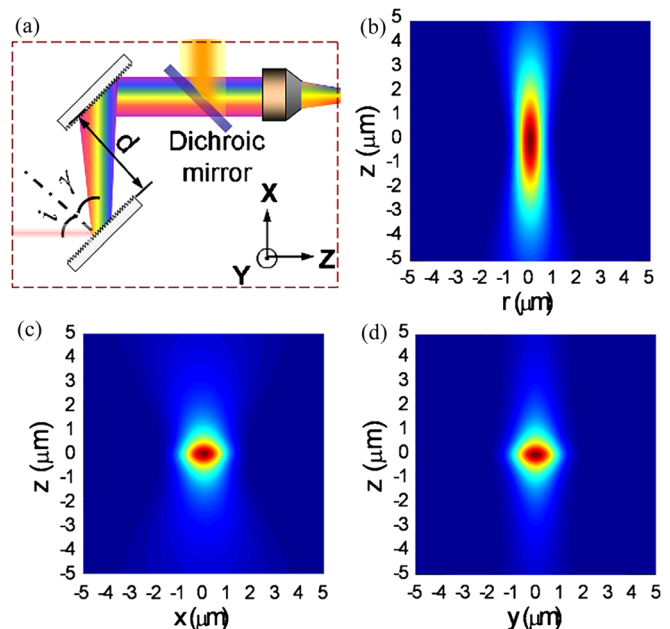FIG. 27. (a) Experimental setup for spatiotemporal focusing of a femtosecond laser beam. (b) Numerically calculated laser intensity distributions at the focus produced by an objective lens without (left panel) and with temporal focusing in the XZ (middle panel) and YZ (right panel) planes, respectively. Reproduced with permission from He *et al.*, Opt. Lett. **35**, 1106 (2010). Copyright 2010 The Optical Society of America.

critically dependent on the plasma dynamics controlled by the femtosecond laser pulses, as discussed in Sec. IV C.

Last but not least, we would like to point out that in addition to producing spherical focal spots of isotropic peak intensity distributions, spatiotemporal focusing can also be used to avoid the nonlinear self-focusing effect before the arrival of pulses near the focus spot and promote the throughput of 3D internal processing.[130,135,136] In particular, a latest investigation reveals that a spatiotemporally focused pulse possesses not only a pulse front tilt, but also an intensity plane tilt around the focus.[137]

C. Quill and nonreciprocal effects

The pulse front tilt, as illustrated in Fig. 28(a), is caused by the tilted intensity distribution in the front of a femtosecond pulse, so that the pulse front is no longer perpendicular to the propagation direction of the laser pulses. A pulse front tilt is typically generated either by angular or spatial chirping of the incident pulses. An immediate consequence of a pulse front tilt in femtosecond laser internal processing is a nonreciprocal writing effect, which can directly influence many applications such as waveguide writing, optical storage, and tissue surgery. The effect was first reported by Kazansky et al. in 2007 and was termed quill writing because of its similarity to the effect of hand writing with a quill pen.[101] An equivalent terminology for quill writing is nonreciprocal writing and these two terms are interchangeable.

As a manifestation of the quill writing effect, straight lines have been written in glass with opposite translation directions with respect to the direction of the pulse front tilt, as shown in Fig. 28(b).[138] In this specific case, a 800 nm femtosecond laser emits pulses with a duration of ca. 150 fs

at a repetition rate of 250 kHz to write the lines at a scan speed of 50 μm/s and to a depth of 120 μm within the sample. With crossed polarizers, birefringent modification can only be smoothly induced in lines written with the sample being translated from the left to the right (i.e., writing from the right to the left, as indicated by the arrows in Fig. 28(b), whereas the lines written with the opposite translational direction show no birefringence. The role of the pulse front tilt that underlies the quill writing effect is further evidenced by the results presented in Fig. 28(c). The effect in Fig. 28(b) can be perfectly reversed by adding a mirror into the setup to reverse the direction of the pulse front tilt while all the other experimental conditions remain unchanged.

Recently, several groups have reported that the quill writing effect can also be induced by femtosecond laser pulses without any front tilt, but with an inhomogeneous intensity distribution across the beam.[139] Although the underlying mechanism of quill writing has not been clarified, this finding suggests that symmetry breaking in the plasma dynamics is responsible for the nonreciprocal behavior. Kazansky and Beresna provided a tentative model to qualitatively explain their experimental observations.[138] Either pulse front tilt or spatial inhomogeneity in a femtosecond laser beam will lead to an asymmetric ponderomotive force acting on the free electrons in the focal volume, as a result of which the electrons are driven to one side of the focal area. Direct evidence for the asymmetric distribution of electrons produced by front-tilted femtosecond laser pulses has been recently reported, by the observation of second harmonic generation in centrosymmetric gases such as air and argon.[135] Under suitable irradiation conditions, the asymmetry of the electron distribution can encode its signature in the
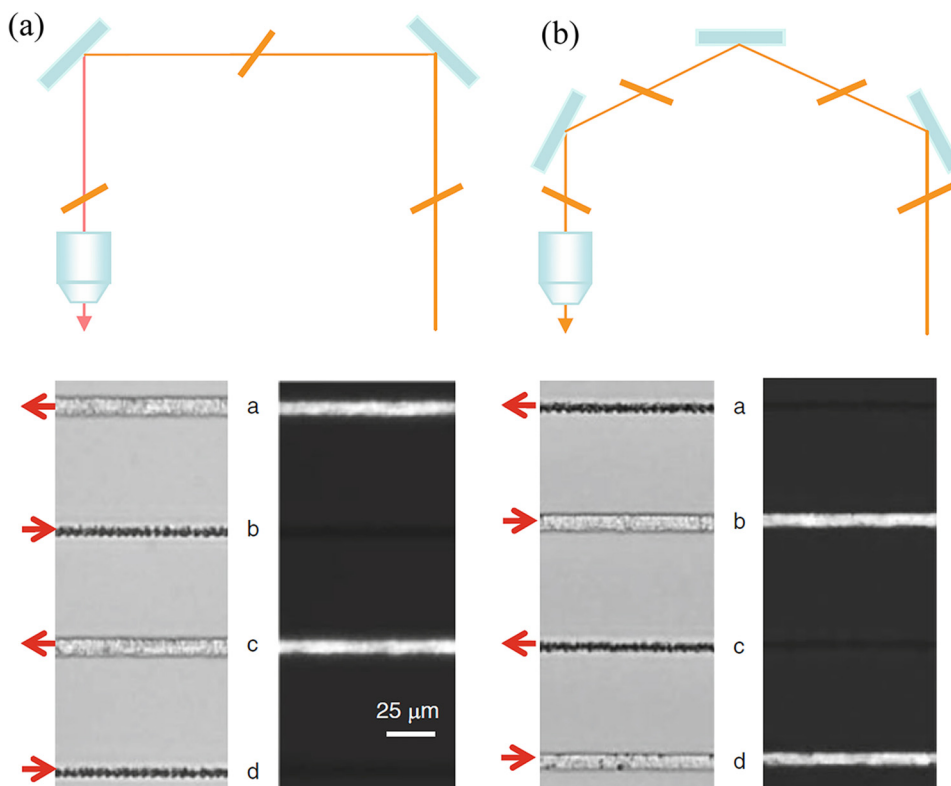

FIG. 28. Quill effect lines written in opposite directions have different morphology. In crossed polarizers, birefringent modification is induced only in one direction. The effect can be reversed by reversing the tilt direction by reflecting the beam from a mirror. Reproduced with permission from Appl. Phys. Lett. **90**, 151 120 (2007). Copyright 2007 AIP Publishing LLC.

structural changes of the laser modified zone and affect the interaction of subsequent pulses with the material in a manner that is critically dependent on the direction of sample translation. The quill writing effect provides an additional control parameter for investigation of the physics behind the interaction of femtosecond laser pulses with various transparent media.[102,140] However, from an application perspective, the quill writing effect is undesirable for writing photonic circuits of complex 3D configurations because it inevitably leads to inhomogeneity in waveguides with different orientations. Therefore, to minimize the quill writing effect, care must be taken to remove both the pulse front tilt and spatial inhomogeneity in the femtosecond laser beam.

D. Fabrication of photonic devices

The field of photonic device fabrication by femtosecond laser internal processing was pioneered in 1996 by Davis *et al.*[18] and Glezer *et al.*[19] through the demonstration of optical waveguide writing and the formation of a nanovoid array inside glass, respectively. These experiments have had a significant impact since then. In particular, optical waveguides are the building blocks for many photonic devices, such as beam splitters and couplers,[141–145] volume Bragg gratings,[146,147] diffractive lenses,[148] Bragg grating waveguides,[149] Mach-Zehnder interferometers (MZIs),[150] waveguide lasers,[151,152] and nonlinear optical waveguide devices.[153,154] On the other hand, the formation of an arbitrary 3D distribution of nanovoids inside glass allows for high-density recording of digital bits. A combination of various internal processing methods opens up new avenues for the fabrication of a variety of integrated microdevices for applications such as integrated photonics (e.g., quantum chips, photonic lanterns, optical information processors, and optical modulators), optofluidics (e.g., optofluidic lasers, chemical and biosensors, medical and biochips, and adaptive and tunable optics), and optomechanics (e.g., microdisplacement sensors). Several review articles are already available on the writing of passive and active waveguide devices in glass, crystals, and ceramics.[12,15,17,155] Therefore, here we mainly focus on emerging applications that have been enabled by the formation of novel 3D photonic structures by femtosecond laser internal processing.

Recently, long-term (i.e., more than 1000 yr) data storage enabled by holographic femtosecond laser processing has attracted significant attention. Current data storage techniques based on hard disk and optical disk drives can only support a lifetime of tens of years, and are vulnerable to harsh environmental conditions such as high/low temperatures or humidity. Recording digital bits in fused silica with femtosecond laser induced multiphoton absorption has been recognized as a potential solution, because fused silica is a material with excellent thermal and chemical stability.[156–159] In addition, the 3D capability of this approach holds the promise of achieving ultrahigh-density data storage.

In a recent experiment, Shiozawa *et al.* reported on the simultaneous recording of multiple bits in fused silica using an 800 nm, 120 fs laser operating at 1 kHz.[156] To achieve single-shot recording of multiple microvoids organized into predesigned patterns that are distributed in a 2D plane at a certain depth in the glass sample, a SLM was used to modulate the phase of the femtosecond laser beam according to computer-generated holograms, as displayed in Fig. 29. After being focused by lens 1 in Fig. 29(a), the zeroth order of the modulated femtosecond laser beam was blocked by a metal plate. The femtosecond laser beam was then collimated by lens 2 and focused in the fused silica with an objective lens (NA = 0.8). In the experiment, approximately 100 dots could be simultaneously recorded at a certain depth with a single-shot laser pulse. By shifting the glass sample in the vertical direction, four-layer data storage with an interlayer distance of 60 μm was demonstrated, as shown in Fig. 29(b). The interlayer distance was optimized as a trade-off between the data recording density and the crosstalk between the successive layers. In the experiment, the crosstalk was examined by experimentally measuring the signal-to-noise ratio (SNR), which was higher than 15 dB (i.e., the SNR limit of crosstalk required for data storage). At a dot pitch of 2.8 μm, the recording density in four layers reaches 45 Mbyte/in.[2], which is already greater than that of a compact disc. Moreover, readout of the multilayer data recorded at different depths was demonstrated using a driveless system equipped with a low-magnification optical microscope, although signal processing was necessary to sharpen the microscope image of the recorded dots and suppress the bit-error rate (BER). Remarkably, a BER in the order of 10^{-3} was demonstrated using the simple readout system.[157]
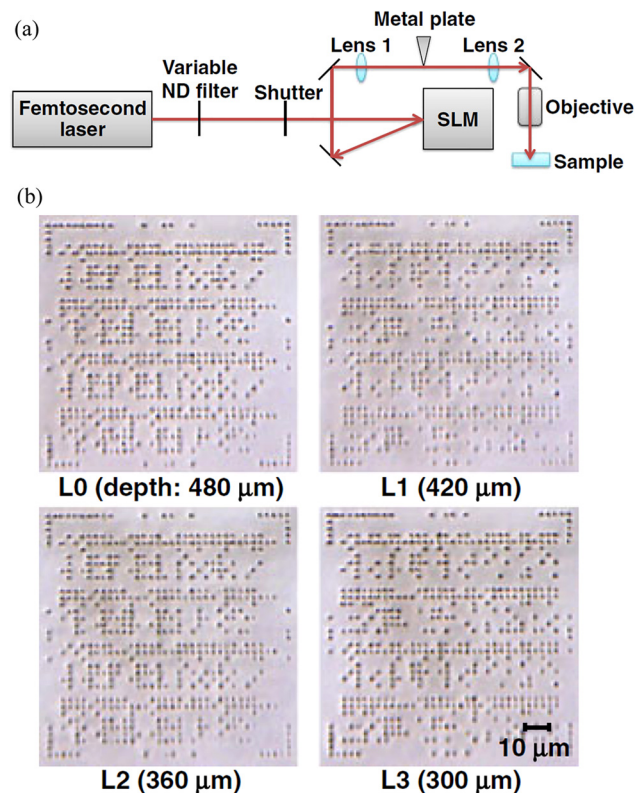

FIG. 29. (a) Experimental setup for simultaneous multi-bit recording. (b) Optical micrographs of recording patterns at different depths of a four-layer sample. Reproduced with permission from Shiozawa *et al.*, Jpn. J. Appl. Phys. **52**, 09LA01 (2013). Copyright 2013 The Japan Society of Applied Physics.

Further increase of the recording density in fused silica can be achieved by the formation of complex nanostructures in the recorded dots, which provides additional dimensions for data storage. Zhang *et al.* recently demonstrated a 5D data storage technique that utilizes self-assembled nanograting structures confined in the focal area of a femtosecond laser as the digital bits.[159] The nanograting can induce birefringence, where the axial orientation and strength of retardance are used as the fourth and fifth dimensions, in addition to the XYZ dimensions in space, for data storage. In the ideal case, a 5D optical storage would enable a capacity up to 18 GB in a fused silica substrate of the same size as that of a conventional compact disc. An accelerated aging experiment conducted under a high temperature environment implied that the lifetime of the nanograting structures, which are used as the digital bits, is even longer than the age of the Universe. Even if the uncertainties involved in the extrapolation over such a long period were considered, the lifetime of optical storage in fused silica is seemingly unlimited.

Similar to microdots, optical waveguides are also a basic element for photonic applications. Over the past decade, optical waveguide writing with femtosecond lasers has been intensively investigated because of its potential for the construction of miniaturized photonic systems, such as optofluidic chips, waveguide sensors, waveguide lasers, and astrophotonic devices. In particular, 3D waveguide writing has recently emerged as a powerful tool for the construction of compact quantum circuits.[30,31,160] Conventional optical interferometers for quantum information processing are built on optical tables with bulk optics. The constructed system generally suffers from a large footprint size, which causes poor stability and scalability. For future applications outside the laboratory, integrated photonic quantum chips based on optical waveguides will be an ideal solution. Although these waveguides can be fabricated on semiconductor chips using planar lithographic technology, they are inherently restricted to a 2D plane and typically have a rectangular cross section. The waveguides are thus sensitive to polarization of the light. In contrast, a femtosecond laser can be used to write optical waveguides with almost unlimited 3D configurations and controllable cross-sectional shapes in transparent materials, which can enable evanescent coupling among multiple waveguides (>2) and polarization-insensitive guiding of light. Waveguides written with a femtosecond laser are ideal candidates for quantum information processing applications. Currently, several functional quantum photonic circuits have been built in glass chips, on which quantum information processing[31,161] and the simulation of quantum systems[162] have been successfully demonstrated.

Figure 30(a) illustrates the layout of a photonic quantum chip that consists of an interferometric array to simulate an eight-step 1D quantum walk (QW).[161] Colored boxes represent phase shifters and different colors indicate different phase shifts, which are realized by the introduction of a controlled deformation in one of the optical waveguides at the output of the directional coupler, as shown in Figs. 30(b) and 30(d). The 3D optical network is composed of almost 60
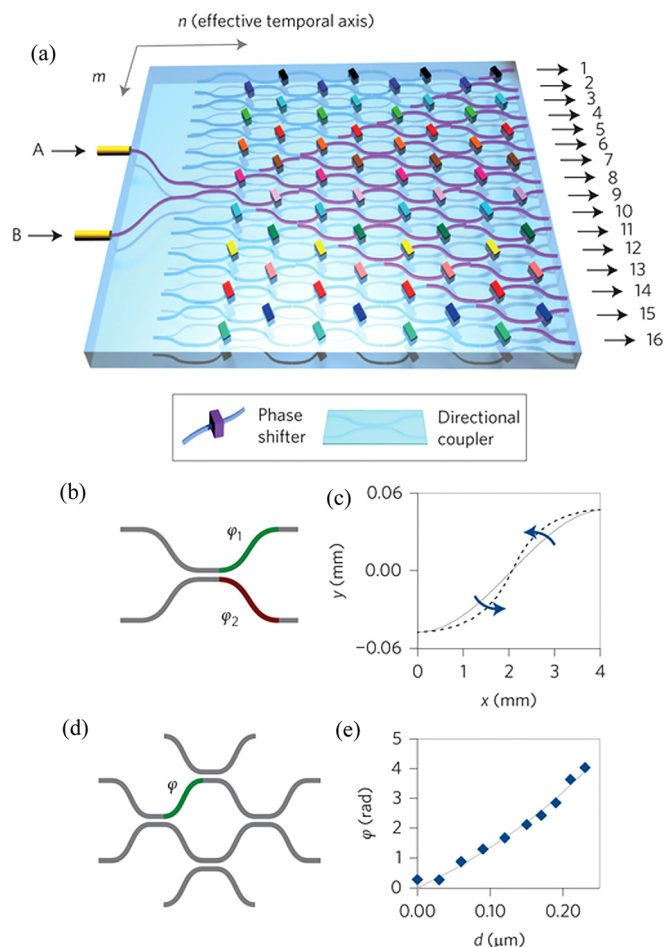

FIG. 30. Integrated circuit for disordered QW. (a) Scheme of the network of directional couplers implementing an eight-step 1D QW with static disorder. Different colors indicate different phase shifts and violet waveguides represent the accessible paths for photons injected from inputs A and B. (b) Controlled deformation of either of the two S-bent waveguides at the output of each directional coupler extends the optical path and is equivalent to the application of a phase shifter. (c) The deformation is given by a nonlinear coordinate transformation. The graph shows the undeformed (solid line) and the deformed S-bends (dashed line). (d) Schematic of the Mach–Zehnder structure, representing the unit cell of the directional couplers network, fabricated to calibrate the phase shift induced by the deformation. (e) Phase shift induced by the deformation; theoretical curve calculated from the nominal geometric deformation (solid line), and experimental measurements (diamond symbols). Reproduced with permission from Crespi *et al.*, Nat. Photonics **7**, 322 (2013). Copyright 2013 Nature Publishing Group.

cascaded beam splitters. Building such a complex interferometer with bulk optics is extremely difficult because of the stringent requirements on alignment precision and phase stability. Crespi *et al.* demonstrated Anderson localization (i.e., trapping of scattered fields in a disordered material) using this chip with two entangled particles affected by static disorder. It is expected that such complex interferometric systems will benefit quantum computation, quantum communication, and high-precision measurements.

E. Fabrication of biochips

3D microfluidic components embedded in transparent materials can be directly formed by femtosecond laser internal processing without any stacking and bonding procedures,

which has enabled the one-step fabrication of integrated microfluidic systems for a wide range of biochip applications. Furthermore, in combination with waveguide writing, optical diagnostics have been directly incorporated into a microfluidic chip. Over the past decade, an impressive number of highly integrated optofluidic systems have been designed and fabricated, for which a variety of innovative functionalities for biological and chemical applications (e.g., determining the functions of living microorganisms, sensing the concentrations of liquid samples, detecting, sorting and manipulating single cells, rapid screening of algae populations, and observation of microorganisms in nanoaquaria) have been successfully demonstrated.[32,33,35–39]

Figure 31 shows a microfluidic network fabricated in commercially available silica glass by water-assisted 3D femtosecond laser drilling.[119] An 800 nm, 120 fs femtosecond laser operating at 1 kHz was used to induce optical breakdown from the backside of the glass sample which was in contact with distilled water. A 20× objective lens (NA = 0.45) was used to focus the laser beam into the glass. A hollow microchannel was drilled by translation of the sample at a speed of 160 μm/s along the designated 3D trajectory. To extend the length of the microfluidic channel, the authors connected the opening of the microchannel with a rubber hose through which positive and negative pressures were alternately applied to accelerate the removal of debris generated in the microfluidic channel during ablation. The total length of the fabricated microchannel reached 2.1 cm, which is an increase of almost one order of magnitude compared with previous results obtained using a similar approach.[163] The two-layer microchannel network shown in Fig. 31 provides clear evidence of the extreme flexibility of this technique.

3D microfluidic chips fabricated by femtosecond laser internal processing have been used for a large number of biological and chemical applications. Facilitated by the wide range of the dimensions available for microfluidic channels (i.e., from a few tens of nanometers to the millimeter scale), microfluidic biochips have been employed to investigate and manipulate single living biological objects ranging from millimeter-scale microorganisms and micrometer-scale cells to nanometer-scale biomolecules.

Figures 32(a) and 32(b) show a typical biochip consisting of 3D microfluidic channels with relatively large cross sections.[164] Hanada *et al.* termed this biochip as a nanoaquarium, which was produced to observe the rapid motion of flagella in microorganisms such as *Euglena gracilis*. The nanoaquarium is composed of a 1-mm-long channel with a cross-sectional area of $150 \times 150 \, \mu m^2$ embedded 150 μm beneath the glass surface, and two open reservoirs with dimensions of $500 \times 500 \, \mu m^2$ connected to both ends of the channel for the introduction of *Euglena gracilis* in water. The nanoaquarium was fabricated in Foturan glass by femtosecond laser direct writing followed by annealing and wet chemical etching. The vertical microchannels are particularly useful because the front and rear sides of *Euglena gracilis* can be observed when it is moving upward and downward, respectively. In contrast, only horizontal motion of *Euglena gracilis* can be observed with conventional Petri dishes under an optical microscope. The etched surfaces of the inner wall typically have a roughness of the order of a few tens of nanometers, which causes scattering of light and distortion of the wavefront; therefore, the fabricated sample is annealed at a temperature of 570 °C to smooth the inner wall of the microchannel by surface reflow. The cross-sectional shape and depth of the horizontal microchannel were also carefully selected to be rectangular and close to the thickness of a cover glass, respectively, to eliminate spherical aberration caused by the mismatch between the refractive indices of air and glass at the interface. Figure 32(d) shows a series of microscope images of *Euglena gracilis* swimming in the microchannel. Such dynamic observation is impossible using a conventional Petri dish that only allows 2D observation. In addition, it is difficult to efficiently capture images of living microorganisms in a Petri dish because they can quickly escape from the field of view of the microscope. Due to the flexibility of femtosecond laser direct writing, a variety of nanoaquaria with different geometries and functionalities have been fabricated for the demonstration of various applications, including determining the information transmission process in *Pleurosira laevis*, observing the high-speed motion of *Cryptomonas*, and elucidating the mechanism for *Phormidium* gliding to seedling roots for the promotion of Komatsuna (Japanese mustard spinach) growth.[165]

Figure 33 presents another biochip fabricated in fused silica by femtosecond laser direct writing and followed by immediate chemical wet etching.[37] In comparison with the microfluidic structures fabricated in Foturan glass, microfluidic structures fabricated in fused silica can provide finer
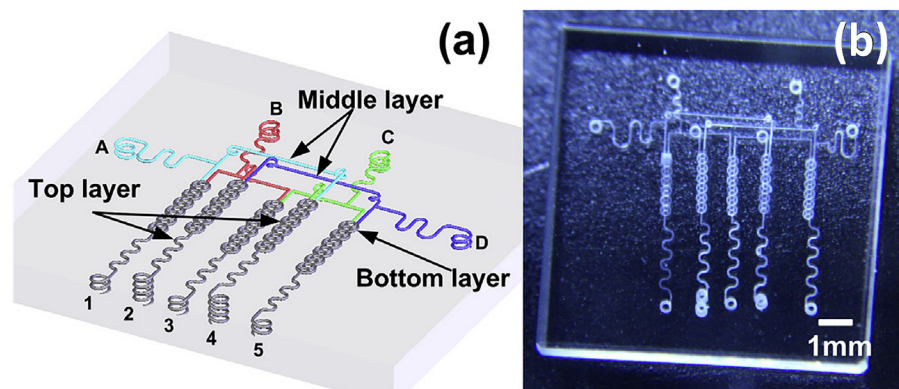

FIG. 31. (a) Design of a microfluidic chip composed of a complex 3D microfluidic network. (b) Microfluidic chip fabricated by water-assisted femtosecond laser 3D drilling. Reproduced with permission from Y. Li and S. Qu, Curr. Appl. Phys. **13**, 1292 (2013). Copyright 2013 Elsevier.
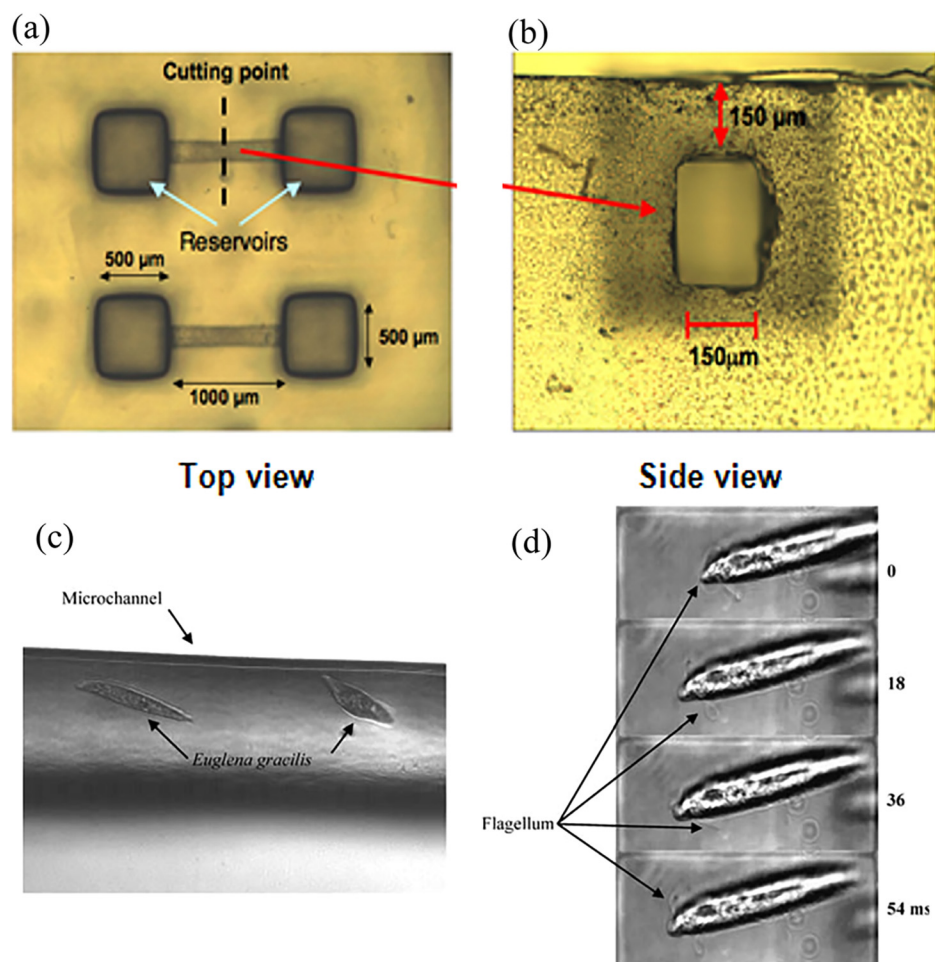
FIG. 32. (a) Top- and (b) side-views of a nanoaquarium fabricated to observe the motion of *Euglena gracilis*. (c) and (d) Micrographs of *Euglena gracilis* swimming in a microchannel. Reproduced with permission from Hanada *et al.* Biomed. Microdevices **10**, 403 (2008). Copyright 2008 Springer.

feature sizes (i.e., microchannels with smaller diameters); however, it also suffers from inferior fabrication efficiency. The biochip in Fig. 33 is used as a 3D mammalian cell separator, which is composed of a T-junction formed by two orthogonally arranged microfluidic channels with a cross-sectional area of $1\,mm \times 300\,\mu m$. The T-junction provides one inlet and two outlets. At the junction, the two microchannels are connected by an array of narrow 200-μm-long microchannels with a cross-sectional area of $4 \times 8\,\mu m^2$. The microchannel array serves as a cell sorting unit (Fig. 33(b)). The sorting microchannels in the array, which are referred to here as constrictions, were designed to have a diameter slightly less than the average size of the cells; therefore, cell sorting is achieved by applying a gradient pressure across the constrictions, which allows only cells that have deformability (i.e., higher elasticity) to navigate their way through the constrictions. The sorted cells are then collected at outlet 1, while the more rigid cells are collected at outlet 2. Promyelocytic HL60 cells with diameters of ca. 12 μm were used as model cells, for which the fabricated device exhibited a sorting throughput as high as 2800 cells/min at a flow rate of 167 μl/min. Fluorescence-based cell viability analysis shows that 81% of the cells collected after the sorting unit maintain cellular integrity. One likely cause of cell death may be the relatively high surface roughness on the inner walls of the constrictions. It should be noted that for most of microfluidic applications related to living cells, control of

the microchannel inner wall roughness is critical. However, this issue has not yet been completely resolved for microchannels fabricated by femtosecond laser processing.

Recently, femtosecond laser internal processing has allowed the fabrication of biochips integrated with both micro- and nanofluidic channels for the analysis of single DNA molecules.[123] The biochip was fabricated by ablation of porous glass immersed in water with femtosecond laser irradiation, as discussed in Sec. IV A. Figure 34(a) shows a schematic illustration of an integrated micro-nanofluidic structure that contains an array of two-layer nanochannels connected to two microfluidic channels. Figure 34(b) shows a top-view optical micrograph of the fabricated nanochannel arrays. The nanochannels were directly written at depths of ca. 200 μm below the porous glass surface, and the difference in the depths of the two layers of the nanochannels was only ca. 1.5 μm. All the nanochannels were directly written by a single scan at a translation speed of 10 μm/s with a pulse energy of 128 nJ. The direction of laser polarization was perpendicular to the translational direction. The fabricated nanochannels have a total length of ca. 40 μm with a width of ca. 40 nm and a height of 1.5 μm (Figs. 34(b)–34(d)). To demonstrate the applications of such nanochannels for the investigation of single molecule behavior, a DNA stretching experiment was conducted using the fabricated device. Figures 34(e) and 34(f) show typical images of stretching of λ DNA in nanochannels with widths of 40 and 200 nm,
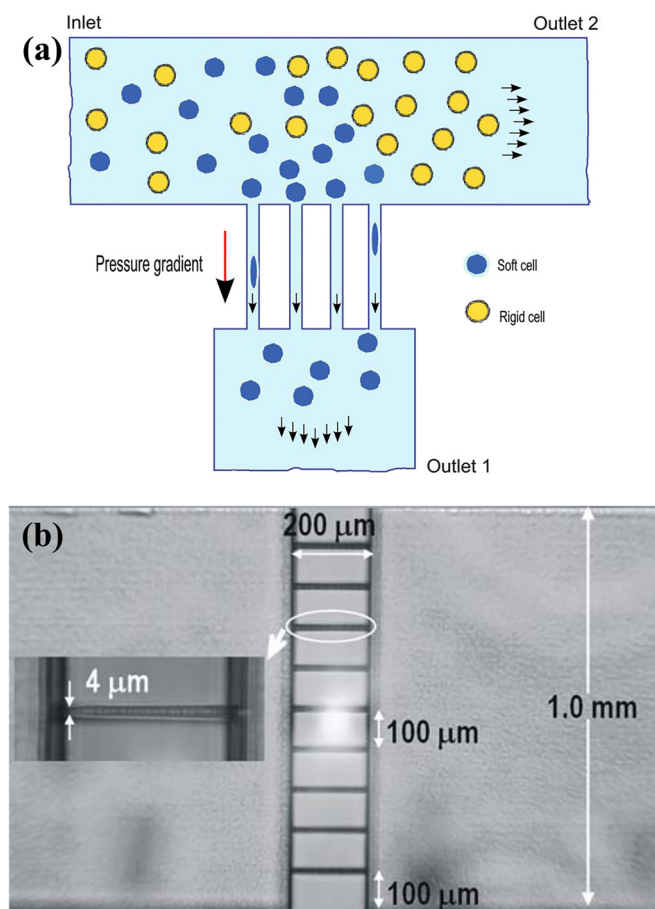
FIG. 33. (a) Schematic illustration of a 3D mammalian cell separator. (b) Top-view micrograph of the constriction array. Reproduced with permission from Choudhury *et al.*, Lab Chip **12**, 948 (2012). Copyright 2012 The Royal Society of Chemistry.

respectively. The average stretching lengths of the DNA molecules are ca. $6.4 \pm 1.0 \, \mu m$ (ca. 30% of the dye-adjusted contour length) and ca. $2.8 \pm 0.6 \, \mu m$ (ca. 13% of the dye-adjusted contour length) in Figs. 34(e) and 34(f), respectively. The continuous flow and uniform stretching of the DNA molecules in the nanochannel arrays also confirms the continuity of the nanochannels and the repeatability of the direct writing process.

Although biochip fabrication based on internal processing in glass with femtosecond laser pulses has achieved such successes, one significant drawback is its relatively lower fabrication resolution compared with that of TPP. To overcome this difficulty, Wu *et al.* proposed a new method termed hybrid femtosecond laser microfabrication (HFLM).[166] The technique involves successive subtractive (femtosecond laser-assisted wet etching of glass) and additive (TPP) 3D microprocessing to realize 3D ship-in-a-bottle microchips, enabling fabrication of novel biochips by the integration of various 3D polymer micro/nanostructures into flexible 3D glass microfluidic channels. Figure 35(a) shows a schematic diagram of the HFLM concept, which mainly consists of femtosecond laser scanning in Foturan glass followed by annealing, HF etching, a second anneal to smooth the inner surfaces, polymer filling, TPP and development. The novel technique has been used to fabricate microfluidic

systems integrated with micro/nanofilters and micromixers. As one example, a micromixer, which is conceptually illustrated in Fig. 35(b) and shown in the SEM image in Fig. 35(c), was integrated into a Y-shaped microfluidic channel embedded in a glass substrate. A comparison of Figs. 35(d) and 35(e) clearly shows that mixing of two different fluids cannot be achieved in the microfluidic channel without the micromixer; whereas a mixing efficiency as high as 87% can be realized with the micromixer.

The unique ability to simultaneously form fluidic and optical microcomponents in glass with extreme flexibility in terms of 3D processing makes femtosecond laser direct writing an ideal tool for the fabrication of integrated optofluidic devices. Optofluidic devices can be realized by incorporating either optical waveguides or free-space micro-optical components in microfluidic systems.[33,35,36,103,167–170] Waveguides, free-space micro-optical components (i.e., microlenses or micromirrors), and microfluidic channels can all be written in glass substrates in a single-step continuous process, which eliminates the need for assembling or packaging procedures.

As a typical example, the refractive index sensor illustrated in Fig. 36(a) clearly showcases the distinct advantages by demonstrating the out-of-plane integration of a waveguide-based MZI and a microfluidic channel.[33] In this specific case, the MZI was intentionally inscribed in a plane tilted at 7° to the substrate plane. In such an arrangement, the two arms of the MZI are located at different depths below the surface, which ensures that only the sensing arm and the microchannel intersect at the right angle, whereas the reference arm passes $20 \, \mu m$ over the microchannel [Figs. 36(b) and 36(c)]. Due to the unbalanced optical lengths of the two arms, the transmission spectrum of the MZI has interference fringes at the wavelength when a sufficiently wide spectral region is scanned by a tunable laser, as shown in the inset of in Fig. 36(d). When the refractive index of the sample in the microfluidic channel varies slightly with the analyte concentration, the variation can be detected by a shift in the fringes. The sensitivity of the device was determined to be 10^{-4} refractive index units (RIU) using D-glucose solutions of various concentrations as test samples, which corresponds to a detection limit of 4 mM [Fig. 36(d)]. The sensitivity was determined to be limited by temperature fluctuations of the analyte in the microfluidic channel; however, the intrinsic sensitivity, measured with an empty channel, is one order of magnitude better. The device offers a high spatial resolution for refractive index sensing comparable to the diameter of the waveguide mode (ca. $11 \, \mu m$). In contrast, conventional MZI refractive index sensors, which detect the evanescent field of the waveguide mode penetrating into a probe analyte, typically require interaction lengths ranging from a few millimeters to several centimeters to achieve sufficient sensitivity.[171]

V. GLASS BONDING

A. Principle and features of glass bonding

Glass microbonding has attracted much interest recently due to its potential applications in electronics, optics,
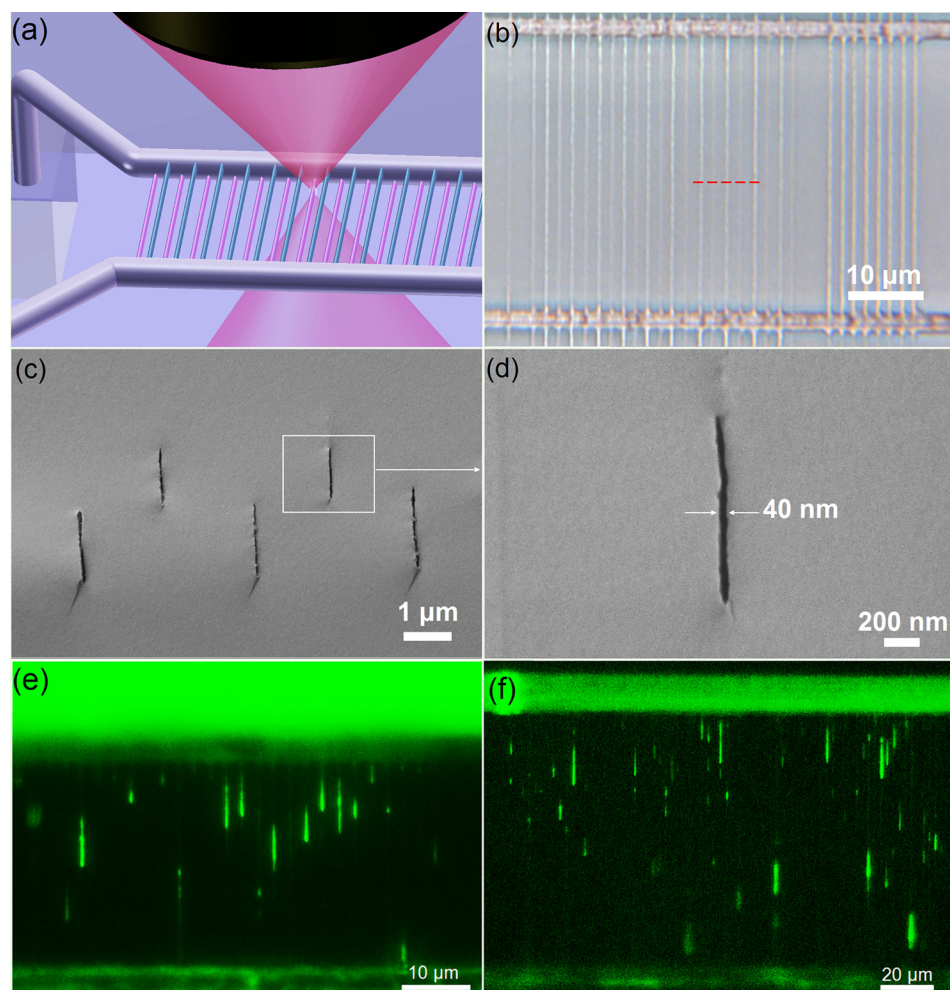
FIG. 34. (a) Schematic diagram of an array of double-layer nanochannels that bridge two microchannels. (b) Top-view optical micrograph of double-layer nanochannels after post-annealing; (c) Cross-sectional SEM micrograph of the nanochannels cleaved along the red dashed line in (b). (d) Close-up cross-sectional SEM micrograph of a nanochannel. (e) and (f) Fluorescent images that show the stretching of λ DNA in two arrays of nanochannels with widths of (e) 50 nm and (f) 200 nm. Reproduced with permission from Liao et al., Lab Chip 13, 1626 (2013). Copyright 2013 The Royal Society of Chemistry.

MEMS, medical devices, microfluidic devices, and small satellites. Laser welding is a promising technique for bonding glass substrates because it has many advantages over conventional bonding techniques such as anodic bonding, fusion bonding, and hydrofluoric acid bonding. Laser welding can provide rapid, high-precision, high-quality, flexible welding that results in low heat distortion. For glass bonding, the laser beam should be absorbed at the interface of the stacked glass substrates. Therefore, CO_2 lasers, which are conventionally used for welding, cannot be used for glass bonding, due to strong absorption by the glass, which prevents propagation to the interface. However, other lasers such as Nd:YAG laser, fiber lasers, and laser diodes require the insertion of an intermediate absorber layer between the two glass substrates because they have little absorption in glass. In contrast, light from femtosecond lasers can induce strong absorption only at the interface due to multiphoton absorption.[172,173]

Glass bonding based on fusion welding with a femtosecond laser is considered to occur due to melting induced at the interface between two glass substrates by irradiation with a focused laser beam. Figure 37 shows schematic diagrams of the electron excitation and relaxation processes in glass induced by femtosecond laser irradiation.[174] (a) Electrons are first excited from the valence band to the conduction band by multiphoton absorption of the femtosecond laser light

(multiphoton ionization) or tunneling ionization when the laser electromagnetic field is extremely strong. (b) The excited electrons can absorb several laser photons sequentially and move themselves to higher energy states where free carrier absorption is efficient (electron heating). (c) Otherwise, the excited electrons are accelerated by the intense electric field of the femtosecond laser beam and collide with surrounding atoms, which generates secondary electrons (impact ionization). This process is repeated and multiplies the number of free electrons, which results in avalanche ionization. (d) Some of free electrons relax in electron-hole pairs to localize the energy stored, which creates localized states such as self-trapped excitons (STEs). This relaxation often starts one to tens of picoseconds after the laser irradiation, depending on the type of glass. Finally, STEs relax to form permanent defects within a few hundred picoseconds. Some of the other free electrons translate their energy into lattice vibrations that generate heat and then relax to the ground state. Glass heating occurs a few tens of picoseconds after the laser irradiation and the irradiated area returns to room temperature after several tens of milliseconds. This glass heating induces glass melting.[49,50] When the femtosecond laser beam is focused with a moderate pulse energy at the interface of stacked glass substrates, localized melting and rapid resolidification can be induced only near the interface due to this heating, which results in glass bonding.
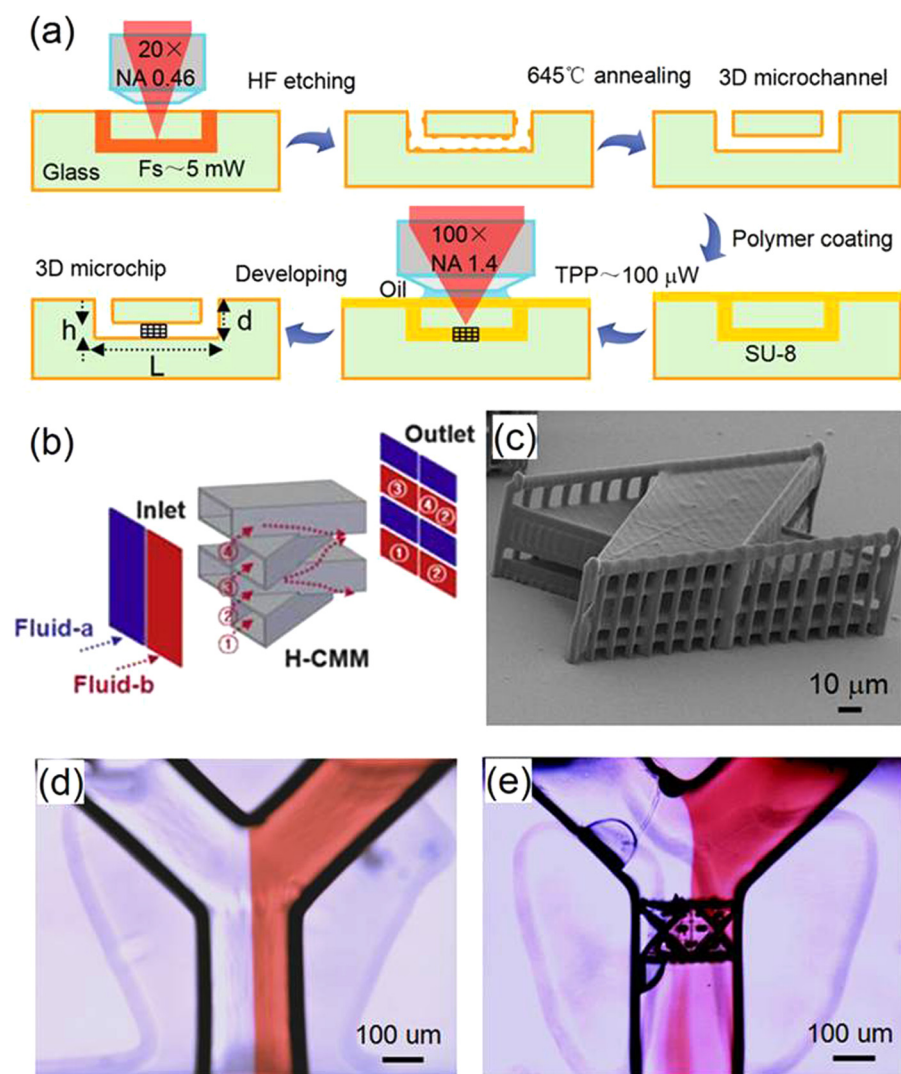
FIG. 35. (a) Schematic illustration of the fabrication procedure for a 3D ship-in-a-bottle biochip by hybrid femtosecond laser microprocessing. The procedure involves femtosecond laser scanning followed by a 1st annealing, HF etching, a 2nd annealing, polymer filling, TPP and development. (b) Schematic design principle of a novel multifunctional filter-mixer device, in which two filters are formed at the inlet and outlet of a passive-type mixer. (c) SEM micrograph showing the 2 filters and 4 layer-microstructure of the mixer. (d) and (e) Comparison of mixing efficiency in microchannels integrated (d) without and (e) with the filter-mixer device. Reproduced with permission from Wu *et al.*, Laser Photonics Rev. **3**, 458 (2014). Copyright 2014 Wiley.

B. Bonding of various glasses

The first experiment on glass bonding using a femtosecond laser was performed in 2005, in which an 800 nm, 130 fs laser at a repetition rate of 1 kHz was used to weld two fused silica substrates.[175] Elimination of the air gap between the two glass substrates is essential in order to achieve successful glass welding;[175,176] therefore, the substrates were stacked after cleaning [Fig. 38(a)] and then pressed together using a fixture with a lens and three bolts [Fig. 38(b)]. The femtosecond laser beam was then focused at the interface to perform welding [Fig. 38(c)].

Since then, both femtosecond lasers and picosecond lasers have been extensively used to bond both the same type of glass substrates, including fused silica,[14,175,177–181] borosilicate glass,[13,177,182–186] soda-lime glass,[187] non-alkali aluminosilicate glass,[176] and photosensitive Foturan glass.[40,188–190] Dissimilar glass substrates such as fused silica/borosilicate glass,[41,179,181,191,192] optical fiber/glass slide,[193] spherical glass bead/float glass,[194] and some other glasses[195,196] have also been fused using the same technique. Table I summarizes some typical examples of ultrafast laser welding for a variety of glass materials.

The bonding of dissimilar glass should be treated in a more delicate manner because the thermal expansion coefficients of each glass substrate are different. Such bonding is expected to result in more opportunities for wider applications in electronic, electromechanical, and medical devices. Bonding of fused silica and borosilicate glass was successfully demonstrated using an 85 fs, 800 nm laser at a repetition rate of 1 kHz.[41] The thermal expansion coefficients of fused silica and borosilicate glass are $35.9 \times 10^{-7}/°C$ and $7 \times 10^{-7}/°C$, respectively. Figure 39 shows the thresholds of incident laser energy to weld these dissimilar substrates as a function of the laser scanning speed. Welding was accomplished in region 1, whereas no welding occurred in region 2. The laser energy required for welding was almost proportional to the scanning speed. In region 1, bonding strengths of 14.9–15.3 MPa were achieved (higher bonding strength was achieved at higher incident energy and lower translation velocity).

The ultrafast laser welding technique has been further extended to bond glass to other materials such as Si[185] and metals.[197] Welding non-alkali glass to Si was attempted using a femtosecond laser operated at 800 nm with a 130 fs pulse width and a repetition rate of 1 kHz.[197] At the
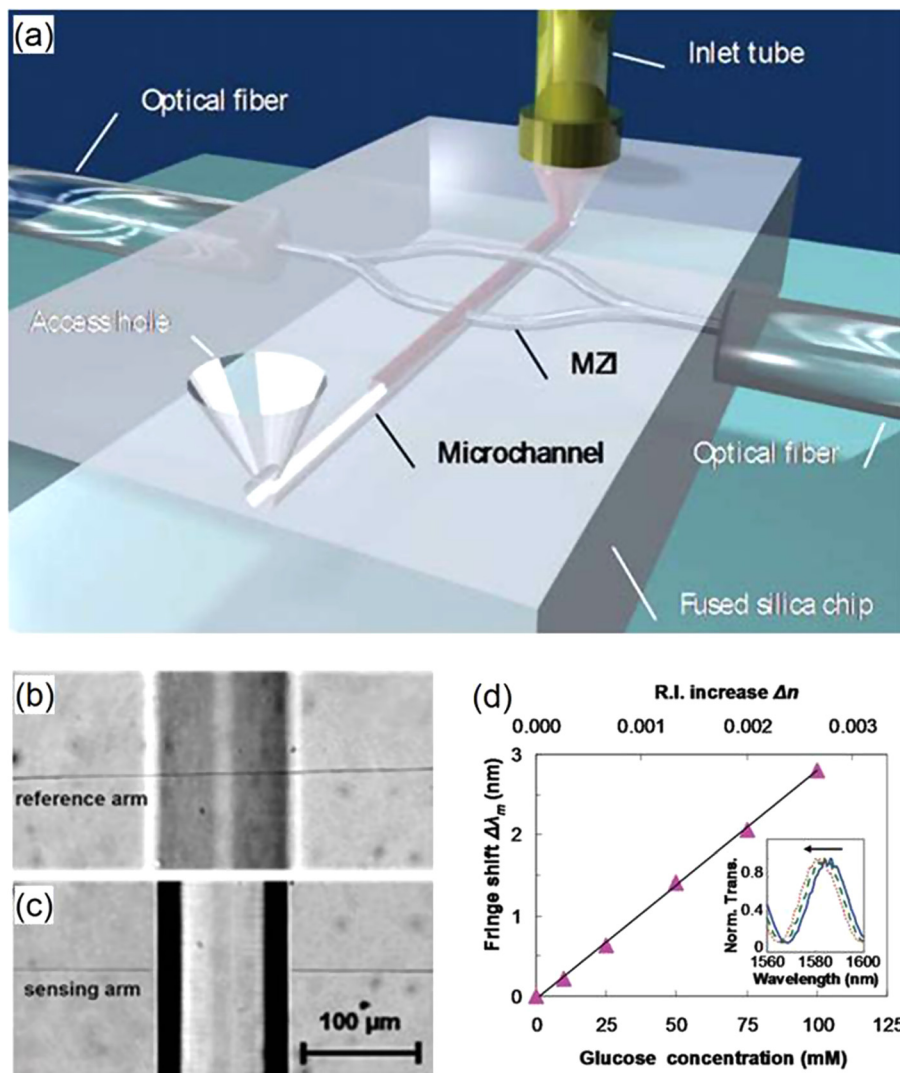
FIG. 36. (a) Schematic of microfluidic channel and integrated MZI fabricated with a femtosecond laser. The sensing arm crosses the channel orthogonally, while the reference arm passes over it. (b) and (c) Micrographs showing the two arms of the MZI crossing the microfluidic channel. Because of the tilted geometry, the reference arm (b) passes over the channel while the sensing arm (c) intersects the channel. (d) Measured fringe shift for different concentrations of D-glucose in water (inset: 0 mM solid line; 50 mM dashed line; 100 mM dotted line); the corresponding increase in the refractive index is also shown. Reproduced with permission from Crespi *et al.*, Lab Chip **10**, 1167 (2010). Copyright 2010 The Royal Society of Chemistry.

wavelength used, Si is not transparent; therefore, it is reasonable to consider that absorption of the laser beam by Si is responsible for the melting at the interface that gives rise to welding. Compared with welding using a nanosecond laser (527 nm, 600 ns, 1 kHz), the femtosecond laser enables a reduction in the pulse energy for welding by two orders of magnitude and also suppresses heat damage. These results suggest that the melting of glass due to multiphoton absorption may cause a positive effect in welding.

C. Enhancement of bonding performance

The bonding strength of welded glass is one of the most important characteristics that requires enhancement. Several
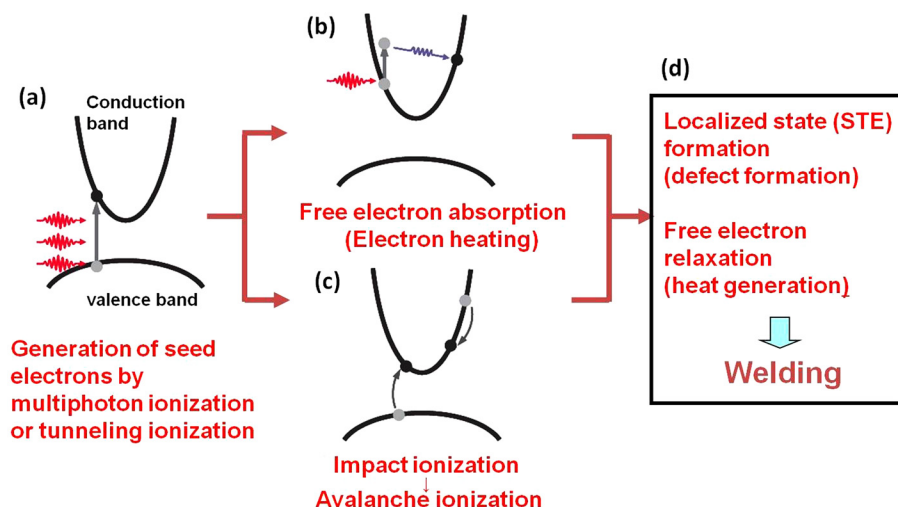
FIG. 37. Electron excitation and relaxation processes in glass induced by ultrafast laser irradiation. (a) Free electron generation by either multiphoton ionization or tunneling ionization, (b) electron heating, (c) impact ionization followed by Avalanche ionization, (d) and localized state formation and free electron relaxation. Reproduced with permission from K. Sugioka and Y. Cheng, *Femtosecond Laser 3D Micromachining for Microfluidic and Optofluidic Applications*, Springer Briefs in Applied Science and Technology (Springer, London, 2014), p. 25. Copyright 2014 Springer.[210]

FIG. 38. Schematic diagram of ultrafast laser microwelding of two substrates. (a) Two stacked substrates. (b) Fixing of two substrates using a sample holder and a pressing lens. (c) Welding of two substrates with focused femtosecond laser pulses at the interface between the two substrates. Reproduced with permission from Tamaki *et al*. Opt. Express **14**, 10 460 (2006). Copyright 2006 The Optical Society of America.
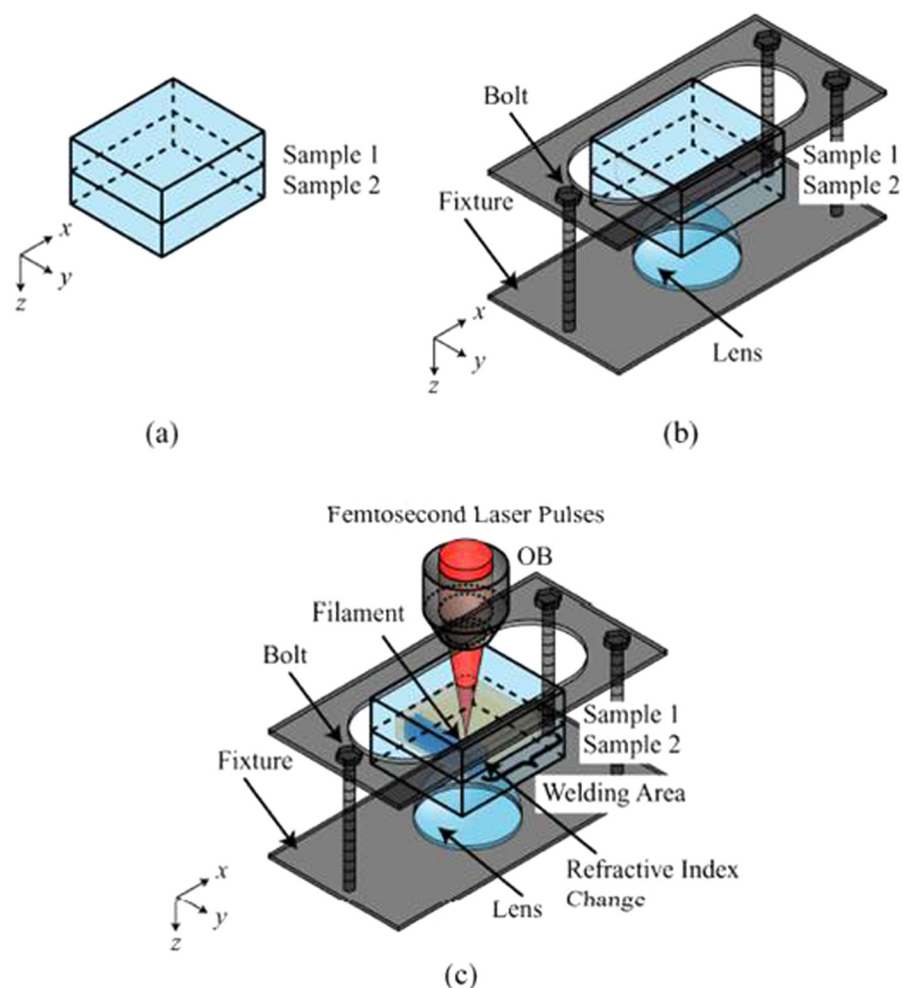
efforts have been made to enhance the bonding strength. In the beginning of glass bonding researches using ultrafast lasers, two glass substrates were stacked and then mechanically pressed together to eliminate the air gap, as shown in Fig. 38(a). However, such close contact with pressure leaves a substantial amount of bending stress inside the samples, which sometimes leads to crack formation and/or weakened joint strength. To overcome this problem, the glass substrates were pre-bonded by optical contact bonding.[184] Optical bonding can be achieved due to van der Waals forces by pushing two glass substrates together, of which the surfaces must be very clean, smooth, and flat. Typical conditions required for optical contact bonding of samples are a surface roughness of less than 0.5 nm, a total thickness variation of 5 μm, and a flatness of less than 30 μm.[198] Optical contact samples provide defect-free welding seams for successive ultrafast laser welding. As a result, the bonding strength of borosilicate glass was evaluated to be between 50 and 90 MPa, which was substantially higher than that of mechanically pressed samples.[176]

As described in Sec. V A, glass melting associated with heating based on multiphoton absorption with an ultrafast laser is responsible for glass welding. Heat diffusion out of the laser focal volume can be suppressed due to the ultrashort pulse width of the ultrafast laser (see Sec. II A). Therefore, the molten pool created by ultrafast laser welding should, in principle, almost correspond to the focal volume. However, when the time interval between consecutive pulses is shorter than the time scale for cooling to room temperature, the generated heat is accumulated, leading to very high temperatures, so producing a significantly larger molten pool. Figure 40 shows optical micrographs of borosilicate glass irradiated with 375 fs, 1045 nm laser pulses for various repetition rates and number of pulses.[49] Cumulative heating is evident at repetition rates of 200 kHz and higher. The size of the molten pool increases with both the repetition rate and the number of pulses. The critical repetition rate that induces cumulative heating (typically in the order of hundreds of kilohertz) is dependent on the physical properties of the material, such as thermal diffusivity. Thus, an ultrafast laser with a repetition rate higher than several hundred kilohertz can improve welding performance, such as the process efficiency and bonding strength, due to the heat accumulation effect.[13,176,182,186]

A picosecond laser is superior to a femtosecond laser in terms of higher joining efficiency by its higher nonlinear absorptivity.[182] The nonlinear absorptivity of an ultrafast laser is specifically associated with the combination of multiphoton ionization and subsequent avalanche ionization. The higher nonlinear absorptivity with the picosecond laser is attributed to the sufficiently long pulse duration for more efficient growth of the free electron density in the conduction band due to avalanche ionization induced by the latter part

TABLE I. Typical works on ultrafast laser welding for a variety of glass materials.

Bonded materials	Laser			Remarks	References
	Pulse width	Wavelength	Repetition rate		
Fused silica	130 fs	800 nm	1 kHz	First demonstration of glass welding by ultrafast laser	175
	550 fs	515 nm	9.4 MHz	Welding by femtosecond laser bursts	178
	750 fsz	1030 nm	up to 1MHz	Complete four edge sealing by multiline scanning	180
	550 fs	515 nm	9.4 MHz	Breaking stress up to 75% of bulk fused silica	14
Fused silica bolisilicate glass	85 fs	800 nm	1 kHz	Characterization of joint strength	177
Borosilicate glass	10 ps		up to 500 kHz	Superiority of ps laser in glass welding as compared with fs laser	182
	16 ps		1 kHz		
	406 fs	1045 nm	1 MHz 100	Dependence of repetition rate, thermal conduction model	13
	325 fs	1045 nm	kHz		
	10 ps	1064 nm	50 kHz – 1 MHz	Simulation by thermal conduction model	183
	10 ps	1064 nm	1 MHz	Defect-free welding by prebonding the samples by optical contact	184
	350 fs	1045 nm	0.7 MHz	Dependence of dimension and geometry of welding seam on scan speed, repetition rate and pulse energy	185
	350 fs	1045 nm	up to 1 MHz	Geometry of welding seam	186
Soda-lime glass	10 ps	1064 nm	up to 8.2 MHz	Measurements of shear strength and bonding energy for different experimenta conditions	187
Non-alkali alumino silicate glass	360 fs	1558 nm	500 kHz	Localized heat accumulation effect	176
Photosensitive (Foturan) glass	360 fs	1045 nm	200 kHz	Double-pulse irradiation	40
	360 fs	1045 nm	200 kHz	Double-pulse irradiation, characterization, mechanism	188
	360 fs	1045 nm	200 kHz	Double-pulse irradiation, mechanism	189
	10 ps	1064 nm	50 kHz to 8.2 MHz	Relation of mechanical strength on the averaged absorbed laser power	190
Glass slide	10 ps	1064 nm	1 MHz	Dependence of hear force and shear strength on focal displacement from the joining surface	195
Fused silica fused silica/borosilicate glass	70 fs	787 nm	10–300 kHz	Filamentation based ultrafast laser welding	179
	70 fs	790 nm	250 kHz	Bonding of dissimilar materials	181
Fused silica/bolosilicate glass	85 fs	800 nm	1 kHz	Welding of dissimilar materials	41
	10 ps	1064 nm	0.5–2 MHz	Mechanical properties of welded seams	191
Fused silica/bolosilicate glass/ULE/zerodur	550 fs	515 nm	9.4 MHz	Welding various combination of dissimilar glass materials	192
Optical fiber/glass slide	70 fs	787 nm	250 kHz	Assembling endcaps of optical fibers	193
Spherical glass bead/float glass	10 ps		100 kHz/500 kHz	Sphere-to-plate welding	194
Sodium borate sodium borate/borosilicate	180 fs	785 nm	1 kHz	Bonding of Sm^{3+} and Cr^{3+} doped glasses	196

of the laser pulse. It was suggested that a pulse duration of 1–10 ps is suitable for local melting because the laser energy can be deposited to the electron system before it is transferred to the lattice, while higher nonlinear absorptivity is achieved than that with a femtosecond laser.[182]

Other approaches include the use of non-linear propagation effects, such as self-focusing and filamentation.[175,179] The peak power of an ultrafast laser can easily reach the critical power required to induce self-focusing by the Kerr effect.[199,200] Loosely focused ultrafast laser pulses generate a filament up to several hundred micrometers in length due to the dynamic balance between self-focusing and self-diffraction by the plasma generated in the filament.[201,202] Ionization and plasma relaxation inside the filament that crosses the interface between two glass substrates transfer the absorbed laser energy to the material. The pressure generated inside the focal volume induces microscopic deformation, which is essential for mixing of the molten material inside the filament zone. The filamentation of ultrafast laser pulses produces a larger welding volume and thus reduces the laser intensity. Furthermore, it enables the welding of thicker samples because the working distance of the focusing lens typically used to produce filamentation is longer than 10 mm.

Femtosecond laser welding of glass proceeds from heat generation via successive plural electron excitation and relaxation processes, specifically multiphoton ionization or tunneling ionization followed by electron heating or avalanche ionization (see Sec. V A). Selective control of each electron excitation process is a challenging approach for enhancing the welding quality and efficiency. A tailored ultrafast laser pulse provides the possibility to control the transient free electron density in glass.[203] Double-pulse irradiation with an ultrafast laser beam has been proposed for application to high-efficiency glass welding, which permits control of the individual electron excitation processes, i.e., multiphoton ionization or tunneling ionization by the
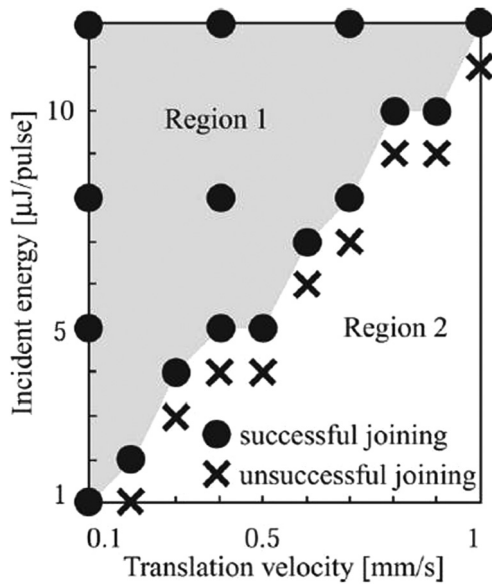
FIG. 39. Dependence of laser-pulse energy and translation velocity on the probability of joining two substrates, fused silica and borosilicate glass. Reproduced with permission from Appl. Phys. Lett. **89**, 021 106 (2006). Copyright 2006 AIP Publishing LLC.

first pulse and electron heating or avalanche ionization by the second pulse, to generate free electrons more efficiently.[40,188,189] Figure 41 shows the dependence of the bonding strength on the delay time between the first and second pulses in double-pulse irradiation for photosensitive Foturan glass welding. The bonding strength increased rapidly from 10.52 to 13.36 MPa (27% increase) when the delay time was increased from 0 to 15 ps. However, the bonding strength decreased abruptly when the delay time was increased from 15 ps to ca. 30 ps. A small rise in bonding strength was observed for a delay time around 100 ps and then decreased gradually with longer delay times. The bonding strengths of 11–11.5 MPa obtained for delay times between 30 ps and 40 ns are still slightly higher than those obtained for a delay time of 0 ps and for single-pulse irradiation.
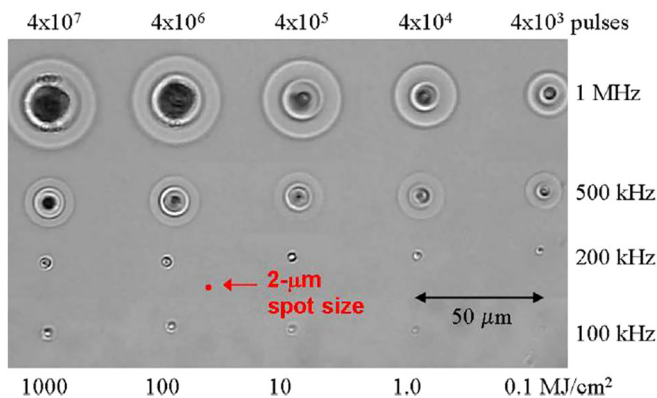

FIG. 40. Optical micrographs of HAZ formed in borosilicate glass irradiated with a 375 fs, 1045 nm laser. Total pulse (top) and fluence accumulation (bottom) are shown for each column and the laser repetition rate is indicated for each row. The laser direction is normal to the glass substrate. Reproduced with permission from Eaton et al., Opt. Express **13**, 4708 (2005). Copyright 2005 The Optical Society of America.
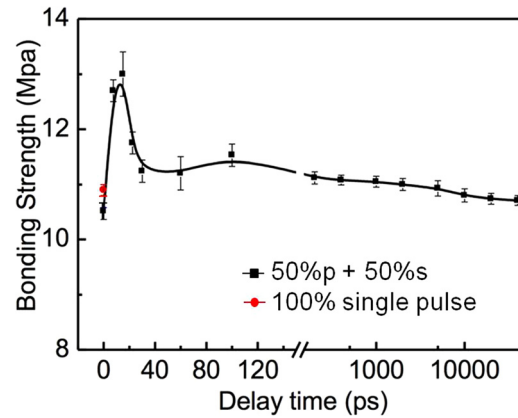

FIG. 41. Dependence of bonding strength on delay time between the first and second pulses of double-pulse irradiation for photosensitive Foturan glass welding. Reproduced with permission from Wu et al., Opt. Express **20**, 28 893 (2012). Copyright 2012 The Optical Society of America.

A mechanism for microwelding with femtosecond double-pulse irradiation has been proposed based on electron excitation and relaxation processes in glass and is summarized in Fig. 42. The first pulse excites free electrons (i.e., seed electrons) from the valance band to the conduction band by multiphoton absorption or tunneling ionization within a few hundred femtoseconds [Fig. 42(a) depicts multiphoton ionization]. These free electrons couple with the lattice over a time scale ranging from less than a picosecond to several tens of picoseconds, depending on the material.[204,205] If the second pulse arrives during this time period, its energy can be absorbed by the excited electrons, which results in electron heating [Fig. 42(b)] or avalanche ionization [Fig. 42(c)]. These processes are induced successively by the two laser pulses (i.e., multiphoton absorption or tunneling ionization induced by the first pulse followed by electron heating or avalanche ionization induced by the second pulse) and can generate higher-energy free electrons or more free electrons for efficient heating, which imparts a higher bonding strength for welding. However, if the second laser pulse arrives a couple of tens of picoseconds after the first pulse, then the second pulse does not interact with the free electrons because they have already relaxed, so that the bonding strength is significantly reduced. Some excited electrons relax to the valence band, thereby generating heat, while other electrons may be trapped in a localized state that has a longer relaxation time due to defects or excitons. The second pulse can still be absorbed by such a localized state to create an excited state, even for delay times longer than a couple of tens of picoseconds [Fig. 42(d)]. This localized-state absorption has been induced by single photons of a femtosecond laser beam (1045 nm).[189] Therefore, this absorption should be more efficiently induced than the interband excitation shown in Fig. 42(a) because the order of multiphoton absorption is much lower than that for interband excitation. Excitation from the localized state to the conduction band is another possible channel for this absorption, rather than the formation of an excited state. Electrons excited from the localized state eventually relax to the ground state or the valence band, thereby generating heat. This absorption of the
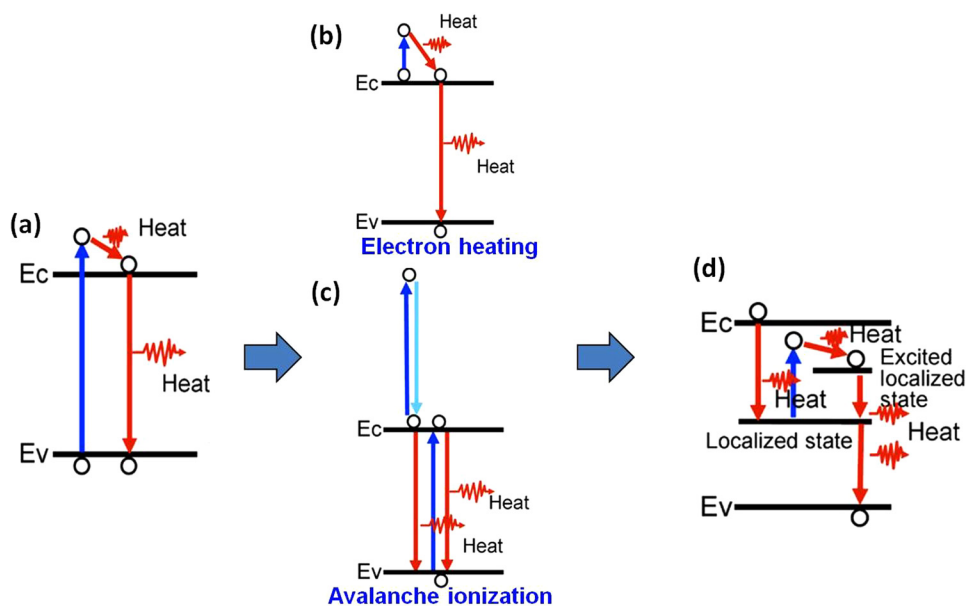
FIG. 42. Possible physical mechanism for glass welding by double-pulse irradiation, which involves electron excitation and relaxation processes including multiphoton ionization or tunneling ionization, avalanche ionization or electron heating, and electron trapping at the localized state. Reproduced with permission from Wu *et al.*, Opt. Express **20**, 28 893 (2012). Copyright 2012 The Optical Society of America.

second pulse by the localized state explains why double-pulse irradiation with delay times between 30 ps and 40 ns results in a higher bonding strength than single-pulse irradiation. After several tens of nanoseconds, electrons trapped in the localized state will relax and absorption by the localized state will no longer occur. Consequently, the bonding strength gradually decreases for delay times greater than several tens of nanoseconds.

VI. CONCLUSIONS AND FUTURE PROSPECTS

The efficient confinement of nonlinear interactions within sub-diffraction focal volumes has led to the realization of femtosecond laser 3D micro and nanofabrication with sub-100 nm resolution stereolithography based on TPP, in addition to writing of optical waveguides and the fabrication of microfluidic channels in bulk transparent materials by internal processing. Another interesting scheme for nonlinear interaction is melting at the interface of two tightly stacked glass substrates, which results in the bonding of various glasses. The flexibility of the direct writing scheme that employs scanning of tightly focused femtosecond laser pulses has enabled the formation of various 3D micro/nanostructures with almost unlimited geometries and configurations, which has had a significant impact on a broad range of applications ranging from optoelectronics, photonics and MEMS to chemical, biological and medical systems. In the past two decades, efforts have been mostly devoted to laboratory investigations with particular concentration on the clarification of mechanisms, the development of new fabrication technologies, and extension of the application range. However, recent advances in the development of high average power, high repetition rate, stable femtosecond laser sources have significantly increased the throughput and reliability of femtosecond laser 3D micro and nanofabrication, which has provided impetus for the acceleration of industrial and practical applications of laboratory-developed technologies.[206,207]

The techniques introduced in this review, such as the fabrication of 3D polymer micro- and nanocomponents by TPP, optical waveguide writing, the fabrication of microfluidic channels, and glass-glass bonding, have long been under intensive investigation, and now becomes more and more open for not only scientific research in various fields but also product development. TPP can be used to produce a wide variety of micro- and nanodevices for photonics, micro- and nanomechanics, biological studies, and medical treatment. Optical waveguides and microfluidic channels are the basic building blocks of photonic circuits and microfluidic systems, respectively. Glass-glass bonding plays a key role in the packaging of a variety of microdevices, including optoelectronic devices, medical systems, MEMS, and small satellites. To perfect these technologies, efforts should be focused on investigation of the underlying mechanisms to achieve better control of the structural changes and/or morphologies in the laser affected zone, refinement of the beam shaping technologies for precise tuning of the geometries of laser written structures and to promote the fabrication efficiency, and to improve the fabrication resolution for precise alignment and coupling between multiple components (e.g., waveguide-waveguide coupling and the intersection of waveguide cores and microfluidic channels). The above-mentioned additive and subtractive processes have been independently developed, each of which inevitably has its own limitations. To breakthrough this point, a new strategy has been recently proposed, in which synergetic combination of each process into a hybrid approach will open up a new door to enhance the flexibility and/or capability of 3D femtosecond micro and nanofabrication by taking the advantages of complementary characteristics of each individual approach.[166,208] Future advances of this technology will lead to the development of smart manufacturing platforms for innovative applications in a variety of fields including integrated photonic devices, functional microfluidics, optofluidics, medical devices, MEMS, and MEMS packaging.[209]

[1] R. R. Gattass and E. Mazur, Nat. Photonics **2**, 219 (2008).
[2] K. Sugioka and Y. Cheng, Light: Sci. Appl. **3**, e149 (2014).
[3] N. Bloembergen, J. Nonlinear Opt. Phys. Mater. **6**, 377 (1997).

[4]B. N. Chichkov, C. Momma, S. Nolte, F. von Alvensleben *et al*., Appl. Phys. A **63**, 109 (1996).

[5]K. Sugioka, B. Gu, and A. Holmes, in *Laser Direct-write Processing*, edited by Craig B. Arnold and Alberto Pigué (Mater. Res. Soc. Bulletin, 2007), Vol. 32, p. 47.

[6]Y. Nakata, T. Okada, and M. Maeda, Jpn. J. Appl. Phys. **42**, L1452 (2003).

[7]C. A. Aguilar, Y. Lu, S. Mao, and S. Chen, Biomaterials **26**, 7642 (2005).

[8]S. Maruo and J. T. Fourkas, Laser Photonics Rev. **2**, 100 (2008).

[9]B. B. Xu, Y. L. Zhang, H. Xia, W. F. Dong *et al*., Lab Chip **13**, 1677 (2013).

[10]K. Sugioka and Y. Cheng, Lab Chip **12**, 3576 (2012).

[11]R. Osellame, H. J. W. M. Hoekstra, G. Cerullo, and M. Pollnau, Laser Photonics Rev. **5**, 442 (2011).

[12]K. Sugioka, Y. Hanada, and K. Midorikawa, Laser Photonics Rev. **4**, 386 (2010).

[13]I. Miyamoto, A. Horn, J. Gottmann, D. Wortmann *et al*., J. Laser Micro/Nanoeng. **2**, 57 (2007).

[14]S. Richter, S. Döring, A. Tünnermann, and S. Nolte, Appl. Phys. A **103**, 257 (2011).

[15]F. Chen and J. R. V. de Aldana, Laser Photonics Rev. **8**, 251 (2014).

[16]K. Itoh, W. Watanabe, S. Nolte, and C. B. Schaffer, in *Ultrafast Lasers in Materials Research*, edited by David G. Cahill and Steve M. Yalisove (Mater. Res. Soc. Bulletin, 2006), Vol. 31, p. 620.

[17]M. Heinrich, K. Rademaker, and S. Nolte, in *Femtosecond Laser Micromachining*, edted by R. Osellame, G. Cerullo, and R. Ramponi (Springer, Berlin, Heidelberg, 2012), Vol. 123, p. 295.

[18]K. M. Davis, K. Miura, N. Sugimoto, and K. Hirao, Opt. Lett. **21**, 1729 (1996).

[19]E. N. Glezer, M. Milosavljevic, L. Huang, R. J. Finlay *et al*., Opt. Lett. **21**, 2023 (1996).

[20]S. Maruo, O. Nakamura, and S. Kawata, Opt. Lett. **22**, 132 (1997).

[21]S. Maruo, K. Ikuta, and H. Korogi, Appl. Phys. Lett. **82**, 133 (2003).

[22]D. Wu, L. Niu, Q. Chen, R. Wang *et al*., Opt. Lett. **33**, 2913 (2008).

[23]K. K. Seet, V. Mizeikis, S. Matsuo, S. Juodkazis *et al*., Adv. Mater. **17**, 541 (2005).

[24]M. Deubel, G. von Freymann, M. Wegener, S. Pereira *et al*., Nat. Mater. **3**, 444 (2004).

[25]M. S. Rill, C. Plet, M. Thiel, I. Staude *et al*., Nat. Mater. **7**, 543 (2008).

[26]J. K. Gansel, M. Thiel, M. S. Rill, M. Decker *et al*., Science **325**, 1513 (2009).

[27]T. Ikegami, R. Ozawa, M. P. Stocker, K. Monaco *et al*., J. Laser Micro/Nanoeng. **8**, 6 (2013).

[28]L. Amato, Y. Gu, N. Bellini, S. M. Eaton *et al*., Lab Chip **12**, 1135 (2012).

[29]R. R. Thomson, A. K. Kar, and J. Allington-Smith, Opt. Express **17**, 1963 (2009).

[30]G. D. Marshall, A. Politi, J. C. F. Matthews, P. Dekker *et al*., Opt. Express **17**, 12546 (2009).

[31]A. Crespi, R. Osellame, R. Ramponi, D. J. Brod *et al*., Nat. Photonics **7**, 545 (2013).

[32]Y. Hanada, K. Sugioka, I. Shihira-Ishikawa, H. Kawano *et al*., Lab Chip **11**, 2109 (2011).

[33]A. Crespi, Y. Gu, B. Ngamsom, H. J. Hoekstra *et al*., Lab Chip **10**, 1167 (2010).

[34]Y. Liao, J. Xu, Y. Cheng, Z. Zhou *et al*., Opt. Lett. **33**, 2281 (2008).

[35]M. Kim, D. J. Hwang, H. Jeon, K. Hiromatsu *et al*., Lab Chip **9**, 311 (2009).

[36]F. Bragheri, L. Ferrara, N. Bellini, K. C. Vishnubhatla *et al*., J. Biophotonics **3**, 234 (2010).

[37]D. Choudhury, W. T. Ramsay, R. Kiss, N. A. Willoughby *et al*., Lab Chip **12**, 948 (2012).

[38]A. Schaap, T. Rohrlack, and Y. Bellouard, J. Biophotonics **5**, 661 (2012).

[39]J. Song, J. Lin, J. Tang, Y. Liao *et al*., Opt. Express **22**, 14792 (2014).

[40]K. Sugioka, M. Iida, H. Takai, and K. Micorikawa, Opt. Lett. **36**, 2734 (2011).

[41]W. Watanabe, S. Onda, T. Tamaki, K. Itoh *et al*., Appl. Phys. Lett. **89**, 021106 (2006).

[42]W. S. Fan, R. Storz, H. W. K. Tom, and J. Bokor, Phys. Rev. B **46**, 13592 (1992).

[43]C. K. Sun, F. Vallée, L. H. Acioli, E. P. Ippen *et al*., Phys. Rev. B **50**, 15337 (1994).

[44]S. S. Wellershoff, J. Hohlfeld, J. Güdde, and E. Matthias, Appl. Phys. A **69**, S99 (1999).

[45]J. Hohlfeld, S. S. Wellershoff, J. Güdde, U. Conrad *et al*., Chem. Phys. **251**, 237 (2000).

[46]S. I. Anisimov and B. Rethfeld, Proc. SPIE **3093**, 192 (1997).

[47]P. B. Corkum, F. Brunel, N. K. Sherman, and T. Srinivasan-Rao, Phys. Rev. Lett. **61**, 2886 (1988).

[48]M. Fujita and M. Hashida, Oyo Buturi **73**, 178 (2004) (in Japanese).

[49]S. M. Eaton, H. Zhang, P. R. Herman, F. Yoshino *et al*., Opt. Express **13**, 4708 (2005).

[50]S. M. Eaton, H. Zhang, M. L. Ng, J. Li *et al*., Opt. Express **16**, 9443 (2008).

[51]B. C. Stuart, M. D. Feit, A. M. Rubenchik, B. W. Shore *et al*., Phys. Rev. Lett. **74**, 2248 (1995).

[52]L. V. Keldysh, Sov. Phys. JETP **20**, 1307 (1965).

[53]S. Küper and M. Stuke, Microelectron. Eng. **9**, 475 (1989).

[54]S. Kawata, H. B. Sun, T. Tanaka, and K. Takada, Nature **412**, 697 (2001).

[55]D. Tan, Y. Li, F. Qi, H. Yang *et al*., Appl. Phys. Lett. **90**, 071106 (2007).

[56]S. M. Kuebler, M. Rumi, T. Watanabe, K. Braun *et al*., J. Photopolym. Sci. Technol. **14**, 657 (2001).

[57]H. Kodama, Rev. Sci. Instrum. **52**, 1770 (1981).

[58]See http://www.cmet.co.jp/eng/app.php for information about applications of products produced by laser stereolithography.

[59]B. Cumpston, S. Ananthavel, S. Barlow, D. Dyer *et al*., Nature **398**, 51 (1999).

[60]S. M. Kuebler, K. Braun, W. Zhou, J. Cammack *et al*., J. Photochem. Photobiol., A **158**, 163 (2003).

[61]W. H. Zhou, S. M. Kuebler, K. Braun, T. Y. Yu *et al*., Science **296**, 1106 (2002).

[62]H. B. Sun, M. Maeda, K. Takada, J. W. M. Chon *et al*., Appl. Phys. Lett. **83**, 819 (2003).

[63]H. B. Sun, K. Takada, M. S. Kim, K. S. Lee *et al*., Appl. Phys. Lett. **83**, 1104 (2003).

[64]S. W. Hell and J. Wichmann, Opt. Lett. **19**, 780 (1994).

[65]L. Li, R. R. Gattass, E. Gershgoren, H. Hwang *et al*., Science **324**, 910 (2009).

[66]Z. Gan, Y. Cao, R. A. Evans, and M. Gu, Nat. Commun. **4**, 2061 (2013).

[67]Z. B. Sun, X. Z. Dong, W. Q. Chen, S. Nakanishi *et al*., Adv. Mater. **20**, 914 (2008).

[68]J. Wang, H. Xia, B. B. Xu, L. G. Niu *et al*., Opt. Lett. **34**, 581 (2009).

[69]H. Xia, J. A. Wang, Y. Tian, Q. D. Chen *et al*., Adv. Mater. **22**, 3204 (2010).

[70]Y. L. Sun, W. F. Dong, R. Z. Yang, X. Meng *et al*., Angew. Chem. Int. Ed. **51**, 1558 (2012).

[71]R. Guo, S. Z. Xiao, X. M. Zhai, J. W. Li *et al*., Opt. Express **14**, 810 (2006).

[72]Q. Chen, D. Wu, L. G. Niu, J. Wang *et al*., Appl. Phys. Lett. **91**, 171105 (2007).

[73]Y. Li, Y. S. Yu, L. Guo, S. Z. Wu *et al*., J. Opt. **12**, 035203 (2010).

[74]L. G. Niu, D. Wang, T. Jiang, S. Z. Wu *et al*., Opt. Commun. **284**, 777 (2011).

[75]Q. D. Chen, X. F. Lin, L. G. Niu, D. Wu *et al*., Opt. Lett. **33**, 2559 (2008).

[76]S. John, Phys. Rev. Lett. **58**, 2486 (1987).

[77]C. C. Cheng and A. Scherer, J. Vac. Sci. Technol. B **13**, 2696 (1995).

[78]H. Sun, S. Matsuo, and H. Misawa, Appl. Phys. Lett. **74**, 786 (1999).

[79]H. B. Sun, V. Mizeikis, Y. Xu, S. Juodkazis *et al*., Appl. Phys. Lett. **79**, 1 (2001).

[80]S. Maruo and K. Ikuta, Appl. Phys. Lett. **76**, 2656 (2000).

[81]S. Maruo and H. Inoue, Appl. Phys. Lett. **89**, 144101 (2006).

[82]S. Maruo, A. Takaura, and Y. Saito, Opt. Express **17**, 18525 (2009).

[83]J. C. McDonald and G. M. Whitesides, Acc. Chem. Res. **35**, 491 (2002).

[84]J. Wang, Y. He, H. Xia, L. G. Niu *et al*., Lab Chip **10**, 1993 (2010).

[85]T. W. Lim, Y. Son, Y. J. Jeong, D. Y. Yang *et al*., Lab Chip **11**, 100 (2011).

[86]Y. He, B. L. Huang, D. X. Lu, J. Zhao *et al*., Lab Chip **12**, 3866 (2012).

[87]M. H. Olsen, G. M. Hjorto, M. Hansen, O. Met *et al*., Lab Chip **13**, 4800 (2013).

[88]M. Farsari and B. Chichkov, Nat. Photonics **3**, 450 (2009).

[89]A. Ovsianikov, M. Malinauskas, S. Schlie, B. Chichkov *et al*., Acta Biomater. **7**, 967 (2011).

[90]P. Tayalia, C. R. Mendonca, T. Baldacchini, D. J. Mooney *et al*., Adv. Mater. **20**, 4494 (2008).

[91]P. W. Wu, W. Cheng, I. B. Martini, B. Dunn *et al*., Adv. Mater. **12**, 1438 (2000).

[92]F. Stellacci, C. A. Bauer, T. Meyer-Friedrichsen, W. Wenseleers *et al.*, Adv. Mater. **14**, 194 (2002).

[93]Y. Y. Cao, N. Takeyasu, T. Tanaka, X. M. Duan *et al.*, Small **5**, 1144 (2009).

[94]A. Ishikawa, T. Tanaka, and S. Kawata, Appl. Phys. Lett. **89**, 113102 (2006).

[95]S. Maruo and T. Saeki, Opt. Express **16**, 1174 (2008).

[96]Y. Shimotsuma, P. G. Kazansky, J. Qiu, and K. Hirao, Phys. Rev. Lett. **91**, 247405 (2003).

[97]V. R. Bhardwaj, E. Simova, P. P. Rajeev, C. Hnatovsky *et al.*, Phys. Rev. Lett. **96**, 057404 (2006).

[98]S. Kanehira, J. Si, J. Qiu, K. Fujita *et al.*, Nano Lett. **5**, 1591 (2005).

[99]Y. Liu, M. Shimizu, B. Zhu, Y. Dai *et al.*, Opt. Lett. **34**, 136 (2009).

[100]S. K. Sundaram and E. Mazur, Nat. Mater. **1**, 217 (2002).

[101]P. G. Kazansky, Y. Weijia, E. Bricchi, J. Bovatsek *et al.*, Appl. Phys. Lett. **90**, 151120 (2007).

[102]W. Yang, P. G. Kazansky, and Y. P. Svirko, Nat. Photonics **2**, 99 (2008).

[103]Z. Wang, K. Sugioka, and K. Midorikawa, Appl. Phys. A **89**, 951 (2007).

[104]M. Masuda, K. Sugioka, Y. Cheng, N. Aoki *et al.*, Appl. Phys. A **76**, 857 (2003).

[105]S. Sowa, W. Watanabe, T. Tamaki, J. Nishii *et al.*, Opt. Express **14**, 291 (2006).

[106]Y. Hanada, K. Sugioka, and K. Midorikawa, Opt. Express **18**, 446 (2010).

[107]K. Sugioka and Y. Cheng, Adv. Opt. Technol. **1**, 353 (2012).

[108]A. Manz, N. Graber, and H. M. Widmer, Sens. Actuators, B **1**, 244 (1990).

[109]G. M. Whitesides, Nature **442**, 368 (2006).

[110]Y. Kondo, J. Qiu, T. Mitsuyu, K. Hirao *et al.*, Jpn. J. Appl. Phys. **38**, L1146 (1999).

[111]A. Marcinkevičius, S. Juodkazis, M. Watanabe, M. Miwa *et al.*, Opt. Lett. **26**, 277 (2001).

[112]Y. Cheng, K. Sugioka, M. Masuda, K. Toyoda *et al.*, RIKEN Rev. **50**, 101 (2003).

[113]K. Sugioka, Y. Cheng, and K. Midorikawa, Appl. Phys. A **81**, 1 (2005).

[114]S. Kiyama, S. Matsuo, S. Hashimoto, and Y. Morihira, J. Phys. Chem. C **113**, 11560 (2009).

[115]D. Choudhury, A. Rodenas, L. Paterson, F. Díaz *et al.*, Appl. Phys. Lett. **103**, 041101 (2013).

[116]C. Hnatovsky, R. S. Taylor, E. Simova, V. R. Bhardwaj *et al.*, Opt. Lett. **30**, 1867 (2005).

[117]Y. Li, K. Itoh, W. Watanabe, K. Yamada *et al.*, Opt. Lett. **26**, 1912 (2001).

[118]K. Ke, E. F. Hasselbrink, and A. J. Hunt, Anal. Chem. **77**, 5083 (2005).

[119]Y. Li and S. Qu, Curr. Appl. Phys. **13**, 1292 (2013).

[120]Y. Liao, Y. Ju, L. Zhang, F. He *et al.*, Opt. Lett. **35**, 3225 (2010).

[121]Y. Ju, Y. Liao, L. Zhang, Y. Sheng *et al.*, Microfluid. Nanofluid. **11**, 111 (2011).

[122]Y. Liao, J. Song, E. Li, Y. Luo *et al.*, Lab Chip **12**, 746 (2012).

[123]Y. Liao, Y. Cheng, C. Liu, J. Song *et al.*, Lab Chip **13**, 1626 (2013).

[124]Y. Nasu, M. Kohtoku, and Y. Hibino, Opt. Lett. **30**, 723 (2005).

[125]G. Cerullo, R. Osellame, S. Taccheo, M. Marangoni *et al.*, Opt. Lett. **27**, 1938 (2002).

[126]Y. Cheng, K. Sugioka, K. Midorikawa, M. Masuda *et al.*, Opt. Lett. **28**, 55 (2003).

[127]M. Ams, G. Marshall, D. Spence, and M. Withford, Opt. Express **13**, 5676 (2005).

[128]K. Sugioka, Y. Cheng, K. Midorikawa, F. Takase *et al.*, Opt. Lett. **31**, 208 (2006).

[129]F. He, H. Xu, Y. Cheng, J. Ni *et al.*, Opt. Lett. **35**, 1106 (2010).

[130]D. N. Vitek, D. E. Adams, A. Johnson, P. S. Tsai *et al.*, Opt. Express **18**, 18086 (2010).

[131]Y. Zhang, G. Cheng, G. Huo, Y. Wang *et al.*, Laser Phys. **19**, 2236 (2009).

[132]P. S. Salter, A. Jesacher, J. B. Spring, B. J. Metcalf *et al.*, Opt. Lett. **37**, 470 (2012).

[133]P. S. Salter and M. J. Booth, Opt. Express **20**, 19978 (2012).

[134]D. N. Vitek, E. Block, Y. Bellouard, D. E. Adams *et al.*, Opt. Express **18**, 24673 (2010).

[135]G. Li, J. Ni, H. Xie, B. Zeng *et al.*, Opt. Lett. **39**, 961 (2014).

[136]D. Kim and P. T. C. So, Opt. Lett. **35**, 1602 (2010).

[137]F. He, B. Zeng, W. Chu, J. Ni *et al.*, Opt. Express **22**, 9734 (2014).

[138]P. Kazansky and M. Beresna, in *Femtosecond Laser Micromachining*, edited by R. Osellame, G. Cerullo, and R. Ramponi (Springer, Berlin, Heidelberg, 2012), Vol. 123, p. 127.

[139]P. S. Salter and M. J. Booth, Appl. Phys. Lett. **101**, 141109 (2012).

[140]R. Kammel, R. Ackermann, J. Thomas, J. Götte *et al.*, Light: Sci. Appl. **3**, e169 (2014).

[141]S. Nolte, M. Will, J. Burghoff, and A. Tunnermann, Appl. Phys. A **77**, 109 (2003).

[142]W. Watanabe, T. Asano, K. Yamada, K. Itoh *et al.*, Opt. Lett. **28**, 2491 (2003).

[143]K. Minoshima, A. M. Kowalevicz, I. Hartl, E. P. Ippen *et al.*, Opt. Lett. **26**, 1516 (2001).

[144]W. Chen, S. M. Eaton, H. B. Zhang, and P. R. Herman, Opt. Express **16**, 11470 (2008).

[145]R. Keil, M. Heinrich, F. Dreisow, T. Pertsch *et al.*, Sci. Rep. **1**, 94 (2011).

[146]K. Yamada, W. Watanabe, J. Nishii, and K. Itoh, Jpn. J. Appl. Phys. **42**, 6916 (2003).

[147]F. He, H. Sun, M. Huang, J. Xu *et al.*, Appl. Phys. A **97**, 853 (2009).

[148]E. Bricchi, J. D. Mills, P. G. Kazamsky, B. G. Klappauf *et al.*, Opt. Lett. **27**, 2200 (2002).

[149]G. D. Marshall, P. Dekker, M. Ams, J. A. Piper *et al.*, Opt. Lett. **33**, 956 (2008).

[150]C. Florea and K. A. Winick, J. Lightwave Technol. **21**, 246 (2003).

[151]G. D. Valle, R. Osellame, N. Chiodo, S. Taccheo *et al.*, Opt. Express **13**, 5976 (2005).

[152]M. Ams, P. Dekker, G. D. Marshall, and M. J. Withford, Opt. Lett. **34**, 247 (2009).

[153]O. M. Efimov, L. B. Glebov, K. A. Richardson, E. V. Stryland *et al.*, Opt. Mater. **17**, 379 (2001).

[154]R. R. Thomson, S. Campbell, I. J. Blewett, A. K. Kar *et al.*, Appl. Phys. Lett. **88**, 111109 (2006).

[155]M. Ams, G. D. Marshall, P. Dekker, M. Dubov *et al.*, IEEE J. Sel. Top. Quantum Electron **14**, 1370 (2008).

[156]M. Shiozawa, T. Watanabe, E. Tatsu, M. Umeda *et al.*, Jpn. J. Appl. Phys. **52**, 09LA01 (2013).

[157]T. Watanabe, M. Shiozawa, E. Tatsu, S. Kimura *et al.*, Jpn. J. Appl. Phys. **52**, 09LA02 (2013).

[158]T. Watanabe, T. Shintani, K. Ono, and T. Mine, IEICE Electron. Express **6**, 1569 (2009).

[159]J. Y. Zhang, M. Gecevicius, M. Beresna, and P. G. Kazansky, Phys. Rev. Lett. **112**, 033901 (2014).

[160]L. Sansoni, F. Sciarrino, G. Vallone, P. Mataloni *et al.*, Phys. Rev. Lett. **105**, 200503 (2010).

[161]A. Crespi, R. Osellame, R. Ramponi, V. Giovannetti *et al.*, Nat. Photonnics **7**, 322 (2013).

[162]M. C. Rechtsman, J. M. Zeuner, Y. Plotnik, Y. Lumer *et al.*, Nature **496**, 196 (2013).

[163]D. J. Hwang, T. Y. Choi, and C. P. Grigoropoulos, Appl. Phys. A **79**, 605 (2004).

[164]Y. Hanada, K. Sugioka, H. Kawano, I. Ishikawa *et al.*, Biomed. Microdevices **10**, 403 (2008).

[165]Y. Hanada, K. Sugioka, H. Kawano, I. S. Ishikawa *et al.*, Appl. Surf. Sci. **255**, 9893 (2009).

[166]D. Wu, S. Z. Wu, J. Xu, L. G. Niu *et al.*, Laser Photonics Rev. **3**, 458 (2014).

[167]V. Maselli, J. R. Grenier, S. Ho, and P. R. Herman, Opt. Express **17**, 11719 (2009).

[168]A. Schaap, Y. Bellouard, and T. Rohrlack, Biomed. Opt. Express **2**, 658 (2011).

[169]N. Bellini, K. C. Vishnubhatla, F. Bragheri, L. Ferrara *et al.*, Opt. Express **18**, 4679 (2010).

[170]Z. Wang, K. Sugioka, Y. Hanada, and K. Midorikawa, Appl. Phys. A **88**, 699 (2007).

[171]R. G. Heideman and P. V. Lambeck, Sens. Actuators B **61**, 100 (1999).

[172]F. Quéré, S. Guizard, and Ph. Martin, Europhys. Lett. **56**, 138 (2001).

[173]V. V. Temnov, K. Sokolowski-Tinten, P. Zhou, A. El-Khamhawy *et al.*, Phys. Rev. Lett. **97**, 237403 (2006).

[174]S. S. Mao, F. Quere, S. Guizard, X. Mao *et al.*, Appl. Phys. A **79**, 1695 (2004).

[175]T. Tamaki, W. Watanabe, J. Nishii, and K. Itoh, Jpn. J. Appl. Phys. **44**, L687 (2005).

[176]T. Tamaki, W. Watanabe, and K. Itoh, Opt. Express **14**, 10460 (2006).

[177]W. Watanabe, S. Onda, T. Tamaki, and K. Itoh, Appl. Phys. B **87**, 85 (2007).

[178]F. Zimmermann, S. Richter, S. Doring, A. Tunnermann *et al.*, Appl. Opt. **52**, 1149 (2013).

[179]D. Helie, F. Lacroix, and R. Vallee, J. Laser Micro/Nanoeng. **7**, 284 (2012).

[180]H. Huang, L. M. Yang, and J. Liu, Appl. Opt. **51**, 2979 (2012).

[181]D. Helie, M. Begin, F. Lacroix, and R. Vallee, Appl. Opt. **51**, 2098 (2012).

[182]I. Miyamoto, A. Horn, J. Göttemann, D. Wortmann *et al.*, J. Laser Micro/Nanoeng. **2**, 7 (2007).

[183]I. Miyamoto, K. Cvecek, and M. Schmidt, Opt. Express. **21**, 14291 (2013).

[184]K. Cvecek, I. Miyamoto, J. Strauss, M. Wolf *et al.*, Appl. Opt. **50**, 1941 (2011).

[185]A. Horn, I. Mingareev, A. Werth, M. Kachel *et al.*, Appl. Phys. A **93**, 171 (2008).

[186]A. Horn, I. Mingareev, and A. Werth, J. Laser Micro/Nanoeng. **3**, 114 (2008).

[187]I. Alexeev, K. Cvecek, C. Schmidt, I. Miyamoto *et al.*, J. Laser Micro/Nanoeng. **7**, 279 (2012).

[188]S. Wu, D. Wu, J. Xu, Y. Hanada *et al.*, Opt. Express **20**, 28893 (2012).

[189]S. Wu, D. Wu, J. Xu, H. Y. Wang *et al.*, Opt. Express **21**, 24049 (2013).

[190]I. Miyamoto, K. Cvecek, Y. Okamoto, M. Schmidt *et al.*, Opt. Express **19**, 22961 (2011).

[191]Y. Okamoto, I. Miyamoto, K. Cvecek, A. Okada *et al.*, J. Laser Micro/Nanoeng. **8**, 65 (2013).

[192]S. Richter, F. Zimmermann, S. Doring, A. Tunnermann *et al.*, Appl. Phys. A **110**, 9 (2013).

[193]D. Helie, S. Gouin, and R. Vallee, Opt. Mater. Express **3**, 1742 (2013).

[194]K. Ratautas, G. Raciukaitis, and M. Gedvilas, J. Laser Micro/Nanoeng. **8**, 175 (2013).

[195]K. Cvecek, I. Miyamoto, J. Strauss, V. Bui *et al.*, J. Laser Micro/Nanoeng. **7**, 68 (2012).

[196]Y. Kim, J. Choi, Y. Lee, T. Kim *et al.*, Appl. Phys. A **101**, 147 (2010).

[197]Y. Ozeki, T. Inoue, T. Tamaki, H. Yamaguchi *et al.*, Appl. Phys. Express **1**, 082601 (2008).

[198]Z. Tang, T. Shi, G. Liao, and S. Liu, Microelectron. Eng. **85**, 1754 (2008).

[199]A. Couairon and A. Mysyrowicz, Phys. Rep. **441**, 47 (2007).

[200]S. L. Chin, S. A. Hosseini, W. Liu, Q. Luo *et al.*, Can. J. Phys. **83**, 863 (2005).

[201]S. H. Cho, H. Kumagai, I. Yokota, K. Midorikawa *et al.*, Jpn. J. Appl. Phys. **37**, L737 (1998).

[202]K. Yamada, W. Watanabe, T. Toma, K. Itoh *et al.*, Opt. Lett. **26**, 19 (2001).

[203]L. Englert, B. Rethfeld, L. Haag, M. Wollenhaupt *et al.*, Opt. Express **15**, 17855 (2007).

[204]S. Guizard, P. D'Oliveira, P. Daguzan, P. Martin *et al.*, Nucl. Instrum. Methods Phys. Res. B **116**, 43 (1996).

[205]B. C. Stuart, M. D. Feit, S. Herman, A. M. Rubenchik *et al.*, Phys. Rev. B **53**, 1749 (1996).

[206]J. Gottmann, M. Hermans, and J. Ortmann, J. Laser Micro/Nanoeng. **8**, 15 (2013).

[207]T. Mans, J. Dolkemeyer, and C. Schnitzler, Laser Tech. J. **11**, 40 (2014).

[208]W. Xiong, Y. S. Zhou, X. N. He, Y. Gao *et al.*, Light: Sci. Appl. **1**, e6 (2012).

[209]Y. Bellouard, A. Champion, B. Lenssen, M. Matteucci *et al.*, J. Laser Micro/Nanoeng. **7**, 1 (2012).

[210]K. Sugioka and Y. Cheng, *Femtosecond Laser 3D Micromachining for Microfluidic and Optofluidic Applications*, Springer Briefs in Applied Science and Technology (Springer, London, 2014).

[211]K. Sugioka and Y. Cheng, "Overview of ultrafast laser processing," in *Ultrafast Laser Processing*, edited by K. Sugioka and Y. Cheng (Pan Stanford, Singapore, 2013).